



저작자표시-비영리-변경금지 2.0 대한민국

이용자는 아래의 조건을 따르는 경우에 한하여 자유롭게

- 이 저작물을 복제, 배포, 전송, 전시, 공연 및 방송할 수 있습니다.

다음과 같은 조건을 따라야 합니다:



저작자표시. 귀하는 원저작자를 표시하여야 합니다.



비영리. 귀하는 이 저작물을 영리 목적으로 이용할 수 없습니다.



변경금지. 귀하는 이 저작물을 개작, 변형 또는 가공할 수 없습니다.

- 귀하는, 이 저작물의 재이용이나 배포의 경우, 이 저작물에 적용된 이용허락조건을 명확하게 나타내어야 합니다.
- 저작권자로부터 별도의 허가를 받으면 이러한 조건들은 적용되지 않습니다.

저작권법에 따른 이용자의 권리는 위의 내용에 의하여 영향을 받지 않습니다.

이것은 [이용허락규약\(Legal Code\)](#)을 이해하기 쉽게 요약한 것입니다.

[Disclaimer](#)

치의과학박사 학위논문

Investigation of developmental mechanisms and
establishment of treatment strategies:
3D morphometric analysis of midface anomalies
in a mouse model of Apert syndrome

에이퍼트 증후군 모델 마우스 얼굴 기형의 3차원 형태
분석을 통한 발병 기전 규명 및 치료법 제시

2021년 2월

서울대학교 대학원

치의과학과 분자유전학 전공

김 봉 수

Investigation of developmental mechanisms and
establishment of treatment strategies:
3D morphometric analysis of midface anomalies in
a mouse model of Apert syndrome

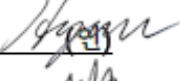
에이퍼트 증후군 모델 마우스 얼굴 기형의 3차원 형태
분석을 통한 발병 기전 규명 및 치료법 제시

지도교수 류 현 모

이 논문을 치의과학박사 학위논문으로 제출함
2020 년 12 월

서울대학교 대학원
치의과학과 분자유전학전공
김 봉 수

김봉수의 박사학위논문을 인준함
2021 년 1 월

위 원 장	_____	박 주 철	 (인)
부 위 원 장	_____	류 현 모	 (인)
위 원	_____	최 제 용	 (인)
위 원	_____	이 진	 (인)
위 원	_____	최 강 영	

ABSTRACT

Investigation of pathogenic mechanisms and
establishment of treatment strategy:

3D morphometric analysis of midface anomalies in a
mouse model of Apert syndrome

BONG-SOO KIM

Department of Molecular Genetics & Dental Pharmacology

The Graduate School of Seoul Nation University

(Directed by Prof. Hyun-Mo Ryoo, D.D.S., Ph.D.)

Apert syndrome, caused by activating mutation in the FGFR2 gene commonly presents craniosynostosis, midface hypoplasia and respiratory problems. Unfortunately, the pathological mechanism and intrinsic contributing factor still remain unclear, and there is no cure

but serial surgical treatment in the earliest stage of the patient's life. In this study, we analyzed the causal factors of midface hypoplasia in Apert syndrome mouse model with three-dimensional morphometric analysis and histological assessment. Moreover, we suggested the therapeutic and surgical target for Apert syndrome treatment.

We used *Fgfr2*^{S252W/+} mice as a mouse model of Apert syndrome. In part 1, we found the premature fusion of anterior facial bones is the main contributing factor toward the anterior-posterior skull length shortening. The facial anomalies are closely related to the abnormal cranial base growth, which could possibly induce the airway obstruction. The inhibition of Peptidyl-prolyl *cis-trans* isomerase NIMA-interacting 1 (PIN1), a downstream signaling enzyme of FGF/FGFR signaling, via genetic knockdown or use of a PIN1 inhibitor, juglone, attenuated the facial deformities in mouse model.

In part 2, we applied chondrocyte-specific *Fgfr2*^{S252W} mutation in mice (*Col2a1-cre; Fgfr2*^{S252W/+}) to examine the effect of cartilaginous component in the midface hypoplasia. These mice showed normal skull shape at birth, however, hypoplastic phenotypes were progressively evident. Especially, abnormal growth of nasal bone, vomer and ethmoid bone was notably presented, suggesting the

involvement of altered nasal septal cartilage in the midface hypoplasia. *Fgfr2*^{S252W} mutation on the septum chondrocytes accelerated hypertrophy and enlarged cellular size, finally, thickened and altered septal cartilage shape caused facial deformities.

In this study, we provided the pathological mechanisms for midface hypoplasia in Apert syndrome by detailed three-dimensional morphometric and histological analysis. Furthermore, we suggested targeting PIN1 and surgical correction of abnormal nasal septal cartilage as a treatment strategy for Apert syndrome patients. We expect these multidimensional observations and analyses on the mouse model of Apert syndrome could help the patients with syndromic craniosynostosis to reduce the risk of surgical process and have better prognosis.

Key words: Apert syndrome, midface hypoplasia, PIN1, nasal septum, 3D morphometric analysis, chondrocyte hypertrophy

Student number: 2014–22043

CONTENTS

I. Literature review

I.1. FGF signaling · · · · ·	1
I.2. Evolution of FGFRs · · · · ·	1
I.3. Role of FGFR in skeletal development · · · · ·	2
I.4. Activating mutations on FGFR2 · · · · ·	4
I.5. Symptoms of syndromic craniosynostosis · · · · ·	6
I.6. Midface hypoplasia · · · · ·	7
I.7. Therapeutic approaches for FGF/FGFR–induced syndromic craniosynostosis · · · · ·	9
I.8. Peptidyl–prolyl <i>cis–trans</i> isomerase NIMA–interacting (PIN1) · · · · ·	9
I.9. PIN1 and FGF signaling in the skeletal development · ·	11
I.10. PIN1 inhibitors · · · · ·	13

II. Purpose of study	14
III. Part 1	15
PIN1 attenuation improves midface hypoplasia in a mouse model of Apert syndrome	
IV. Part 2	68
Role of septal cartilage on midface hypoplasia of Apert syndrome	
V. Conclusion	129
VI. References	130
VII. 국문 초록	145

List of Figures

Part 1. PIN1 attenuation improves midface hypoplasia in a mouse model of Apert syndrome

[Figure 1–1] Landmarks on 3D image P0 mouse skull

[Figure 1–2] Cranial suture fusion and cranial base flexion were repaired by PIN1 inhibition

[Figure 1–3] Increased proliferation around coronal suture was rescued by *Pin1* haplodeletion

[Figure 1–4] PIN1 inhibiting effect does not show significant difference in wild-type mice

[Figure 1–5] Improved craniofacial phenotypes of *Fgfr2*^{S252W/+} by genetic or pharmacological PIN1 inhibition

[Figure 1–6] The discriminant function analysis for skull shape variance

[Figure 1–7] The shape changes of the face and the cranial base in *Fgfr2*^{S252W/+} mice were partially restored by PIN1 inhibition

[Figure 1–8] The discriminant function analysis for cranium shape changes of each mouse group

[Figure 1–9] Reduced facial length of *Fgfr2*^{S252W/+} mice by PIN1 inhibition

[Figure 1–10] Facial deformities manifested in *Fgfr2*^{S252W/+} mice were rescued by *Pin1* haplodeficiency or Juglone treatment

[Figure 1–11] Abnormal facial suture growth was repaired by PIN1 inhibition

[Figure 1–12] Altered mandibular growth in the *Fgfr2*^{S252W/+} mice was recovered by haplodeletion of *Pin1*

[Figure 1–13] Abnormal flexion of cranial base in *Fgfr2*^{S252W/+} mice was recovered by genetic *Pin1* depletion or Juglone treatment

[Figure 1–14] Correlation between skull length and cranial base angle

[Figure 1–15] Endocranial shape changes in *Fgfr2*^{S252W/+} mice

[Figure 1–16] Synchronosis growth in the cranial base was not impaired in *Fgfr2*^{S252W/+} mice at P0 stage

[Figure 1–17] A correlation of shape deformities between the face and the cranial base in *Fgfr2*^{S252W/+} mice

[Figure 1–18] Narrowed and irregular airway due to retroflexed

cranial base was attenuated by genetic *Pin1* haplodeletion

Part 2. Role of septal cartilage on midface hypoplasia of Apert syndrome

[Figure 2-1] Craniofacial landmarks for the morphometric analysis

[Figure 2-2] Landmarks on the nasal septal cartilage for 3D shape analysis

[Figure 2-3] Cranial anomalies on *EIIa-SW* and *Col2-SW*

[Figure 2-4] Histology of coronal suture of the *Fgfr2*^{S252W} mutant mice

[Figure 2-5] The genotypic ratio of each mutant mouse.

[Figure 2-6] Linear measurements of craniofacial bones

[Figure 2-7] Morphometric analysis of skull at P0

[Figure 2-8] Morphometric analysis of skull at P7

[Figure 2-9] Morphometric analysis of whole skull, cranium and face at P21

[Figure 2-10] DFA for skull and facial shape variance at P21

[Figure 2–11] The facial shape variance of each group by PCA

[Figure 2–12] Abnormal obliteration of the suture between premaxilla and maxilla bone

[Figure 2–13] Deviated snout of the mutant mice at P21

[Figure 2–14] Reduced formation of ethmoid bone in the mutant mice

[Figure 2–15] *Col1-SW* showed mild craniofacial phenotypes

[Figure 2–16] *Fgfr2^{S252W}* mutation affects to the vomer growth via changed nasal septum growth

[Figure 2–17] Altered septum and vomer growth may induce the fusion of vomer and premaxilla bone

[Figure 2–18] Chondrocyte-derived factors influencing bone formation were not affected by *Fgfr2^{S252W}* mutation

[Figure 2–19] Deviation of the nasal septum and the snout in the mutant mice

[Figure 2–20] Correlation between the deviation of the nasal septum and the snout

[Figure 2–21] Thickening of the nasal septal cartilage

[Figure 2–22] SOX9 expression was reduced by *Fgfr2^{S252W}* mutation

on the septum chondrocytes

[Figure 2–23] RUNX2 expression was increased by *Fgfr2*^{S252W} mutation on the septum chondrocytes

[Figure 2–24] Chondrocyte hypertrophy markers were increased with *Fgfr2*^{S252W} mutation

[Figure 2–25] Increased septum chondrocyte size in *Col2*–*SW*

[Figure 2–26] Increased tracheal cartilage density in *EIIa*–*SW*

List of Tables

Part 1. PIN1 attenuation improves midface hypoplasia in a mouse model of Apert syndrome

[Table 1–1] Description of landmarks on the mouse craniofacial and categorization by modules: cranium, face and cranial base

[Table 1–2] Procrustes ANOVA for the effect of measurement error on skull shape variation

[Table 1–3] Procrustes analysis for overall skull shape variance between each group

[Table 1–4] Procrustes analysis of variance for shape of groups of three parts of skull: cranium, face and cranial base

Part 2. Role of septal cartilage on midface hypoplasia of Apert syndrome

[Table 2–1] Landmark descriptions used on the craniofacial shape analysis

[Table 2–2] Landmark descriptions used on the nasal septal cartilage

shape analysis

[Table 2–3] Primers used for quantitative real–time PCR

[Table 2–4] Craniofacial suture fusion frequency at P0 and P7 stages

[Table 2–5] Premaxilla–vomer closure and palate perforation frequency at P7 and P21 stages

Abbreviations

FGF fibroblast growth factor

FGFR fibroblast growth factor receptor

PIN1 peptidyl-prolyl *cis-trans* isomerase NIMA-interacting 1

Micro-CT Micro-computerized tomography

PCA principal components analysis

DFA discriminant function analysis

PLA partial least square analysis

EIIa-SW *EIIa-cre; Fgfr2^{S252W/+}*

Col2-SW *Col2a1-cre; Fgfr2^{S252W/+}*

Col1-SW *Colla1-cre; Fgfr2^{S252W/+}*

BMP bone morphogenetic protein

IHH indian hedgehog

VEGF vascular epithelial growth factor

TGF β 1 transforming growth factor beta 1

ECM-1 extracellular matrix protein-1

RUNX2 runt-related transcription factor 2

PCNA proliferating cell nuclear antigen

I. Literature review

I.1. FGF signaling

Fibroblast growth factors (FGFs) are growth factors with diverse biological functions by binding to tyrosine kinase FGF receptors (FGFRs) (Ornitz and Itoh 2001). Interaction of FGFRs and FGFs induces the phosphorylation of specific cytoplasmic tyrosine residues and triggers downstream pathways. FGF signaling regulate various biological process, including cell growth, migration, differentiation, survival, and apoptosis. FGF/FGFR signaling is also essential for earliest stage of development, organ formation and skeletogenesis. FGF/FGFR signals mainly activate the ERK1/2, P38 and JNK pathway (Bradshaw and Dennis 2010).

I.2. Evolution of FGFRs

The FGFR family members (FGFR1–4) show high amino acid homology in human (~55–72%). These four FGFR genes have been identified in vertebrates including humans, mice and zebrafish. One *C. elegans* *Fgfr* gene *egg laying defective 15 (egl-15)* and two *D. melanogaster* *Fgfr* genes (*breathless* and *heartless*) have been

identified. These invertebrate Fgfrs share relatively low amino acid identity with their vertebrate homologs (Itoh and Ornitz 2004).

FGFR1–3 undergo alternative splicing of the IgIII domain to produce variants that have distinct ligand–binding specificities. Those variants are differentially expressed in epithelial and mesenchymal lineages. It is essential to the biological functions of the FGF signaling system (Powers et al. 2000). In general, FGFRb splice variants are found in epithelial tissues and FGFRc splice variants are found in mesenchymal tissues (Ornitz and Marie 2015).

I.3. Role of FGFRs in skeletal development

FGFR1 is expressed in the early limb bud. Later, FGFR1 is expressed prominently in hypertrophied cartilage, osteocytes and osteoblasts (Peters et al. 1992). *Fgfr1*–deficient mice show severe growth retardation, and died during gastrulation due to impaired mesodermal differentiation (Deng et al. 1994). Mice with deletion of FGFR1 in limb bud mesenchymal cells also showed reduced limb skeleton, missing digits or died at birth (Harfe et al. 2004; Perantoni et al. 2005).

FGFR2 is expressed in condensing mesenchyme of early limb bud (Orr–Urtreger et al. 1993; Peters et al. 1992). In developing bone, FGFR2 is predominantly expressed in perichondrial and periosteal tissue (Yu et al. 2003). In development, FGFR1 and FGFR2 are expressed in pre–osteoblast and osteoblast (Delezoide et al. 1998; Iseki et al. 1997). FGFR2IIIb variant is expressed primarily by epithelial cells (Powers et al. 2000) and FGFR2IIIc variant is expressed in mesenchyme origin cells in mesenchymal condensates and during endochondral and intramembranous ossification (Eswarakumar et al. 2002). FGFR2 is a positive regulator for osteoblast differentiation, and Runx2, the master transcription factor for bone formation, is downstream of FGFR2 signaling (Miraoui et al. 2009). *Fgfr2IIIc*^{-/-} mice showed reduced ossification and it was related with decreased Osteopontin and Runx2 (Eswarakumar et al. 2002). FGFR1 and FGFR2 are also highly expressed in preosteoblasts and osteoblasts in the osteogenic front during calvaria bone development (Ornitz and Marie 2015). The FGFR2c splice variant is expressed in early mesenchymal condensations and then in sites of intramembranous ossification (Eswarakumar et al. 2002). Activating mutation of FGFR2 is known to boost differentiation of pre–osteoblast or immature osteoblast and expand their pool (Ornitz

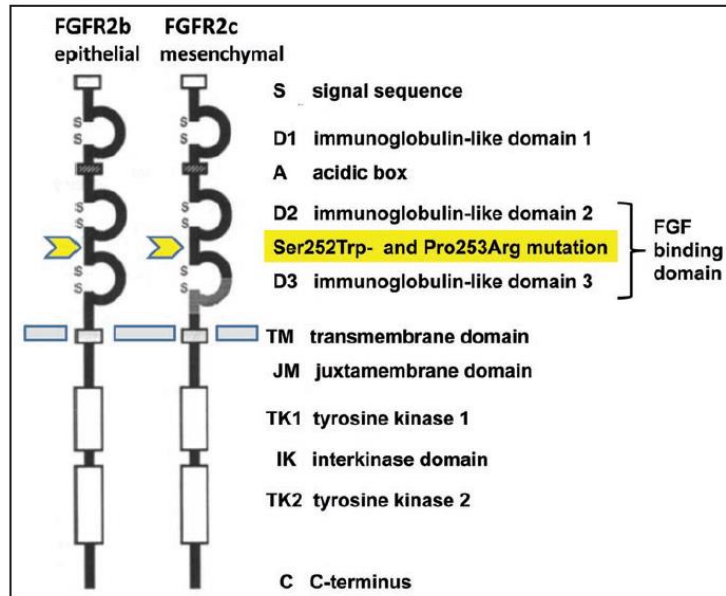
and Marie 2015). Gain-of-function mutation of FGFR2 mutations have variable effects on cranial suture development in mice and humans and cause multiple types of craniosynostosis, such as Apert syndrome, Crouzon syndrome and Pfeiffer syndrome (Wilkie 2005).

FGFR3 is mainly expressed in reserve and proliferating chondrocytes in the epiphyseal growth plate (Peters et al. 1993; Szebenyi et al. 1995). FGFR3 negatively regulates chondrogenesis in endochondral bone formation, while promote chondrocyte terminal hypertrophic differentiation (Minina et al. 2002; Murakami et al. 2004; Sahni et al. 1999). Gain-of-function mutations in FGFR3 cause skeletal dysplasia, including achondroplasia (ACH) and hypochondroplasia (HCH) exhibiting smaller body size (Ornitz and Marie 2002).

I.4. Activating mutations on FGFR2

Apert syndrome (MIM 101200) is a genetic disorder that occurs in approximately one out of 65,000 births (Czeizel et al. 1993). It mainly presents craniosynostosis, midface hypoplasia, and syndactyly. Most of Apert syndrome cases are caused by the Ser252Trp or Pro253Arg missense mutations in the

FGFR2 gene. This region in the *FGFR2* gene corresponds to the region between



FGFR2 isoforms, FGFR2b and FGFR2c, and the structure of FGFR2. Activating mutations inducing Apert syndrome are located in the linker region between D2 and D3. (Melnik 2009)

immunoglobulin-like domain 2 and 3 where FGF ligands bind (Johnson and Wilkie 2011). Therefore, these mutations result in the loss of affinity in ligand-receptor interactions and subsequent hyper-activation of downstream signaling (Kim et al. 2003a; Kim et al. 2003b; Yu et al. 2000). FGFR1-3 genes are most common genes involved in syndromic craniosynostosis (Wilkie 2005). A mouse model carrying the activating mutations on FGFRs successfully mimic craniosynostosis phenotype (Lee et al. 2019). Among them, since

mutation on FGFR2 is commonly related with craniofacial syndromes, mouse models for *Fgfr2c*^{C342Y/+} or *Fgfr2c*^{W290R/+} (Crouzon syndrome), and *Fgfr2*^{S252W/+} or *Fgfr2*^{P253R/+} (Apert syndrome) are available (Chen et al. 2003; Eswarakumar et al. 2004; Mai et al. 2010; Wang et al. 2005). Common phenotypes of these mouse models are early fusion of coronal suture, midface hypoplasia, brachycephaly, which mimics the human disease phenotype. These mutations on FGFR2 altered osteoblast proliferation, differentiation and apoptosis (Eswarakumar et al. 2004). Activated Erk1/2 and p38 signaling are known to participate in the regulation of coronal suture by FGFR2 (Wang et al. 2010; Yin et al. 2008). Protein kinase C (PKC) signaling is also important in the FGFR2-promoted osteogenic differentiation (Miraoui et al. 2009).

I.5 Symptoms of syndromic craniosynostosis

Calvaria expands during childhood to accommodate the growing brain. Cranial sutures, consisted with undifferentiated mesenchyme between each plate of calvarial bones, act as a growth center of calvaria. Craniosynostosis describes the premature fusion of one or more cranial sutures. Consequently, skull shapes are distorted due to

lack of growth to the fused suture, and compensatory overgrowth at the non-fused sutures. (Johnson and Wilkie 2011). Craniosynostosis is found between 1 in 2,100 and 1 in 2,500 birth (Boulet et al. 2008). Most genetically determined craniosynostosis are autosomal dominant in inheritance, but around half of cases are from sporadic mutations. The genes most frequently mutated were *FGFRs*, *TWIST* and *EFNB1* (Johnson and Wilkie 2011). Among them, mutations on *FGFR2* and *FGFR3* are associated more than 50% of cases. *FGFR2* is mainly expressed in osteoprogenitors and differentiating osteoblasts in the osteogenic front of calvarial bones (Britto et al. 1998). Craniosynostosis-induced raised intracranial pressure causes clinical manifestations such as somnolence, irritability, vomiting. (Fadda et al. 2015). There are also retrusion of the orbital region, associated with hypertelorism, eyelid antimongoloid, proptosis and eyebrow cleft.

I.6. Midface hypoplasia

With craniosynostosis, the most common clinical symptom found in the patients with Apert syndrome is midface hypoplasia, including palatal defects, retruded maxilla and underdeveloped nasal organs

(Johnson and Wilkie 2011). Syndromic synostosis patients commonly present breathing problems due to airway obstruction (Ahmed et al. 2008). Almost 50% of patients are suffered from obstructive sleep apnoea, which is majorly caused by midface hypoplasia and distorted nasopharyngeal airway (Nout et al. 2012). Because the pharynx is small and the nasal cavity is narrowed, severe respiratory distress will be caused, especially during the neonatal period when patients are nasal breathers (Fadda et al. 2015). Moreover, 30% of Apert syndrome patients show clefting of the soft palate or uvula. Delayed or ectopic tooth eruption, cross bite and dental crowding are common features (Fadda et al. 2015). Unfortunately, despite relatively high disease frequency, there is no cure for craniosynostosis except for the serial surgical corrections in the early stage of life. Moreover, due to the unpredictable growth patterns, surgical correction could be repeated at a later age. Because midface consists of various bones, cartilage and fibrous tissues, multidisciplinary approaches are pursued (Fadda et al. 2015; Martelli et al. 2008)

I.7. Therapeutic approaches for FGF/FGFR–induced syndromic synostosis

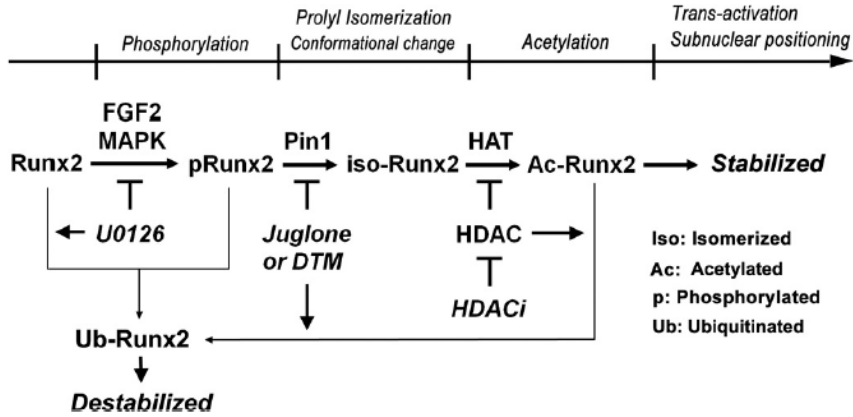
Many researchers have tried to rescue the cranial suture closure with targeting FGF/FGFR signaling. Shukla et al. demonstrated prevented suture closure by inhibiting ERK/MAPK pathway in the Apert syndrome mouse model (Shukla et al. 2007). Eswarakumar et al. described genetic and pharmacological approach for Crouzon syndrome mouse model by selective uncoupling between docking protein *Frs2 α* and *Fgfr2c*, resulting in prevented craniosynostosis (Eswarakumar et al. 2006). Soluble form of FGFR2IIIC, as a decoy receptor, also partially rescued craniosynostosis in Apert syndrome mouse (Morita et al. 2014). These studies may provide promising therapeutic strategies to reduce hyper–activated FGF signaling by FGFR2 mutations in craniosynostosis.

I.8. Peptidyl–prolyl cis–trans isomerase NIMA–interacting 1 (PIN1)

Protein phosphorylation regulates the activation of signaling cascades to control cell growth, proliferation and survival.

Phosphorylation on the specific residue often occurs conformational changes in protein kinases and their substrates, and it regulates protein activities in physiological process and disease (Pawson and Scott 2005). Peptidyl-prolyl *cis-trans* isomerase NIMA-interacting 1 (PIN1) (EC 5.2.1.8) is a member of the parvulin subfamily of peptidyl prolyl *cis-trans* isomerases (PPIases) family including other two subfamily, cyclophilins and FK506-binding proteins (FKBPs) (Gothel and Marahiel 1999; Lu et al. 1996). PIN1 specifically binds phosphorylated serine/threonine-proline motifs and catalyzes the isomerization between the *cis* and *trans*-conformation of the rigid peptide bonds in the proline backbone, thus modulating the activity, phosphorylation status, subcellular localization, or stability of its target proteins (Lu and Zhou 2007). Phosphorylated serine/threonine-proline residues is specifically recognized by PIN1, and inaccessible to conventional PPIases, such as cyclophilins and FK506-binding proteins (Gothel and Marahiel 1999). Pin1 is a ubiquitously expressed with multiple functions in different biological systems (Liou et al. 2011). This gene is well conserved in mouse, chicken and zebrafish.

I.9. Pin1 and FGF signaling in the skeletal development



Phosphorylated Runx2 by FGF–MAPK signaling is recognized and isomerized by Pin1. This structural change is critical for acetylation and stabilization of Runx2. (Yoon et al. 2013)

Among various functions, PIN1 has a critical role in skeletal development. Lee et al. firstly reported that *Pin1*^{-/-} mice showed abnormal bone formation, especially in older mice (Lee et al. 2009). Later, the important role of PIN1 in skeletal growth and remodeling in developmental stage has been found (Islam et al. 2017; Yoon et al. 2014; Yoon et al. 2013).

FGF/FGFR signaling is an essential in osteoblast differentiation, especially required for transactivation of RUNX2, the master transcription factor of bone development. Moreover, ERK/MAPK–

mediated phosphorylation of RUNX2 by FGF stimulation is critical step (Ge et al. 2009; Kim et al. 2003a; Park et al. 2010) . Subnuclear positioning of RUNX2 accelerated by FGF stimulation is required for osteoblast differentiation. Nuclear–matrix target sequence (NMTS) in the C–terminus of RUNX2 is essential for RUNX2–mediated recognition of the nuclear matrix (Zaidi et al. 2001; Zaidi et al. 2006). Moreover, PIN1 binding site is densely distributed around the NMTS, especially P409 is believed as a putative target residue of PIN1 (Yoon et al. 2014). Collectively, PIN1–mediated structural modification on RUNX2 stimulated from FGF signaling is indispensable axis for osteoblast differentiation and skeletal development (Yoon et al. 2014).

In the *Fgfr2*^{S252W/+} Apert syndrome mouse model, hyper–activated FGFR2 signaling increased the RUNX2 stability and the expression around the osteogenic front of coronal sutures. These phenotypes were rescued by inhibiting PIN1 activity in the mouse model (Shin et al. 2018).

I.10. PIN1 inhibitors

The PPIases have emerged as targets for a wide range of disease including cancer, neurodegenerative disease and peripheral neuropathy (Dunyak and Gestwicki 2016). Because they have so many potential substrates throughout the body, discovering drug is challenging field. Among them, due to the role of Pin1 in numerous diseases including cancer and neurodegeneration, finding inhibitors has been an ongoing pursuit (Moore and Potter 2013). Juglone, the firstly discovered PIN1 inhibitor produced by the black walnut tree, inhibits PIN1 activity by covalent modification of Cys-113 in the active site (Hennig et al. 1998). Interestingly, Juglone shows specific inhibitory action on PIN1, but not on the other PPIases, FKBP or cyclophilins, despite the high structural and sequence similarity between the active site of the PPIases (Dunyak and Gestwicki 2016). However, since Juglone has not been yet tested for clinical trials as its toxicity and water insolubility (National Institutes of Health 2020), studies for the proper dosage, modification of juglone or finding alternative drugs should be performed.

II. Purpose of the study

Midface hypoplasia is considered as the most challenging part of craniosynostosis management even in adult age. Since midface consisted with various bony and cartilaginous tissues, the intrinsic growth pattern need be well understood. Despite the high incidence of syndromic craniosynostosis, there is no cure but a series of risky surgical procedures in their childhood. In this study, we performed three-dimensional morphological analysis of the craniofacial phenotypes of Apert syndrome mouse model to elucidate the causal factor of midface hypoplasia. To suggest the therapeutic target of craniosynostosis and midface hypoplasia, PIN1, a mediator of FGF/FGFR signaling, was regulated genetically or pharmacologically. Furthermore, to define the intrinsic cartilaginous factor for facial deformities, cartilage-specific mutant mice were examined during growth. The purpose of this study is to provide the pathological mechanisms of midfacial deformity, and to suggest the therapeutic target of syndromic craniosynostosis.

III. Part 1

PIN1 Attenuation Improves Midface Hypoplasia in a Mouse Model of Apert Syndrome

This research was originally published in the Journal of Dental Research, 2020, Vol. 99(2) 223–232

Abstract

Premature fusion of the cranial suture and midface hypoplasia are common features of syndromic craniosynostosis caused by mutations in the *FGFR2* gene. The only treatment for this condition involves a series of risky surgical procedures designed to correct defects in the craniofacial bones, which must be performed until brain growth has been completed. Several pharmacological interventions directed at FGFR2 downstream signaling have been tested as potential treatments for premature coronal suture fusion in a mouse model of Apert syndrome. However, there are no published studies that have targeted for the pharmacological treatment of midface hypoplasia. We used *Fgfr2*^{S252W/+} knock-in mice as a model of Apert syndrome, and

used morphometric analyses to identify causal hypoplastic sites in the midface region. 3D geometric and linear analyses of *Fgfr2*^{S252W/+} mice at postnatal day 0 demonstrated distinct morphological variance. The premature fusion of anterior facial bones such as the maxilla, nasal, and frontal bones, rather than the cranium or cranial base is the main contributing factor toward the anterior–posterior skull length shortening. The cranial base of the mouse model had a noticeable downward slant around the intersphenoid synchondrosis, which is related to distortion of the airway. Within a skull, the facial shape variance was highly correlated with the cranial base angle change along *Fgfr2* S252W mutation–induced craniofacial anomalies. The inhibition of an FGFR2 downstream signaling enzyme, PIN1, via genetic knockdown or using a PIN1 inhibitor, Juglone, attenuated the aforementioned deformities in a mouse model of Apert syndrome. Overall, these results indicate that FGFR2 signaling is a key contributor toward abnormal anterior–posterior dimensional growth in the midface region. Our study suggests a novel therapeutic option for the prevention of craniofacial malformations induced by mutations in the *FGFR2* gene.

Introduction

Apert syndrome is a rare genetic disorder that occurs in approximately one out of 65,000 births; however, it is a relatively common craniofacial anomaly (Czeizel et al. 1993). It is mainly characterized by craniosynostosis, midface hypoplasia, and syndactyly. Most of Apert syndrome cases are caused by the Ser252Trp or Pro253Arg missense mutations in the *FGFR2* gene. This region in the *FGFR2* gene corresponds to the region between immunoglobulin-like domain 2 and 3 where FGF ligands bind (Johnson and Wilkie 2011). Therefore, these mutations result in the loss of specificity in ligand-receptor interactions and subsequent hyper-activation of downstream signaling (Kim et al. 2003a; Kim et al. 2003b; Yu et al. 2000). Constitutively active FGFR2 signaling accelerates the proliferation and differentiation of osteoblasts in the craniofacial sutures, causing early fusion of the sutures (Su et al. 2014). With craniosynostosis, the most common clinical symptom of Apert syndrome patients is midface hypoplasia, including symptoms of palatal defects, retruded maxilla and underdeveloped nasal organs (Johnson and Wilkie 2011). It is also closely associated with airway obstruction (Ahmed et al. 2008). Even if multidisciplinary approaches

are pursued (Martelli et al. 2008), there is no currently reliable approach except for the serial surgical corrections of the skull malformations in the earliest stage of the patients' life. Also, few studies have attempted the pharmacological approaches for midfacial anomaly treatment.

Previous studies have reported the causal factors of craniosynostosis and identified therapeutic targets. The emerging role of p38 MAPK pathway in Apert syndrome has been demonstrated (Wang et al. 2010), and the inhibitor of ERK/MAPK tested for prevented closure of the cranial suture synostosis in a mouse model of Apert syndrome (Shukla et al. 2007; Yin et al. 2008). Likewise, the intermediate regulator of FGF pathway could be a target of Apert syndrome treatment.

Peptidyl-prolyl *cis-trans* isomerase NIMA-interacting 1 (PIN1) (EC 5.2.1.8) catalyzes the isomerization between the *cis* and *trans*-conformation of the rigid peptide bonds in the proline backbone, thus leading to the conformational change of its target proteins (Lu and Zhou 2007). Our previous studies demonstrated the crucial role of PIN1 in regulating bone development by controlling the transcriptional activity of RUNX2, a key transcription factor and

especially, FGF/FGFR signaling-mediated RUNX2 activation and stability at the post-translational level (Yoon et al. 2014; Yoon et al. 2013). Within the same results, we recently demonstrated the prevention of early coronal suture fusion by PIN1 inhibition and its underlying molecular mechanism (Shin et al. 2018). In this study, we investigated whether genetic or pharmacological attenuation of PIN1 could prevent midface hypoplasia of mouse model of Apert syndrome, *Fgfr2*^{S252W/+}. Mechanistically, we conducted detailed quantitative analyses to observe the pattern of midface shape changes and its relationship with other part of the skull.

Materials and methods

Generation of mutant mice and experimental design

A mouse carrying ploxPneo cassette, which blocks expression of the mutant *Fgfr2* allele (*Fgfr2*^{neoS252W/+} mouse, FVB background) (Shukla et al. 2007) was bred with *Pin1*^{+/-} mouse (C57BL/6) (Fujimori et al. 1999) to generate *Fgfr2*^{neo252W/+}; *Pin1*^{+/-} mouse. Cre recombinase from *EIIa-Cre* mouse (B6.FVB-TgN (EIIa-cre) C3739Lm, #003724, Jackson Laboratory) removes pLoxpneo to allow expression of the mutant allele (Shukla et al. 2007). The

littermates including *Fgfr2*^{S252W/+}; *Pin1*^{+/-} mice were only used to reduce the variance between the littermates. Mice used from our previous work (Shin et al. 2018) were included in this study. All mice were maintained under specific pathogen-free conditions. All experiments were performed in accordance with Institutional Animal Care and Use Committee policies and Special Committee on Animal Welfare of Seoul National University (Seoul, Republic of Korea).

Pharmacological Inhibition of PIN1

For the inhibition of PIN1 enzymatic activity, we used a pharmacological inhibitor, Juglone (5-hydroxy-1,4 naphthoquinone) (cat. 420120, Calbiochem, Darmstadt, Germany), as previously described (Shin et al. 2018). Briefly, pregnant mice were intraperitoneally injected with Juglone (1 mg/kg) once a day from E14.5 to E18.5. The number of littermates was unaffected with 1 mg/kg of Juglone injection (Shin et al. 2018). Newborn mice were euthanized and examined for further studies.

3D image processing and landmark placing

Newborn mice were euthanized and dissected heads were fixed with 4% paraformaldehyde. Micro-computed tomography (Micro-CT) scans were acquired by using SMX-90CT (SHIMAZU, Kyoto, Japan) (35 μm /pixel, 70 kVp, 89 μA). 3D modeling was performed by using CT Analyzer (Brucker, Billerica, MA) and three-dimensional coordinates from 42 craniofacial landmarks (Figure 1-1 and Table 1-1 (Richtsmeier laboratory, Pennsylvania state university) and (Wei et al. 2017)) were recorded by using Landmark Editor 3.0v (IDAV, University of California, Davis). Due to relatively low Micro CT resolution for newborn mice, measurement error was checked by Procrustes AVONA (Klingenberg and McIntyre 1998). Landmark placing was done twice on two separately taken images to test measurement error. Subsequently, the four-set of landmarks were averaged. Image reconstruction and three-dimensional linear and angular measurements were performed using TRI 3D-BON software (RACTOC System Engineering Co, Tokyo, Japan).

Statistical and shape analyses

Landmark coordinates were Procrustes-transformed to remove the effect of scaling, rotation and translation (Klingenberg 2011). After

generating covariance matrices, Principle component analysis (PCA) was performed to visualize patterns of shape variation within and among groups. PCA performs a coordinate rotation that aligns the principal axes (PCs) with the directions of maximum variation. The wireframe images representing the mean shape of each group were generated by using discriminant function analysis (DFA). To analyze the distribution of a set of shapes between groups, Procrustes ANOVA was performed. Landmarks were assigned to the three-subsets (blocks) (cranium, face and cranial base) to analyze associated shape changes between the different modules of the skull by using Two-block partial least squares (PLS), which identifies the features of shape covariation between the blocks (Rohlf and Corti 2000). Statistical significance test for DFA and PLS analysis was computed via permutation tests against the null hypothesis of independence with 10,000 rounds of number of randomization. All geometric morphometric analyses were performed in Morpho J v 1.06d (Klingenberg 2011). For linear and angular measurements, Data are presented as the mean \pm standard deviation. Statistical analysis was performed using one-way ANOVA followed by Bonferroni's correction or Newman-Keuls multiple comparison test using Prism 5.0 software (GraphPad, San Diego, CA). $p \leq 0.05$ was

considered significant.

Histological analysis

The specimens were decalcified with 10% EDTA (pH 7.4) solution for 24 h. Dehydration and paraffin infiltration were conducted using an automated tissue processor (TP1020, Leica, Wetzlar, Germany). For thorough infiltration of paraffin into the nasopharyngeal space, the edge of temporal bone was carefully sliced off. Embedded tissues were cut to 5 μm thick sections using a rotary microtome (RM2145, Leica, Wetzlar, Germany) and stained with Hematoxylin and Eosin (H&E). For immunohistochemistry, the slides were subjected to antigen retrieval in citrate buffer for 10 minutes at 90° C. PCNA (sc-56, Santa Cruz), COL2A1 (sc-52658, Santa Cruz, Dallas, TX) and Collagen Type X (234196, Millipore) were detected. All images were acquired using a digital micro-imaging camera (DP72, Olympus, Tokyo, Japan) under a microscope (BX51, Olympus, Tokyo, Japan). PCNA positive cells in resting zone of synchondrosis were counted from three of WT and *Fgfr2*^{S252W/+} mice each by using ImageJ (NIH, USA). Significance was calculated by Student t-test.

Results

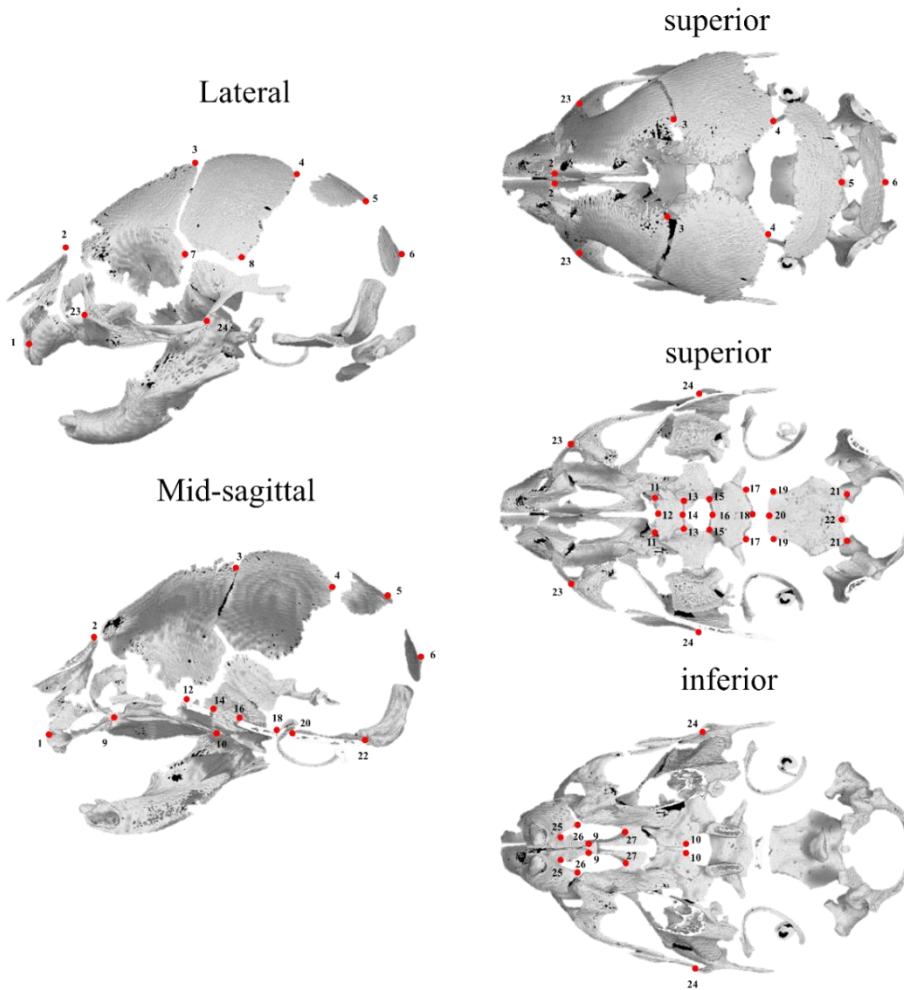


Figure 1–1. Landmarks on 3D image of P0 mouse skull

42 landmarks were assigned on the cranium, face and cranial base for three-dimensional analysis.

Table 1–1. Description of landmarks on the mouse craniofacial and categorization by modules: cranium, face and cranial base

No.	Description	Module
1	Point A, anterior–most point of alveolus of upper incisor, left and right side (<i>A</i>)	face
2	Nasion, intersection of nasal bone, caudal point, left and right side (<i>N</i>)	face, cranium
3	Most medial intersection of the frontal and parietal bones, taken on the frontal, left and right side	cranium
4	Most postero–medial point on the parietal bone, left and right side	cranium
5	Caudal–most point of interparietal bone at mid–sagittal plane	cranium
6	Caudal–most point of occipital bone at mid–sagittal plane (<i>Oc</i>)	cranium
7	Most superior point on the squamous temporal, intersection of the coronal suture, left and right side	cranium
8	Most postero–inferior point on the parietal bone, left and right side	cranium
9	Caudal–most point of premaxilla bone at mid–sagittal plane, left and right side (<i>Pm</i>)	face
10	Caudal–most point of palatine bone at mid–sagittal plane, left and right side (<i>P</i>)	base
11	Most anterior, dorsal point on the anterior projection on the presphenoid, left and right side	base

12	Rostral, dorsal–most point of pre–sphenoid bone at mid–sagittal plane (<i>Ps</i>)	base
13	Most postero–lateral, dorsal point of corner of the presphenoid bone, left and right side	base
14	Caudal, dorsal–most point of pre–sphenoid bone at mid–sagittal plane (<i>Ps'</i>)	base
15	Most antero–lateral, dorsal point of corner of the basisphenoid bone, left and right side	base
16	Rostral, dorsal–most point of basi–sphenoid bone at mid–sagittal plane (<i>Bs</i>)	base
17	Most postero–lateral, dorsal point of corner of the basisphenoid bone, left and right side	base
18	Caudal, dorsal–most point of basi–sphenoid bone at mid–sagittal plane	base
19	Most antero–lateral, dorsal point of corner of the basioccipital bone, left and right side	base
20	Rostral, dorsal most point of basioccipital bone at mid–sagittal plane	base
21	Most postero–lateral, dorsal point of corner of the basioccipital bone, left and right side	base
22	Basion, caudal, dorsal–most point of basi–occipital bone at mid–sagittal plane (<i>Ba</i>)	base
23	Anterior notch on zygomatic process, left and right side (<i>Zm</i>)	face
24	Intersection of zygoma with zygomatic process of temporal, left and right side	face
25	Most anterior point of the anterior palatine foramen, left and right side	face

26	Most infero-lateral point of the premaxillary-maxillary suture, taken on premaxilla, left and right side	face
27	Most posterior point of the anterior palatine foramen, left and right side	face

Measurement error

Procrustes ANOVA results show that the mean squares for individual variation (2.7×10^{-4}) exceeded the error for imaging (3.7×10^{-5}) and repeated landmark placing (3.8×10^{-5}), which indicates that measurement error is negligible (Table 1–2).

Table 1–2. Procrustes ANOVA for the effect of measurement error on skull shape variation

Effect	SS	MS	df	F	P
Individual	0.4237025 6	0.000277837 7	152 5	4.1 6	<.000 1
Imaging (error 1)	0.1166671 9	0.000037707 6	309 4	0.9 7	0.809 7
Repeat (error 2)	0.2398303 2	0.000038757 3	618 8		

Fgfr2^{S252W} mice showed midface shortening and cranial base flexion, which were improved by genetic or pharmacological PIN1 inhibition

Micro-CT images of the lateral skull (Figure 1-2, upper lane) indicate that sutural spaces between the fronto-nasal (white arrow) and maxillary bones (white arrowhead) are almost filled in *Fgfr2*^{S252W/+} mice. Genetic attenuation of *Pin1* by heterogenous mating and PIN1 inhibitor, Juglone treatment on *Fgfr2*^{S252W/+} mice yielded a decrease in the degree of premature fusion in facial sutures that was comparable to WT mice. As shown in Figure 1-3, we confirmed that increased proliferation around the osteogenic front of coronal suture in *Fgfr2*^{S252W/+} mice was alleviated by haplodeletion of *Pin1*. Because there were no significant shape differences between WT, *Pin1*^{+/-} and Juglone treated-WT mice, (Figure 1-4), we did not focus on *Pin1*^{+/-} and Juglone-WT groups in this study. According to Micro-CT images of the mid-sagittal plane of skull (Figure 1-2, lower lane), the cranial base of *Fgfr2*^{S252W/+} mice was abruptly bent near the intersphenoid synchondrosis (ISS) (yellow arrowhead) and the premaxilla bone was raised up, resulting in a high palatal arch (asterisk). However, the bent appearance of the cranial base was not observed in *Fgfr2*^{S252W/+}; *Pin1*^{+/-} mice and Juglone-treated *Fgfr2*^{S252W/+} mice (yellow line). The PCA analysis showed clear

separation of *Fgfr2*^{S252W/+} mice from WT by skull shape variance along PC axes (Figure 1-4A). Wireframe image of *Fgfr2*^{S252W/+} mice showed shortened facial length, abnormally bent cranial base and increased skull width. Notable separation was also shown in *Pin1*-haplodeleted or Juglone-treated *Fgfr2*^{S252W/+} group in comparison with *Fgfr2*^{S252W/+} mice mainly along the PC1 axis (Figure 1-4C and D). Although these two groups were not completely overlapped with WT (Figure 1-4E), they were clearly separated from *Fgfr2*^{S252W/+} group and appeared to be moving toward WT (Figure 1D). The shape distribution between each group was statistically significant (Figure 1-5 and Table 1-3).

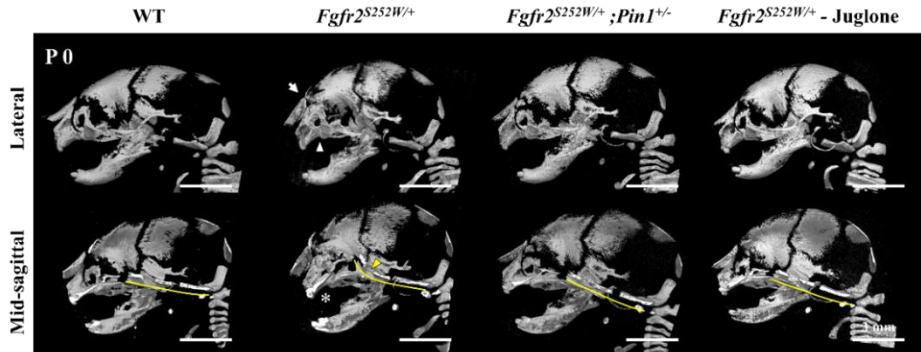


Figure 1–2. Craniofacial suture fusion and cranial base flexion were repaired by PIN1 inhibition

Micro-CT images of wild-type (WT), $Fgfr2^{S252W/+}$, $Fgfr2^{S252W/+}; Pin1^{+/-}$ and Juglone-treated $Fgfr2^{S252W/+}$ mice skull at postnatal day 0 (P0) stage. The upper panel shows the representative lateral view of skull. The spaces between the frontal, nasal and maxilla bones are almost closed in $Fgfr2^{S252W/+}$ mice (white arrow and arrowhead) while the other two genotypes show patency. The lower panel shows the mid-sagittal sectional view. The cranial base of $Fgfr2^{S252W/+}$ mice was abruptly bent around the ISS (yellow arrowhead and line), while the cranial base was flat in the other two genotypes (yellow line). $Fgfr2^{S252W/+}$ mice also showed steeper premaxilla than the in other two genotypes (asterisk). For detailed analyses of cranial base, see Figure 1–11. The skull shape variance of WT and $Fgfr2^{S252W/+}$

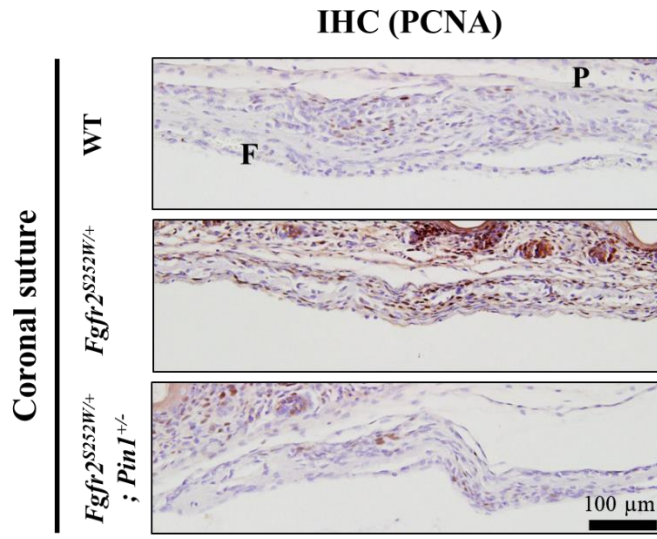


Figure 1–3. Increased proliferation around coronal suture was rescued by *Pin1* haplodeletion

Immunohistochemistry of PCNA on coronal suture region. Increased PCNA positive cells at osteogenic front between frontal (F) and parietal (P) bones of *Fgfr2^{S252W/+}* mouse were recovered to WT level by *Pin1* haplodeletion (*Fgfr2^{S252W/+}; Pin1^{+/-}*).

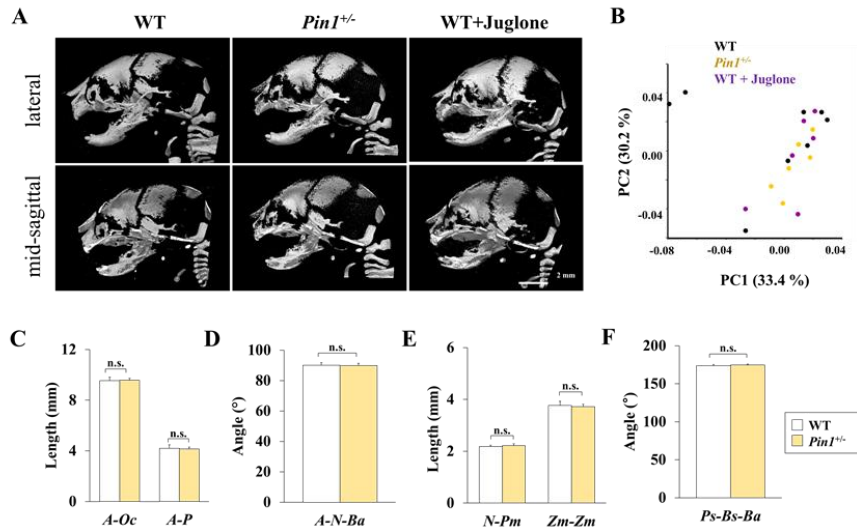
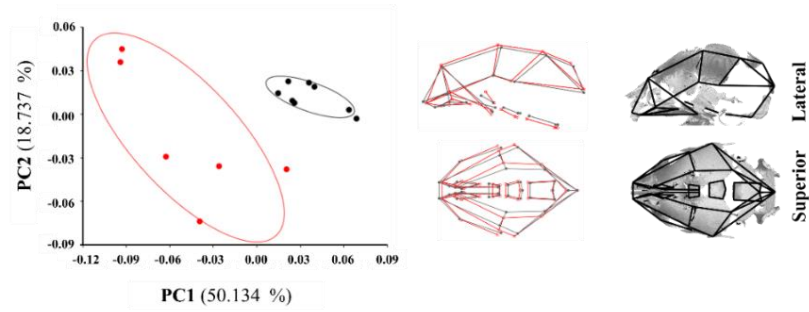
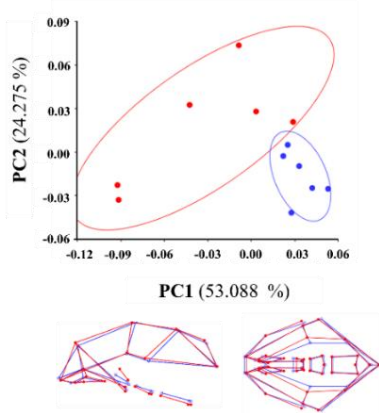
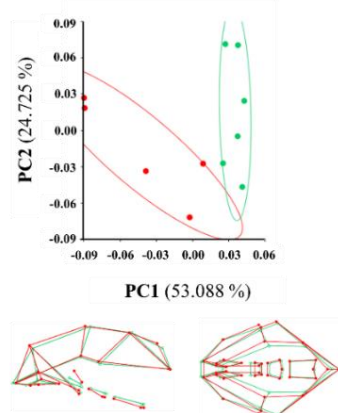
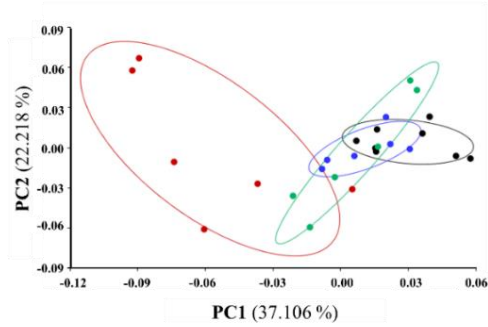
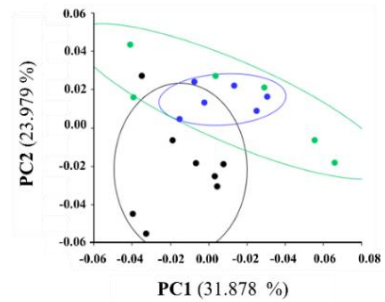


Figure 1–4. PIN1 inhibiting effect does not show significant difference in wild–type mice

Comparison between the skull phenotypes of WT, *Pin1*^{+/-} and Juglone–treated WT mice. **(A)** Micro CT images of WT, *Pin1*^{+/-} and Juglone–treated WT mice at lateral and mid–sagittal view. No notable morphological difference was found. **(B)** PCA from landmarks (Figure 1–1) on the skull of WT, *Pin1*^{+/-} and Juglone–treated WT mice. These three groups were not separated by skull shape variance. **(C–F)** Linear and angular measurements of WT and *Pin1*^{+/-}. Total skull length (*A–Oc*), facial length (*A–P*), angle between (*A–N–Ba*), facial height (*N–Pm*) and width (*Zm–Zm*) and cranial base angle (*Ps–Bs–Ba*). Details of landmarks are described on Figure 1–1. ($n \geq 6$, n.s: non–significant)

A**B****C****D****E**

● WT ● *Fgfr^{2S252W/+}* ● *Fgfr^{2S252W/+}; Pin1^{+/-}* ● *Fgfr^{2S252W/+} + Juglone*

Figure 1–5. Improved craniofacial phenotypes of *Fgfr2*^{S252W/+} by genetic or pharmacological PIN1 inhibition

The skull shape variance of WT and *Fgfr2*^{S252W/+} (A), *Fgfr2*^{S252W/+} and *Fgfr2*^{S252W/+}; *Pin1*^{+/-} (B), *Fgfr2*^{S252W/+} and Juglone–treated *Fgfr2*^{S252W/+} (C), all groups (D) and WT, *Fgfr2*^{S252W/+}; *Pin1*^{+/-} and Juglone–treated *Fgfr2*^{S252W/+} groups (E) were analyzed by PCA. The percentage of total variance for each PC was displayed on the axis. Wireframe images in (A–C) indicating the mean skull shape of each genotype were generated by DFA, and the statistic results were provided on Figure 1–5. The color by groups for PCA plot and wireframe images is correspondent.

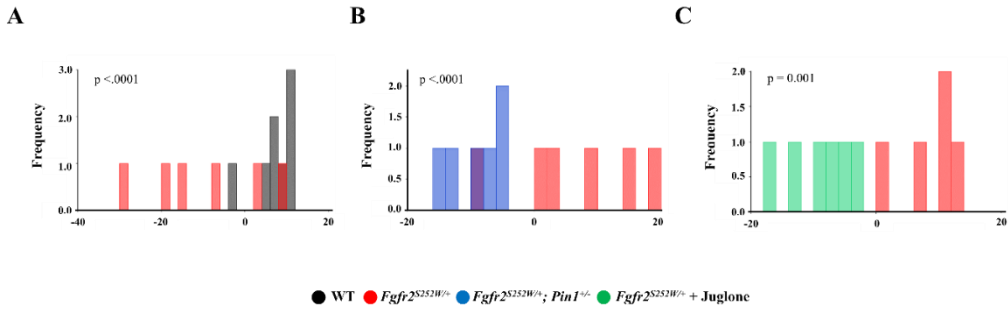


Figure 1–6. The discriminant function analysis for skull shape variation.

Cross-validation scores for comparison between WT and *Fgfr2*^{S252W/+} (A), WT and *Fgfr2*^{S252W/+}; *Pin1*^{+/-} (B) and WT and *Fgfr2*^{S252W/+} – Juglone treated group (C) were analyzed. P-value for 10,000 permutation test using Procrustes distance is showed on each graph.

Table 1–3. Procrustes analysis for overall skull shape variance between each group.

Groups	Effect	SS	MS	df	F	P
S252W/WT	Group	0.028776 3	0.000471 74	61	41.8 2	<.000 1
	Side	0.004601 6	0.000079 33	58	7.03	<.000 1
	Group*Side	0.000654 3	0.000011 28	58	0.24	1.000
S252W– Pin1 /S252W	Group	0.017520 2	0.000287 21	61	22.8 9	<.000 1
	Side	0.001772 9	0.000030 56	58	2.44	0.000 4
	Group*Side	0.000727 8	0.000012 54	58	0.34	1.000
S252W– JUG /S252W	Group	0.019625 6	0.000321 73	61	22.4 7	<.000 1
	Side	0.002138 5	0.000036 87	58	2.57	0.000 2
	Group*Side	0.000830 6	0.000014 32	58	0.32	1.000
S252W– Pin1 /S252W– JUG/WT	Group	0.011844 5	0.000097 08	122	4.95	<.000 1
	Side	0.003847 9	0.000066 34	58	3.38	<.000 1
	Group*Side	0.002276 0	0.000019 62	116	0.63	0.999 1
ALL	Group	0.040056 5	0.000218 88	183	12.7 6	<.000 1
	Side	0.004947 9	0.000085 30	58	4.97	<.000 1
	Group*Side	0.002983 7	0.000017 14	174	0.45	1.000

* SS, sum of squares; MS, mean squares; df, degree of freedom

* WT, wild type (black); S252W, *Fgfr2*^{S252W/+} (red); S252W–Pin1, *Fgfr2*^{S252W/+}; *Pin1*^{+/-} (blue); S252W–JUG, *Fgfr2*^{S252W/+} – Juglone (green)

The shape changes of the face and the cranial base in *Fgfr2*^{S252W/+} mice were partially restored by PIN1 inhibition.

To examine the effect of *Fgfr2*^{S252W} mutation on each part of skull and its recovery by PIN1 inhibition, the skull was divided into three sub-groups including cranium, face and cranial base (Table 1-1), and PCA was performed on each sub-group. While the separation of the cranium shapes between groups was not apparent (Figure 1-6A), both the facial and the cranial base shapes were clearly separated between *Fgfr2*^{S252W/+} and the other groups along the PC1 axis (Figure 1-6B and C). Wireframe images also displayed the shape changes including shortened facial length, increased facial height and width (Figure 1-6B) and down-flexed cranial base (Figure 1-6C) along *Fgfr2*^{S252W/+} group corresponded PC1 axis. PIN1-inhibited groups were distinguished from these phenotypes, and the shape of each part of skull appear to be moving towards the WT (Figure 1-6B, C and Figure 1-7). From Procrustes analyses (Table 1-4), we found the facial shape was most significantly changed by Fgfr2 S252 mutation (F = 67.80) followed by cranial base (F = 32.32) and cranium (F = 21.60). Linear measurements of mouse skull on antero-posterior axis also showed drastically shortened facial length (*A-P*) of *Fgfr2*^{S252W/+} mice but mild effect on cranium and cranial base length

(Figure 1–8). However, shortened facial and skull length significantly rescued to WT level in the *Fgfr2*^{S252W/+}; *Pin1*^{+/-} mice. These results indicate that the morphological changes found in the anterior midface of *Fgfr2*^{S252W/+} mice played the main role in the decreased skull length in *Fgfr2*^{S252W/+} mice. Moreover, PIN1 inhibition significantly improved facial and overall craniofacial abnormalities.

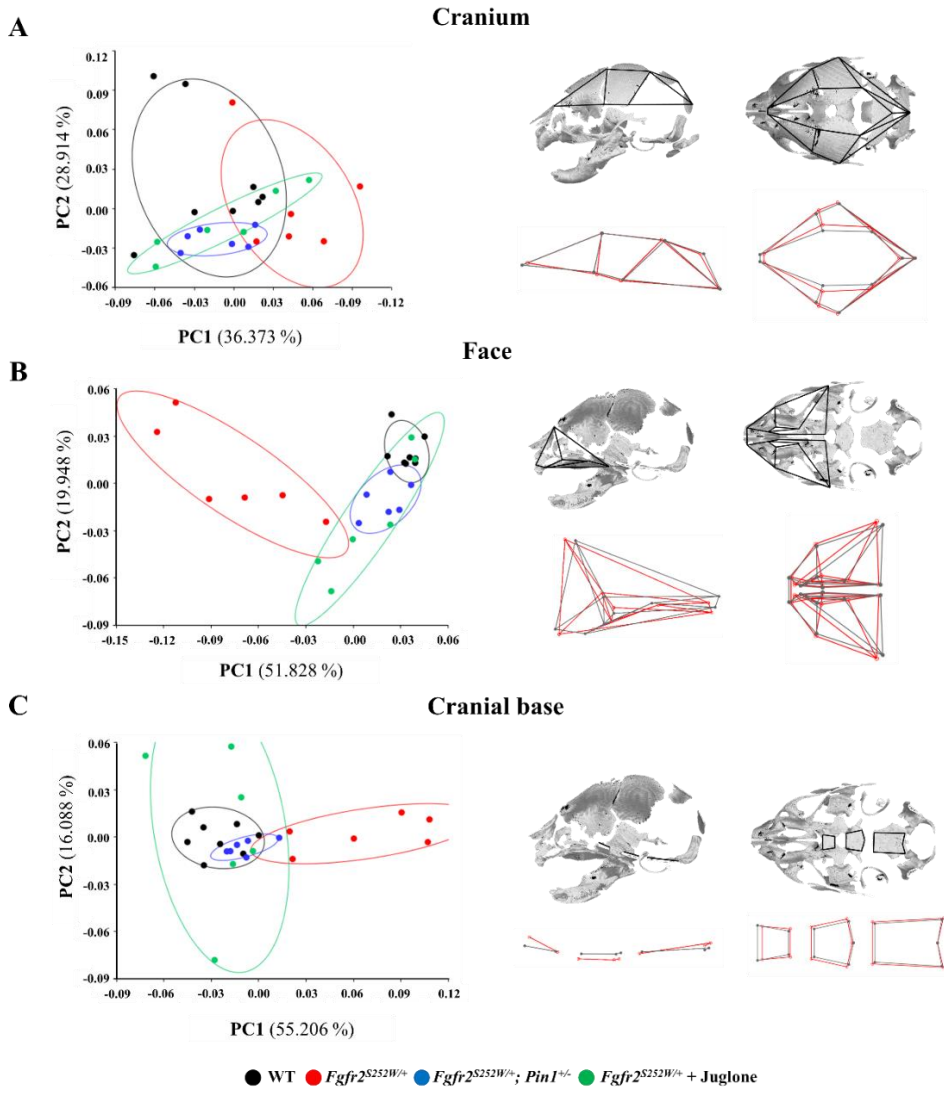


Figure 1–7. The shape changes of the face and the cranial base in *Fgfr2*^{S252W/+} mice were partially restored by PIN1 inhibition.

Principal component analysis was performed to analyze the shape changes of three main part of skull; (A) the cranium, (B) the face and (C) the cranial base. Mean shape changes of each module by Fgfr2 S252W mutation compare to WT were represented with wireframe images by DFA. DFA results for other groups and statistics were provided on Figure 1–7.

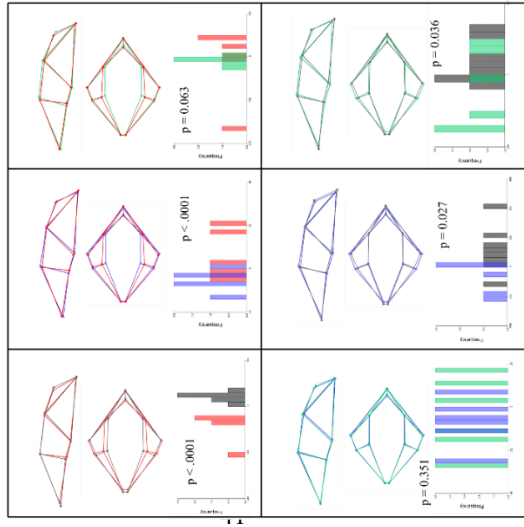
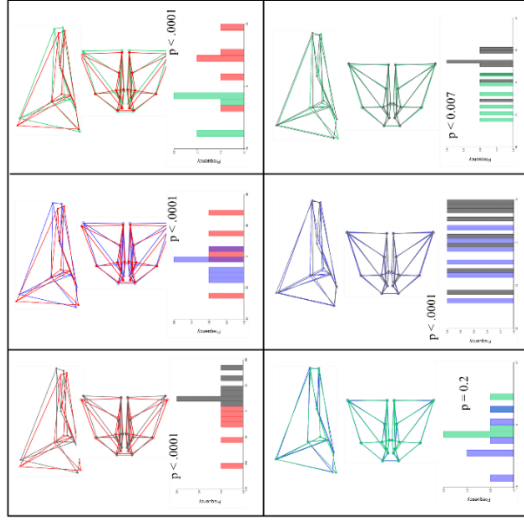
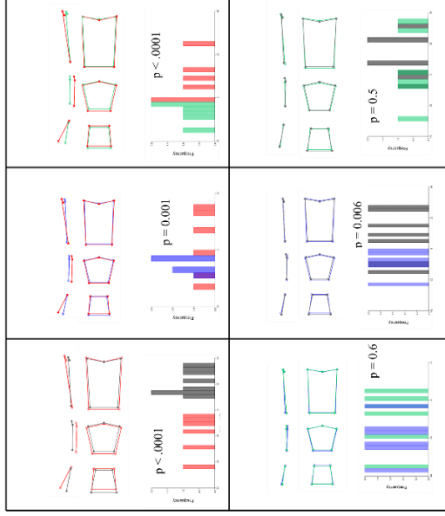
A**B****C**

Figure 1–8. The discriminant function analysis for cranium shape changes of each mouse group. Comparison of average cranium (A), face (B) and cranial base (C) shape of each pair of groups was represented by wireframe images at lateral and superior view, and cross-validation score graph was inserted below with P-value from 10,000 permutation test using Procrustes distance.

Table 1–4. Procrustes analysis of variance for shape of groups of three parts of skull: cranium, face and cranial base

	Groups	SS	MS	df	F	P
Cranium	S252W/WT	0.02029	0.0013530	15	21.60	<.0001
	S252W– Pin1 /S252W	0.01330	0.0008868	15	7.37	0.0003
	S252W– JUG /S252W	0.01158	0.0007722	15	4.22	0.0051
	S252W– Pin1 /S252W– JUG/WT	0.01728	0.0005761	30	2.92	0.0027
	ALL	0.03559	0.0007911	45	4.97	<.0001
Face	S252W/WT	0.04364	0.0018974	23	67.80	<.0001
	S252W– Pin1 /S252W	0.03023	0.0013147	23	75.43	<.0001
	S252W– JUG /S252W	0.02654	0.0011541	23	31.13	<.0001
	S252W– Pin1 /S252W– JUG/WT	0.01349	0.0002933	46	9.09	<.0001
	ALL	0.05964	0.0008643	69	28.89	<.0001
Cra	S252W/WT	0.03121	0.0017339	18	32.32	<.0001

	S252W– Pin1 /S252W	0.01856	0.0010315	18	20.94	<.0001
	S252W– JUG /S252W	0.02650	0.0014724	18	42.41	<.0001
	S252W– Pin1 /S252W– JUG/WT	0.00492	0.0001369	36	4.07	<.0001
	ALL	0.04114	0.0007619	54	19.14	<.0001

* SS, sum of squares; MS, mean squares; df, degree of freedom

* WT, wild type (black); S252W, *Fgfr2*^{S252W/+} (red); S252W–Pin1, *Fgfr2*^{S252W/+}; *Pin1*^{+/-} (blue);

S252W–JUG, *Fgfr2*^{S252W/+} – Juglone (green)

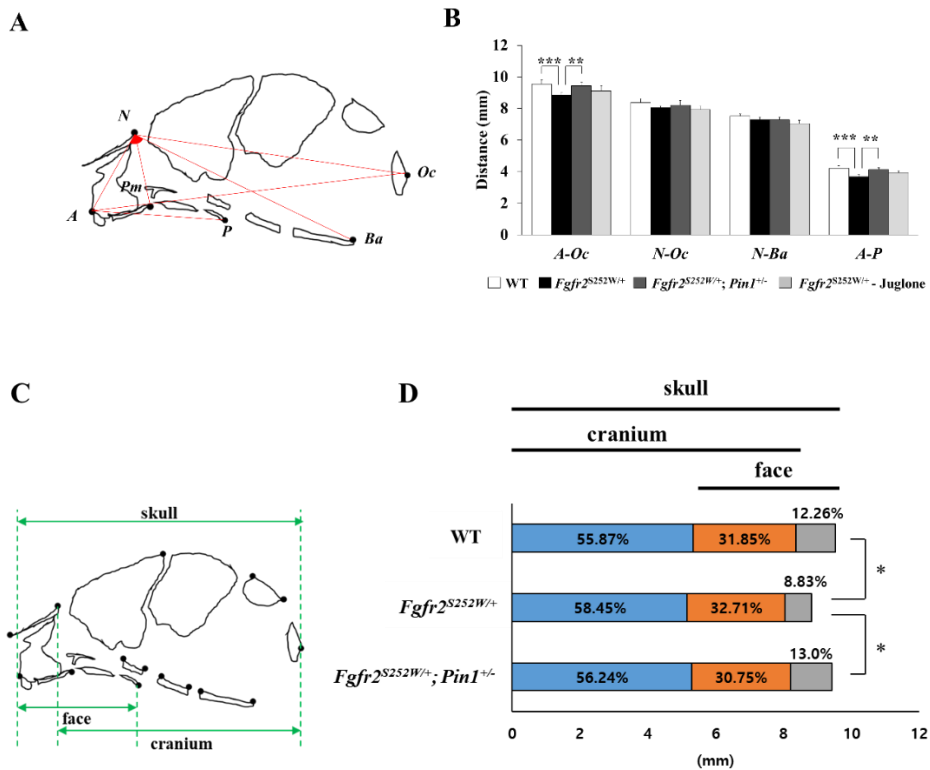


Figure 1–9. Rescued facial length of *Fgfr2*^{S252W/+} mice by PIN1 inhibition

(A) The depiction of landmark points for analyzing the skull and midface at the mid-sagittal plane. (B) Anterior-posterior dimensional skull analyses. *A–Oc*: skull length, *N–Oc*: calvarial length, *N–Ba*: cranial base length, *A–P*: facial length. (C and D) The ratio of face (orange + grey bar) and cranium (blue + orange bar) length in total skull length. (* $p \leq 0.05$, ** $p \leq 0.01$, *** $p \leq 0.001$).

Abnormalities on anterior facial development in *Fgfr2*^{S252W/+} mice were alleviated by PIN1 inhibition

Since we confirmed shortening of the anterior facial region as a major contributor of midface hypoplasia in *Fgfr2*^{S252W/+} mice, facial growth profile was observed. Linear measurement results showed increased facial height (Figure 1-9B), width (Figure 1-9C) and altered facial position (Figure 1-9D) in *Fgfr2*^{S252W/+} mice, and they were rescued by PIN1 inhibition. In *Fgfr2*^{S252W/+} mice, facial suture development was notably impaired (Figure 1-10A). The premaxillo-maxillary suture and maxilla-palatine suture are almost obliterated (Figure 1-10B). On the contrary, the inter-premaxillary suture was fused in most of the WT mice, but was patent or partially fused in *Fgfr2*^{S252W/+} mice (Figure 1-10B). This abnormal suture growth in *Fgfr2*^{S252W/+} mice completely or partially recovered to WT levels after PIN1 attenuation. Collectively, altered facial suture growth might result the anterior facial shortening and compensatory increase in facial height and width in *Fgfr2*^{S252W/+} mice. Generally, midface hypoplasia found in Apert-type craniosynostosis causes mandibular prognathism (Wink et al. 2013). An anterior cross-bite was observed in *Fgfr2*^{S252W/+} mice, which indicates relative mandibular prognathism (Figure 1-2). We performed mandibular

linear and angular measurements as described in Figure 1-10A. Total mandibular body length was significantly shortened in *Fgfr2*^{S252W/+} mice (*B-Go* in Figure 1-10B). Among the anterior- (*B-Me*), mid- (*Me-An*) and posterior- (*An-Go*) mandibular body length, a significant difference was only found in the mid-mandibular (*Me-An*) length ($p \leq 0.005$). Genetic *Pin1* haplodeletion returned the *Me-An* length to WT-level and alleviated the shortening observed in the *B-Go* length. In addition to shortening of mandibular body, the gonial angle (*Me-Go-Co*) is significantly decreased ($p \leq 0.05$) in *Fgfr2*^{S252W/+} mice. This was partially alleviated by genetic *Pin1* haplodeletion, but it was not statistically significant (Fig. 1-10C). All these deformities that occurred in the anterior midface development of *Fgfr2*^{S252W/+} mice were alleviated by *Pin1* haplodeletion.

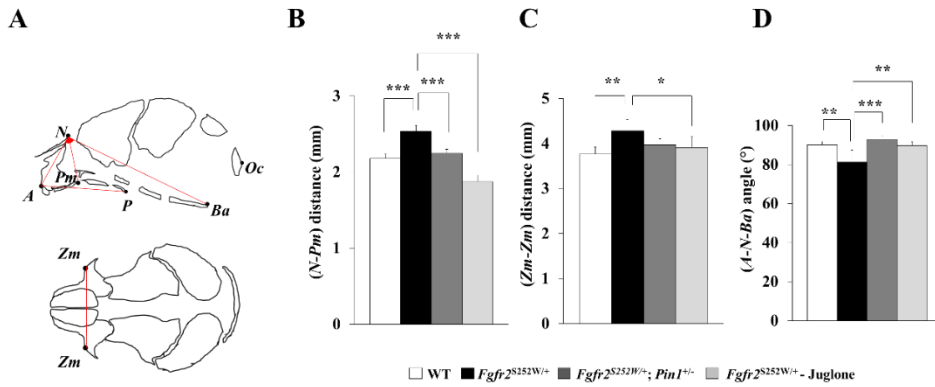


Figure 1–10. Facial deformities manifested in *Fgfr2^{S252W/+}* mice were rescued by *Pin1* haplodeficiency or Juglone treatment

(A) The depiction of landmark points for analyzing the skull and midface at the mid-sagittal plane and superior view. (B) *N-Pm* indicates the facial height. (C) The distance between *Zm-Zm* indicates the facial width. (D) The angle, *A-N-Ba* indicates a relationship between the most anterior point of the maxilla, *A*, and the cranial base, *N-Ba*. ($*p \leq 0.05$, $**p \leq 0.01$, $***p \leq 0.001$)

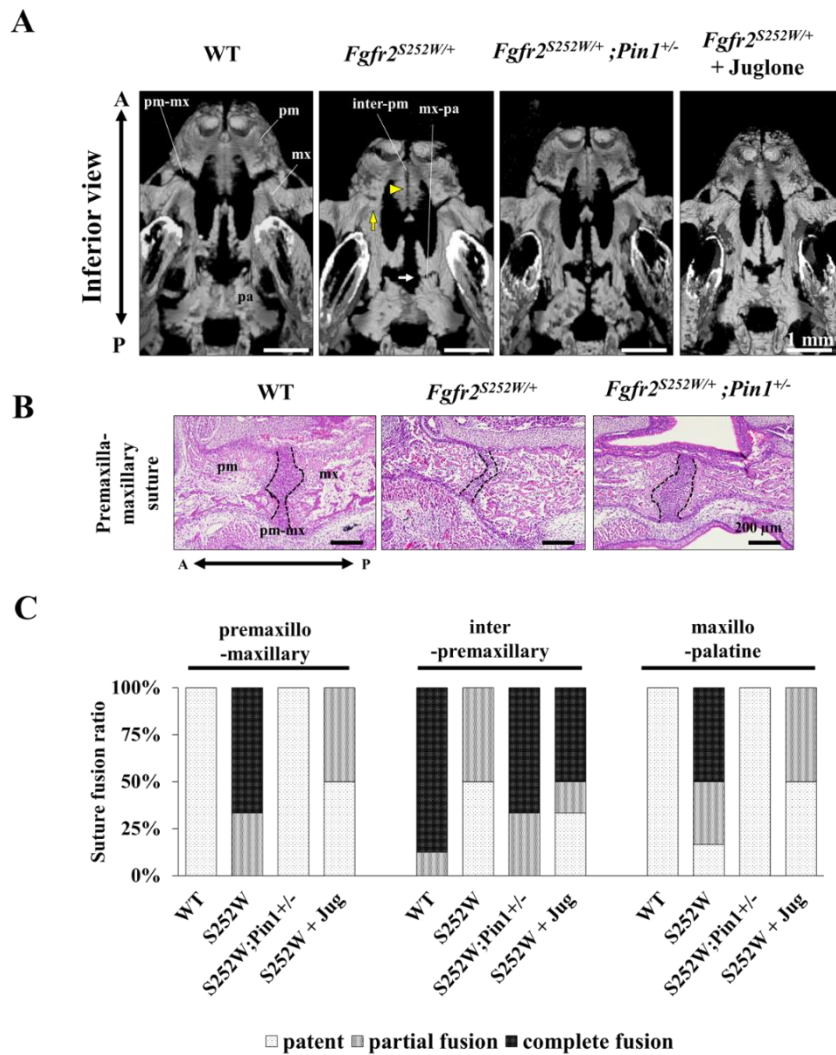


Figure 1–11. Abnormal facial suture growth was repaired by PIN1 inhibition

(A) Micro-CT images showing an inferior view of the midface. *Fgfr2*^{S252W/+} mice showed complete or partial fusion of premaxilla-maxillary suture (yellow arrow), patent or widened inter-premaxillary suture (yellow arrowhead) and partial fusion of maxilla

and palatal bone (white arrow). pm, premaxilla; mx, maxilla; pa, palatine; pm-mx, premaxillo-maxillary suture; inter-pm, inter-premaxillary suture; mx-pa, maxillary-palatine suture.

(B) Hematoxylin/Eosin staining of premaxillo-maxillary suture on sagittal plane. Black dotted line indicates the boundary of each bone.

(C) The patency of premaxillo-maxillary, inter-premaxillary, and maxillary-palatine sutures are analyzed. Suture patency was counted as a ratio (the number of animal of the phenotype/total number of animal in the group), S252W/+ for *Fgfr2*^{S252W/+}; S252W; *Pin1*^{+/-} for *Fgfr2*^{S252W/+}; *Pin1*^{+/-} and S252W+Jug for juglone-treated *Fgfr2*^{S252W/+} mice.

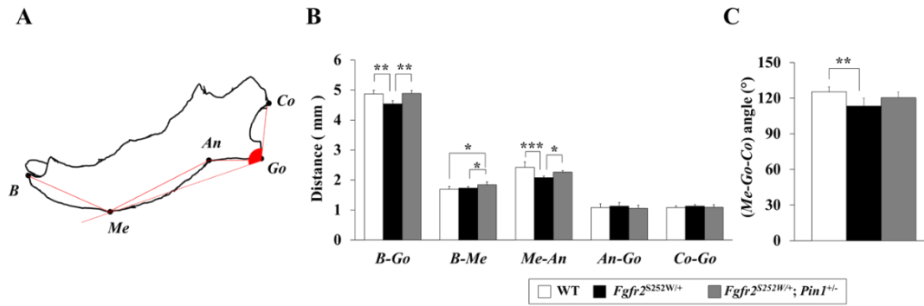


Figure 1–12. Altered mandibular growth in the *Fgfr2*^{S252W/+} mice was recovered by haplodeletion of *Pin1*

(A) Schematic depiction of mandibular landmarks. (B) *B-Go*, mandibular body length; *B-Me*, anterior mandibular body length; *Me-An*, mid-mandibular body length; *An-Go*, posterior mandibular body length; *Co-Go*, mandibular height were analyzed. (C) Gonial angle (*Me-Go-Co*) was analyzed. (n=8 for WT and n=6 for the others, statistical analysis performed using Student's *t-test*, **p*<0.05, ***p*<0.005) (B, inferior rim point on lower incisor alveolus; Me, menton, inferior point on mandibular symphysis; An, antegonial notch, concavity at the inferior surface of the mandible; Go, gonion, tip of mandible angle; Co, posterior-most point of condyle)

Abnormal flexion of cranial base in *Fgfr2*^{S252W/+} mice was recovered by genetic *Pin1* depletion or Juglone treatment

As demonstrated in Figure 1–2, *Fgfr2*^{S252W/+} mice showed an abrupt flexion in the cranial base around the intersphenoid synchondrosis, which cause angular and locational change of presphenoid bone. Unlike the other three genotypes, the point *Ps* of *Fgfr2*^{S252W/+} mice is always located vertically higher than *Ps'* in an individual animal. Some *Fgfr2*^{S252W/+} mice showed the *Ps* point above the (*N–Ba*) line (Figure 1–11A and B). This abnormality is also demonstrated by the angle between the (*Ps–Bs*) and (*Bs–Ba*) lines (Figure 1–11C). While this angle is almost 180° in WT mice, it decreases significantly in *Fgfr2*^{S252W/+} mice. Upon *Pin1* haplodeletion or Juglone treatment, this angle returns to a level that is comparable to WT mice. The posterior part of the premaxilla was abruptly raised up in *Fgfr2*^{S252W/+} mice (Figure 1–2, lower lane, asterisk). This noticeable change, represented by the angle between the line extension of (*A–Pm*) and cranial base line (*N–Ba*) was significantly alleviated by genetic or pharmacological inhibition of *Pin1* (Figure 1–11D). The degree of cranial base flexion showed close correlation with skull length (Figure 1–12). The pattern showed that the more curved cranial base, the shorter total skull length in *Fgfr2*^{S252W/+} mice. The

endocranial area was effected by abnormal cranial development and cranial base flexion (Figure 1–13A). 3D–reconstructed images of endocranial area reflected shortening and heightening of cranium, while the ventral part was expanded probably due to bent down cranial base. Reduced Pin1 expression in *Fgfr2*^{S252W/+} partially recovered these phenotypes. Despite shortened skull (Figure 1–8), total endocranial volume was not significantly reduced in mutant mice (Figure 1–13B). Dorsal–ventral or lateral dimensional expansion might compensate the volume decrease. To observe the effect of chondrogenic growth change on the abnormal cranial base structure, we examined the cell proliferation and differentiation in synchondrosis of *Fgfr2*^{S252W/+} mice at P0 stage. However, proliferation (Figure 1–14A) or chondrogenesis (Figure 1–14B) in the synchondrosis was not significantly different from WT. These results presumably indicate that abnormal cranial base growth mainly caused as a secondary effect by cranial or facial shape changes.

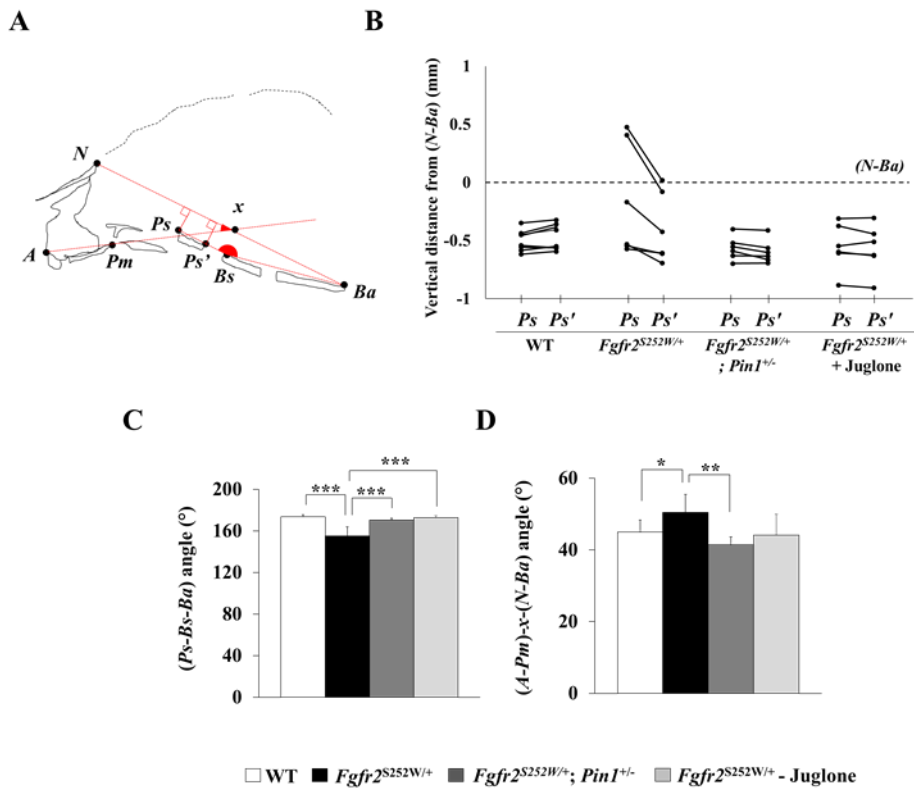


Figure 1–13. Abnormal flexion of cranial base in *Fgfr2*^{S252W/+} mice was recovered by genetic *Pin1* depletion or Juglone treatment

(A) Landmarks for angular measurements of the cranial base were depicted. (B) The location and vertical distance between the most anterior (*Ps*) and posterior (*Ps'*) points of the presphenoid bone from the (*N-Ba*) line were analyzed. Each *Ps* and *Ps'* from an individual animal is linked with a line. Negative value indicates that these points are located under the (*N-Ba*) line, whereas positive values indicate that they are located above the line. (C) The flexion of

cranial base was represented by the angle between ($Ps-Bs-Ba$). (D)
 The steepness of premaxilla was represented by the angle between
 the line ($A-Pm$) and the line ($N-Ba$). (* $p \leq 0.05$, ** $p \leq 0.01$, *** $p \leq 0.001$)

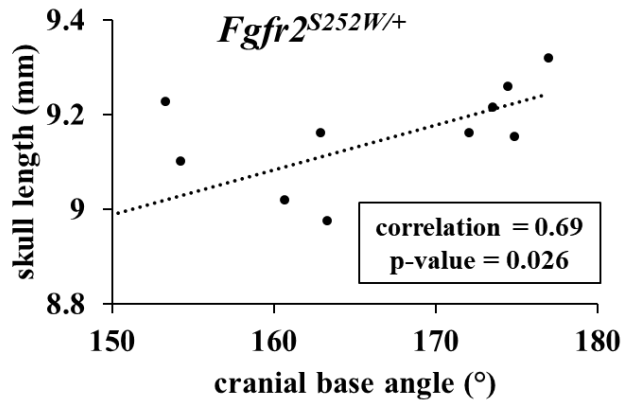


Figure 1-14. Correlation between skull length and cranial base angle

Correlation graph between total skull length ($A-Oc$ in Fig. 1-8) and
 the cranial base angle ($Ps-Bs-Ba$, Figure 1-11) in *Fgfr2^{S252W/+}* mice.

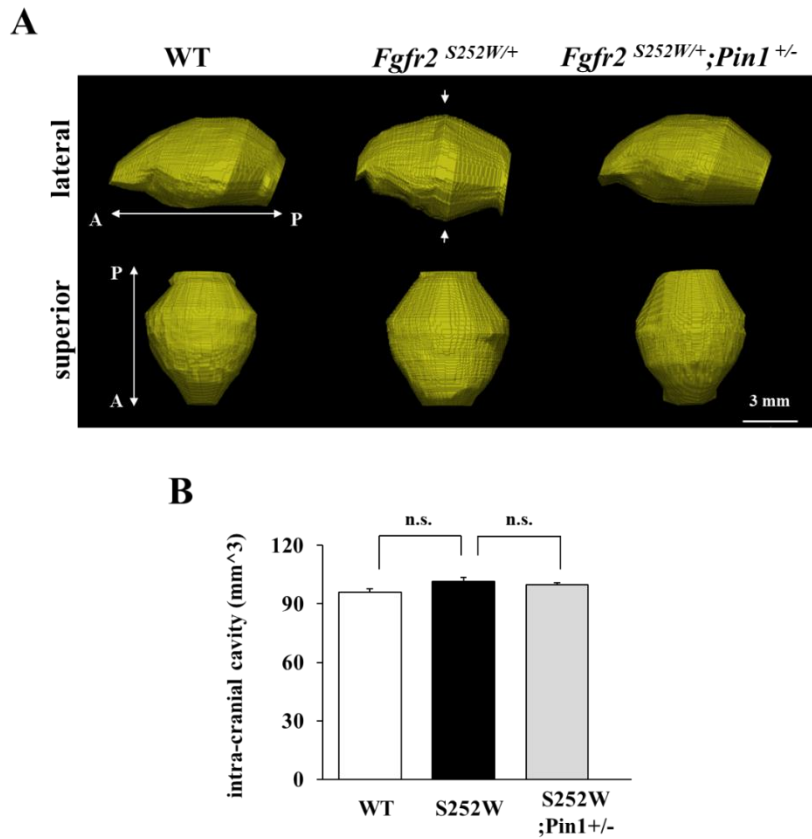


Figure 1–15. Endocranial shape changes in *Fgfr2*^{S252W/+} mice.

(A) 3D–reconstructed images of endocranial area. Endocranial shape of *Fgfr2*^{S252W/+} showed A–P dimensional shortening and dorsal–ventral dimensional expansion (white arrows). (B) The volume of 3D–reconstructed endocranial area was measured. (n.s., no significant)

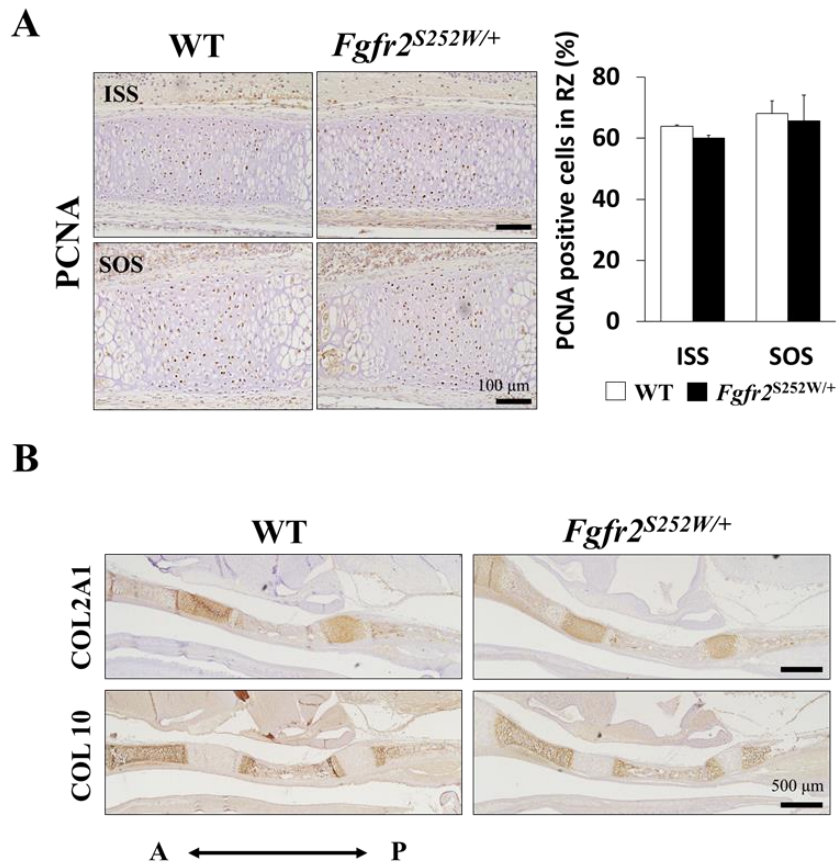


Figure 1–16. Synchondrosis growth in the cranial base was not impaired in *Fgfr2*^{S252W/+} at P0 stage

(A) PCNA was stained on synchondrosis of WT and *Fgfr2*^{S252W/+} mice. PCNA positive cells in resting zone of inter–sphenoid synchondrosis (ISS) and sphenoid–occipital synchondrosis (SOS) were counted from three different individuals (Image J, $p > 0.1$, Student t–test). (B) Collagen type II and collagen type X were detected by immunohistochemistry on cranial base of WT and *Fgfr2*^{S252W/+} mice.

A correlation of shape deformations between the face and the cranial base in *Fgfr2*^{S252W/+} mice

Two-block PLS analysis was performed to identify the covariation between the different modules of the skull; cranium, face and cranial base as assigned in Table 1-1. Strong correlation was found between the face and the cranial base shape changes (RV = 0.7705, $p \leq 0.0001$) (Figure 1-13A). Relatively small covariance was found in the other two analyses related to cranium in midface abnormalities (Figure 1-13B and C). Especially, shape variance of *Fgfr2*^{S252W/+} occupied the PLS1 positive end with high correlation between each component is mainly driven by associated changes in shortened, raised and widened face and retro-flexed cranial base (Figure 1-13D).

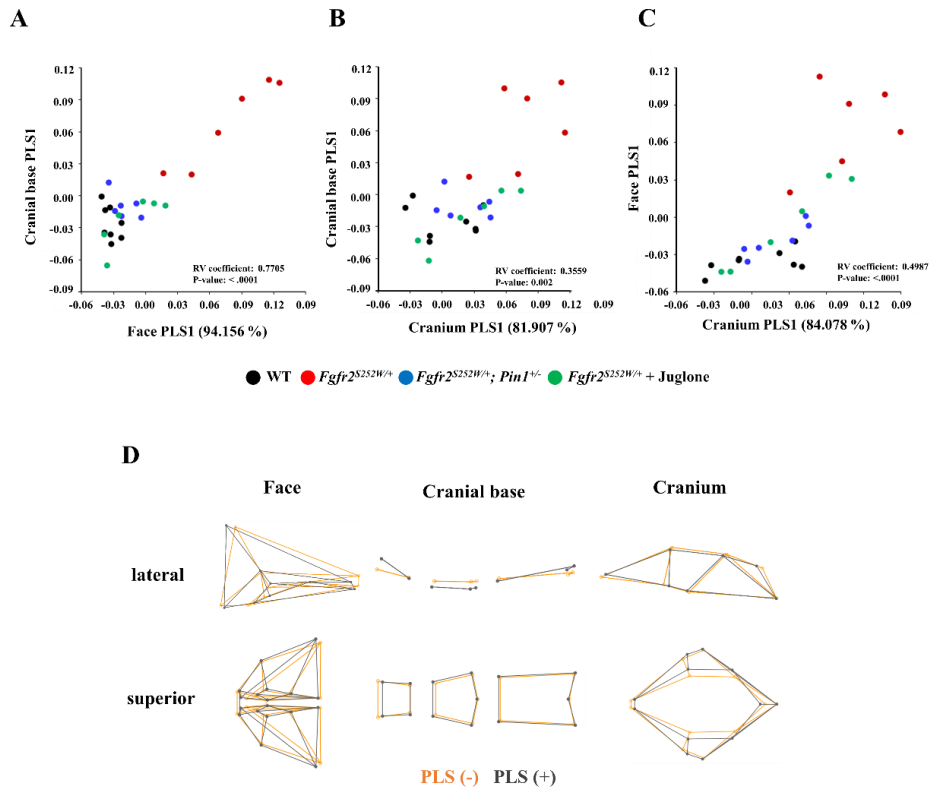


Figure 1–17. A correlation of shape deformations between the face and the cranial base in *Fgfr2^{S252W/+}* mice

(A) Associated face and cranial base shape changes corresponding to the first pair of PLS1 axes (94.156 % of total squared covariance) between four groups. RV coefficient and P–value between two blocks were represented in the plot graph. (B) PLS analysis between cranium and cranial base module along the PLS1 (81.907 % of total squared covariance). (C) PLS analysis between cranium and face module along the PLS1 (84.078 % of total squared covariance). (D)

Wireframe images represent the pattern of shape changes of each module along the negative PLS1 (orange line) or positive PLS1 axis (grey line). Landmarks corresponding to each subset are categorized on Table 1–1. Statistical significance test for PLS analysis was computed via permutation tests against the null hypothesis of independence with 10,000 rounds of number of randomization.

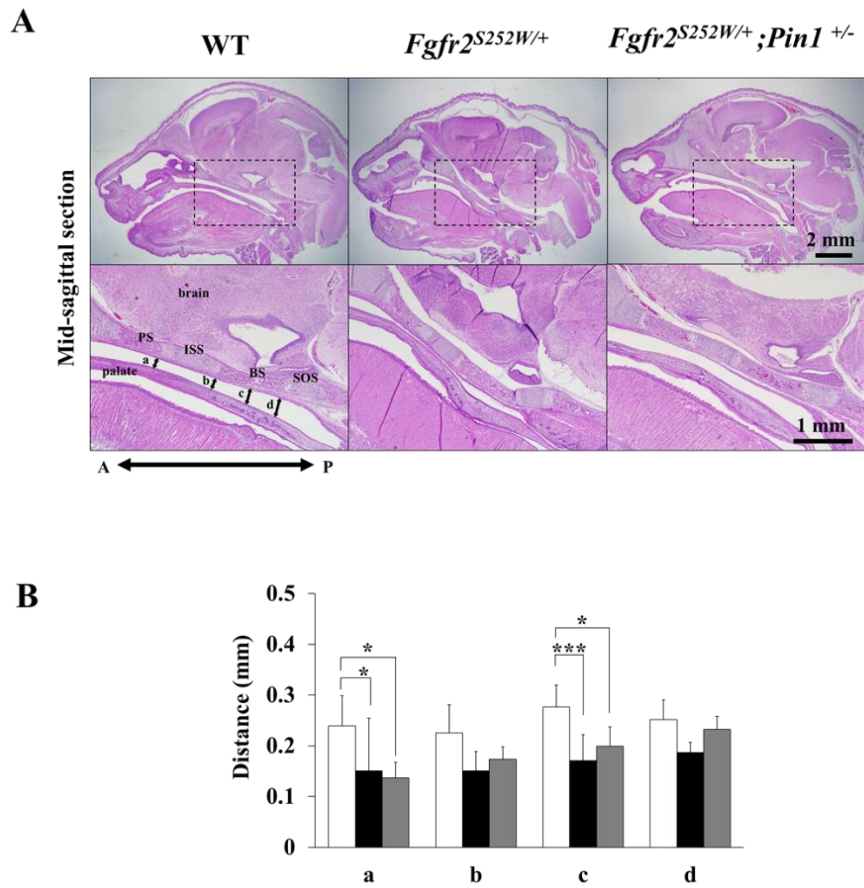


Figure 1–18. Narrowed and irregular airway due to retroflexed cranial base was attenuated by genetic *Pin1* haplodeletion.

(A) H&E staining on the mid-sagittal section of the skull showed an abrupt bending at the cranial base that causes decreases airway width from the nose to oropharynx in *Fgfr2*^{S252W/+} mice. However, *Pin1* haplodeletion caused the airway to return to WT morphology. The lower lane shows higher magnification of the boxed area in the upper lane. Lowercase letters (a, b, c, and d) indicate the distance between

each point on cranial base (a, caudal, ventral–most point of presphenoid bone; b, c, and d, rostral, mid, and caudal, ventral–most point of basisphenoid bone, respectively) to the closest point on the palate below. **(B)** Nasopharynx width marked as a–d was measured using ImageJ software. n=7 for WT, n=6 for *Fgfr2*^{S252W/+} and n=4 for *Fgfr2*^{S252W/+; Pin1}^{+/-}. (* $p \leq 0.05$, ** $p \leq 0.01$, *** $p \leq 0.001$).

Discussion

Among many clinical issues of Apert syndrome, along the coronal suture fusion, midface hypoplasia tends to be the most challenging part of craniosynostosis patient management (Cunningham et al. 2007). However, few studies have focused on molecular targets or non–surgical approaches for the recovery of midface anomalies. In our previous study, we have clearly demonstrated the rescue of coronal suture fusion by PIN1 inhibition as well as its molecular mechanism (Shin et al. 2018). Beyond cranial sutures, midface abnormalities come from more complicate interactions of various types of cells and tissues. In this study, we have shown detailed analyses of the structural changes of craniofacial skeletons as well as the recovery of midface hypoplasia by PIN1 inhibition.

We confirmed that the premature closure of facial sutures is the main contributing element of *Fgfr2*^{S252W/+}-induced midface hypoplasia. Abnormal flexion at the cranial base also contributes toward midface hypoplasia. It is well known that the facial region, the anterior part of the calvarium, and the rostral part of the sphenoid bones originate from the neural crest, which have a much higher osteogenic potential than the posterior part of the cranium, mesodermal origin (Li et al. 2010; Xu et al. 2007). Among many morphogens involved in craniofacial development, Wnt1 is one of the main differences between neural crest and mesoderm-origin cells (Yoshida et al. 2008). Moreover, canonical Wnt/ β -catenin-dependent FGF signaling is crucial for the outgrowth of nasal and maxillary processes in the development of the upper jaw (Jin et al. 2012). These studies might explain why more significant defects are found in the anterior parts of the cranium and face.

The premature suture closure is mainly found in transverse sutures in *Fgfr2*^{S252W/+} mice (Martinez-Abadias et al. 2013; Motch Perrine et al. 2014). Likewise, FGFR-mediated syndromic craniosynostosis such as Apert and Crouzon syndrome is well studied as the main cause of coronal suture defects (Johnson and Wilkie 2011). These studies suggest that FGF signaling might contain certain key genes

for determining transverse suture growth and anterior–posterior growth of the head.

Despite observing protruded mandibles in *Fgfr2*^{S252W/+} mice, we also observed decreases in the mandibular body length and gonial angle. As reported in human cases, the mandibular shape among Apert syndrome patients can be determined by facial growth and angulation of the cranial base (Kasai et al. 1995; Wink et al. 2013). Alteration of mandibular growth in this mouse model also could be interpreted as an adaptive mechanism to accommodate midface hypoplasia.

The downward flexion at the cranial base in *Fgfr2*^{S252W/+} mice is probably caused by an increase in intracranial pressure generated by brain growth (Connolly et al. 2004; Kreiborg et al. 1993). We also found the close relationship between cranial base structure and skull growth. Consequently, upper airway obstruction is frequently observed among Apert syndrome patients due to midface hypoplasia (Ahmed et al. 2008). It may cause bad breathing habits, subsequently resulting in facial deformities (Basheer et al. 2014). In the *Fgfr2*^{S252W/+} mice, the abruptly elevated premaxilla caused a distortion in the anterior nasal structure with high palatal vault and narrowed airway, which may have caused serious respiratory

problems. Interestingly, a recent study has shown decreased nasal airway volume as elements for midface abnormalities in the same mouse model (Holmes et al. 2018). These results suggest that multiple approaches managing intrinsic and extrinsic elements should be considered for breathing issues of Apert syndrome.

Despite dramatic shape changes, we could not find significant defect of synchondrosis or cranial base growth at P0 stage. Considering the low expression level of FGFR2 on the cartilage (Eswarakumar et al. 2002; Lazarus et al. 2007), direct effect of *Fgfr2* S252W mutation on cartilage development might be mild (Chen et al. 2003; Yu et al. 2003). There is also possibility that there should be decreased proliferation when the condensations are forming (Shimizu et al. 2007), and it could be varied with developmental stages (Holmes et al. 2018). Based on our PLS analyses, we found the facial shape deformations could be the major contributor to the cranial base abnormalities rather than cranial base growth itself. Although dramatic distortion of cranium was not presented at P0 stage, raised intracranial pressure and spatial restriction due to the nasal and coronal suture fusion should also affect cranial base growth (Connolly et al. 2004). These results suggest that the facial and cranial suture closure cause midface hypoplasia in *Fgfr2*^{S252W/+} mice in the direct

and indirect manner. Therefore, rescue of abnormal suture growth by modulating PIN1 would successfully recover *Fgfr2*^{S252W/+}-induced midface hypoplasia and overall craniofacial anomalies.

Because *Fgfr2*^{S252W/+} mice already demonstrate craniosynostosis at P0 stage, Juglone was applied *in utero* before craniofacial suture fusion. Juglone has a molecular weight of 174.2 Da with a lipid-soluble character, which could possibly pass the placental barrier (Griffiths and Campbell 2015). We also have observed a dose-dependent effect on littermates (Shin et al. 2018). Because Apert syndrome patients require several rounds of corrective surgery, it would be useful if Juglone treatment could delay or prevent further surgical intervention. Although inhibition of PIN1 in this study significantly improved the *Fgfr2*^{S252W/+} skull phenotypes and appear to be moving towards the WT in appearance in some aspects, there are distinct differences and high variations compared to the WT skull. These limitations indicate that more effective drug concentration determination or lower-dose combination therapy targeting PIN1 must be needed for further clinical application.

In our Apert syndrome mice model, we did not find syndactyly, a key feature of Apert syndrome in humans as other studies also mentioned

(Wang et al. 2005). The absence of this feature could be explained with the possibility that S252W mutation on FGFR2 causes less severe digital syndactyly in humans when compared with P253R mutation on FGFR2 (Lajeunie et al. 1999; Passos-Bueno et al. 1998). Likewise, mice with FGFR2-P253R mutation showed digital abnormalities (Yin et al. 2008). Moreover, species-specific differences or alternative splicing levels of FGFR2 could affect to the absence of syndactyly in mice model (Oldridge et al. 1999; Wang et al. 2005).

In the present study, we have conducted detailed and careful quantitative analyses of changes in the midface in the mouse model of Apert syndrome. Premature obliteration of the facial sutures and the flexion of the cranial base were suggested as contributing factors causing midface hypoplasia, which were significantly alleviated by PIN1 inhibition. Our data strongly demonstrates that targeting PIN1 as a therapeutic strategy for the prevention and treatment of craniofacial abnormalities in Apert syndrome.

IV. Part 2

Role of septal cartilage on midface hypoplasia of Apert syndrome

Abstract

Midface hypoplasia is a major manifestation of Apert syndrome. However, the tissue component responsible for midface hypoplasia has not been elucidated. We studied mice with a chondrocyte-specific *Fgfr2*^{S252W} mutation (*Col2a1-cre; Fgfr2*^{S252W/+}; referred to hereafter as *Col2-SW*) to investigate the effect of cartilaginous components in midface hypoplasia of Apert syndrome. In *Col2-SW* mice, skull shape was normal at birth, but hypoplastic phenotypes became evident with age. General dimensional changes of *Col2-SW* mice were comparable with those of mice with mutations in *EIIa-cre; Fgfr2*^{S252W/+}, a classic model of Apert syndrome in mice. *Col2-SW* mice showed some unique facial phenotypes, such as elevated nasion, abnormal fusion of the suture between the premaxilla and the vomer, and decreased ethmoid bone volume, which are related to the

development of the nasal septal cartilage. Morphological and histological examination revealed that the presence of increased septum chondrocyte hypertrophy and abnormal thickening of nasal septum is causally related to midface deformities in nasal septum-associated structures. Our results suggest that careful examination and surgical correction of the nasal septal cartilage can improve the prognosis in the surgical treatment of midface hypoplasia and respiratory problems in patients with Apert syndrome.

Introduction

Activating mutations of the fibroblast growth factor receptor 2 (*FGFR2*) gene are well-known to cause syndromic craniosynostosis, including Apert, Crouzon, and Pfeiffer syndromes. (Cunningham et al. 2007). In the case of Apert syndrome, mostly Ser252Trp or Pro253Arg mutations cause loss of ligand-receptor specificity and hyperactivation of downstream signaling (Yu et al. 2000). Syndromic craniosynostosis is often characterized by elevated intracranial pressure and breathing difficulties, which result mainly from midface hypoplasia (Forte et al. 2019; Nout et al. 2012). Surgical maxillary advancement should be conducted to reduce respiratory distress and

intracranial hypertension (Heggie et al. 2013). However, because of the unpredictable growth pattern of the midface, a surgical correction might be repeated later in life with multidisciplinary approaches (Mathijssen 2015).

Nasal septum development is essential in the midface; it is responsible for sagittal and vertical maxillary growth (Grymer and Bosch 1997; Hall and Precious 2013). Several patients with craniosynostosis have a narrow nose, septum deviation, and associated breathing issues (Mathijssen 2015). Additionally, since the nasal septal cartilage articulates with various facial bones (Posnick 2014) and has various roles as a growth center in the midface (Howe et al. 2004), an understanding of the intrinsic growth potential of the nasal septal cartilage is therefore critical for surgical correction of craniofacial defects.

We previously reported that premature obliteration of the facial suture was the main contributor to the development of midface hypoplasia and skull anomalies in a mouse model of Apert syndrome (Kim et al. 2020a). However, the intrinsic growth of facial bony or cartilaginous components beyond the craniofacial suture closure is still poorly understood. In this study, we carefully observed mice with

the chondrocyte-specific *Fgfr2*^{S252W} mutation to examine the growth of facial cartilaginous tissues and its effect on midface hypoplasia.

Materials and methods

Generation of tissue-specific mutant mice

A mouse carrying ploxPneo cassette, which blocks expression of the mutant *Fgfr2* allele (*Fgfr2*^{neoS252W/+}) (Shukla et al. 2007) was bred with different types of Cre recombinase-expressing mice, *EIIa-cre* (B6.FVB-TgN [EIIa-cre] C3739Lm, 003724; Jackson Laboratory), *Col2a1-cre* (Ovchinnikov et al. 2000) and *Colla1(2.3kb)-cre* (Lim et al. 2016) mouse. *Col2a1-cre* and *Colla1-cre* transgenic mice were kindly provided by Dr. Je-Young Choi (Kyungpook National University, Daegu, Korea). Homozygotic Cre transgenic mice were used in this study. Pups carrying *Fgfr2*^{S252W} mutation were examined at neonate (P0), one-week (P7) and three-weeks old (P21). All mice were maintained under specific pathogen-free conditions. All experiments were performed in accordance with the policies of the Institutional Animal Care and Use Committee and Special Committee on Animal Welfare of Seoul National University (Seoul, Korea).

Micro-CT scanning and landmark placing

Mice were euthanized, and dissected head was fixed with 4% of paraformaldehyde. Micro-CT scans were acquired by using skyscan1272 (Bruker, North Billerica, MA) with 10 or 20 $\mu\text{m}/\text{pixel}$ of resolution. The samples stained with Iodine-based contrast-enhancing agent, Lugol's triiodine solution (L6146, Sigma Aldrich, St. Louis, MO) (Gignac et al. 2016) for 48 hours were scanned with 10 $\mu\text{m}/\text{pixel}$ of resolution for nasal septal cartilage examination. Septal cartilage area was manually selected at the coronal view of slice images and reconstructed by using CT Analyzer software (Bruker, North Billerica, MA). 23 landmarks on the craniofacial bones (Figure 2-1 and Table 2-1) (Kim et al. 2020a) and 15 landmarks on the nasal septal cartilage (Figure 2-2 and Table 2-2) were recorded by using Landmark Editor 3.0v (IDAV, University of California, Davis, CA).

Shape analyses and Statistics

Linear and volumetric measurements of the 3D-reconstructed skull, vomer, nasal septal cartilage and perpendicular plate of ethmoid bone were performed by using the CT Analyzer (Bruker, North Billerica,

MA) and TRI 3D-BON (RATOC System Engineering Co., Tokyo, Japan). Landmark coordinates were processed into the Procrustes superimposition to uniformly scale the objects, and utilized for principal component analysis (PCA) and discriminant function analysis (DFA) by using MorphoJ v1.06d (Klingenberg 2011) as previously described (Kim et al. 2020a). To analyze the shape distribution among groups, Procrustes ANOVA was performed via permutation test against the null hypothesis of independence with 1000 rounds of number of randomization. Septal deviation was measured on the coronal plane of nasal cavity by using imageJ software (NIH, Bethesda, MD). Values are presented as the mean \pm SD and statistical analysis was performed with one-way ANOVA, followed by Tukey or Bonferroni multiple comparison test with Prism 8.4.3 (GraphPad). $P \leq 0.0332$ was considered significant.

Histological Analysis

The specimens were processed as previously described (Kim et al. 2020a). Paraffinized dissected head of mice was serially sectioned to 5 μm -thick on the sagittal or coronal plane with rotary microtome (RM2145, Leica, Wetzlar, Germany). Slides including the premaxilla,

the vomer and the palatine process were selected on the sagittal plane. Slides including the septal cartilage and the vomer body were selected on the coronal plane. Slides were stained with alcian blue, hematoxylin and eosin. For quantify cellular number and size on the septal cartilage, each chondrocyte was selected manually by using the osteomeasure software (Osteometrics, Decatur, GA) and calculated with imageJ software (NIH, Bethesda, MD). For immunohistochemistry, rehydrated slides were treated with citrate buffer (pH 6.0) for 10 min at 90 ° C or proteinase K solution for 30 seconds at 37 ° C for antigen retrieval. SOX9 (sc-20095, santa cruz, Dallas, TX), RUNX2 (D130-3, MBL international Co., Woburn, MA) and type X collagen (234196, Millipore, Burlington, MA) were detected. Stained cells were counted by using imageJ software (NIH, Bethesda, MD).

RNA Isolation from Nasal Septal Cartilage and Gene Expression Analysis

Nasal septal cartilage was carefully isolated from P0 and P7 mice after euthanization. Soft tissues around septal cartilages were cleaned with scalpel and directly moved to the QIAzol lysis reagent

(79369; Qiagen, Hilden, Germany). Isolated RNA was synthesized into cDNA (RR036A; Takara, Kyoto, Japan), and quantitative real-time PCR was performed (RR420A; Takara, Kyoto, Japan). Details for the primers were described on Table 1. Values are presented as the mean \pm SD and the significance was calculated by Student's *t* test. $P \leq 0.05$ was considered significant.

Staining of trachea

Isolated trachea from P21 mice was stained with alcian blue solution (ANC500, scytek, UT) for overnight. The trachea was observed with stereo microscope (Stemi 305, Carl Zeiss, Oberkochen, Germany). The images of trachea were taken by AxioCam 105 camera and AxioVision software (Carl Zeiss).

Results

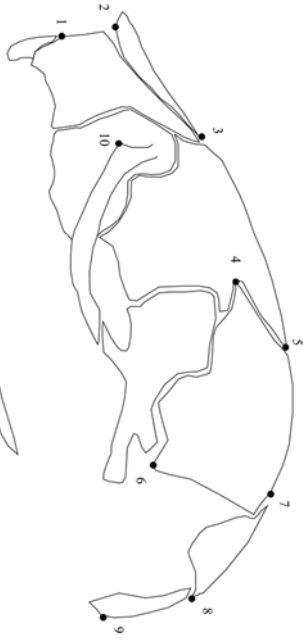
Chondrocyte-specific *Fgfr2*^{S252W} shows a progressive midface hypoplasia in the absence of premature craniofacial suture closure

Micro-CT images of Apert syndrome model (*EIIa-cre; Fgfr2*^{S252W/+}, referred to hereafter as “*EIIa-SW*”) mouse at P0 showed early fusion of coronal, naso-frontal and premaxillo-maxillary sutures (Figure 2-3A). Premaxillo-maxillary suture, normally patent at P7, is obliterated on *EIIa-SW*. At P21, *EIIa-SW* showed dramatically shortened skull and the nasion severely sunken nasion and distorted nose. Chondrocyte-specific *Fgfr2*^{S252W} mice (*Col2a1-cre; Fgfr2*^{S252W/+}; referred to as “*Col2-SW*” hereafter) did not show premature fusion of coronal, naso-frontal suture at P0, premaxillo-maxilla suture until P7 (Figure 2-3B and Table 2-4). However, despite normal skull shape at P0, *Col2-SW* showed decrease in antero-posterior growth of skull comparable to that of *EIIa-SW* (Figure 2-3B). As mature osteoblast-specific *Fgfr2*^{S252W} mice (*Col1a1(2.3kb)-cre; Fgfr2*^{S252W/+}; referred to as “*Col1-SW*” hereafter) showed normal craniofacial suture and skull growth (Figure 2-13A~C) and no lethality (Figure 2-5), we did not focus on *Col1-SW* in this study. Although *Col2-SW* presented improved

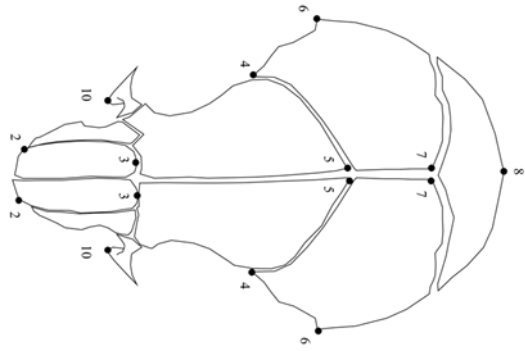
survival rate compare to *EIIa-SW*, they still showed lower genotypic ratio than expected ratio (Figure 2-5). Although skull shortening of *EIIa-SW* was noticeable from P0 stage, *Col2-SW* showed progressive decrease of skull growth (Figure 2-6B). The length of skull components, cranium, cranial base and face showed similar growth pattern to the whole skull (Figure 2-6C). The relative width of the face and the cranium were increased in the *EIIa-SW* considering reduced their length, probably due to the increased intra-facial and -cranial pressure (Figure 2-6D). Meanwhile, *Col2-SW* showed increased facial width, despite no premature facial suture closure. Facial height was increased as the nasion has been elevated in *Col2-SW* (Figure 2-6E). Three-dimensional morphometric analysis based on the landmarks (Figure 2-1 and Table 2-1) at P0 demonstrated distinct skull shape variance of *EIIa-SW* (Figure 2-7A). Widened cranium and retroflexed cranial base was noticeable on *EIIa-SW* (Figure 2-7B). *Col2-SW* mice showed similar skull shape to WT at P0. At P7, the mutant mice presented more distinct skull shape variance (Figure 2-8A). Shortened and widened skull and retroflexed cranial base became more evident compare to P0 stage of *EIIa-SW*. *Col2-SW* skull shape became distinct from WT and *EIIa-SW*, especially with elevated nasion (Figure 2-8B). The

craniofacial shape variance of each group was more clearly distinguished at P21 (Figure 2-9 and 2-10). The skull shape variances shown at P7 became severer. P21 mice demonstrated shortened face, sunken nasion, expanded cranium and flexed cranial base of *EIIa-SW* (Figure 2-9A, C, E). *Col2-SW* mice also showed shortening of anterior face, but they showed normal cranial base shape and cranial width. Especially, the nasion was notably elevated (Figure 2-9E and 2-11). These results suggest that *Col2-SW* showed relatively progressive craniofacial deformities in the absence of premature craniofacial suture closure, and thus, altered growth of facial cartilaginous tissue might be important on these anomalies.

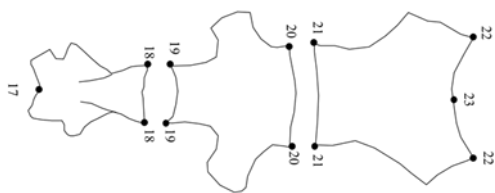
cranium (lateral view)



cranium (superior view)



cranial base (superior view)



anterior face (inferior view)

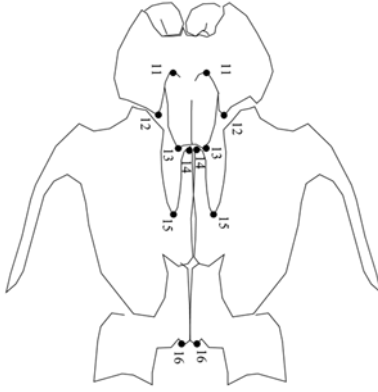


Figure 2–1. Landmarks on the craniofacial bones used for morphometric analyses

Three–dimensional 23 landmarks were assigned on the cranium, the face and the cranial base. Detail description of landmarks are in Table 2–1.

Table 2–1. Landmark description used on the craniofacial shape analyses

Landmark	Description	module
1	Point A, anterior–most point of alveolus of upper incisor (left and right)	face
2	Most antero–lateral point of corner of the nasal bone (left and right)	face
3	Nasion, caudal point of nasal bone (left and right)	face, cranium
4	Most superior point on the squamous temporal, intersection of the coronal suture (left and right)	cranium
5	Most medial intersection of the frontal and parietal bones, taken on the frontal (left and	cranium

	right)	
6	Most postero-inferior point on the parietal bone (left and right)	cranium
7	Most postero-medial point on the parietal bone (left and right)	cranium
8	Caudal-most point of interparietal bone at mid-sagittal plane	cranium
9	Caudal-most point of occipital bone at mid-sagittal plane	cranium
10	Anterior notch on zygomatic process (left and right)	face
11	Most anterior point of the anterior palatine foramen (left and right)	face
12	Most infero-lateral point of the premaxillary-maxillary suture, taken on premaxilla (left and right)	face
13	Caudal-most point of premaxilla bone at mid-sagittal plane (left and right)	face
14	Most anterior point of palatine process of maxilla (left and right)	face
15	Most posterior point of the anterior palatine foramen (left and right)	face
16	Caudal-most point of palatine bone at mid-sagittal plane (left and right)	face
17	Rostral, dorsal-most point of presphenoid bone at mid-sagittal plane	cranial base
18	Most postero-lateral, dorsal point of corner of	cranial

	the presphenoid bone (left and right)	base
19	Most antero-lateral, dorsal point of corner of the basisphenoid bone (left and right)	cranial base
20	Most postero-lateral, dorsal point of corner of the basisphenoid bone (left and right)	cranial base
21	Most antero-lateral, dorsal point of corner of the basioccipital bone (left and right)	cranial base
22	Most postero-lateral, dorsal point of corner the basioccipital bone (left and right)	cranial base
23	Basion, caudal, dorsal-most point of basi-occipital bone at mid-sagittal plane	cranial base

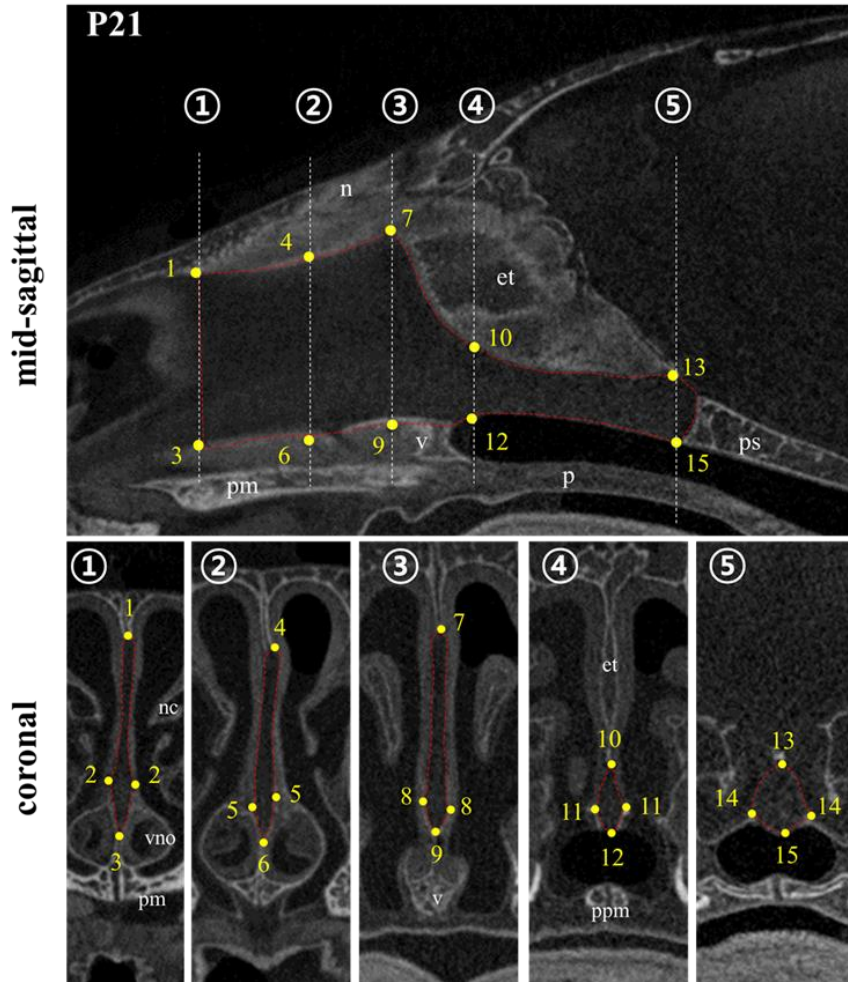


Figure 2–2. Landmarks on the nasal septal cartilage for 3D shape analysis. Red dotted area presents manually selected septal cartilage region. Descriptions for landmarks are on Appendix Table 6. Plane ① was selected where the incisive foramen ends and two premaxilla plates meet. The position of all specimens was equally aligned considering the shape and

size of premaxilla bone, nasal concha, incisor root and vomeronasal organ. n, nasal bone; et, ethmoid bone; pm, premaxilla bone; v, vomer; p, palate; nc, nasal concha; vno, vomeronasal organ; ppm, process of palatine bone of maxilla. Plane ②, ③, ④ and ⑤ are crossing the landmarks 4, 7, 10 and 13, respectively.

Table 2–2. Landmark description used on the nasal septal cartilage shape analysis

Landmark	Description
1	Most superior point of septum at the plane ①*
2	Most lateral point of septum at the plane ①
3	Most inferior point of septum at the plane ①
4	Most concave point of septum adjacent to the nasal bone. The plane ② is parallel to plane ① crossing landmark 4.
5	Most lateral point of septum at the plane ②
6	Most inferior point of septum at the plane ②
7	The highest point of septum at the nasion. The plane ③ is parallel to plane ① crossing landmark 7.

8	Most lateral point of septum at the plane ③
9	Most inferior point of septum at the plane ③
10	Most concave point of septum adjacent to the perpendicular plate of ethmoid bone. The plane ④ is parallel to plane ① crossing landmark 10.
11	Most lateral point of septum at the plane ④
12	Most inferior point of septum at the plane ④
13	Most superior point of septum at the boundary of presphenoid bone. The plane ⑤ is parallel to plane ① crossing landmark 13.
14	Most lateral point of septum at the plane ⑤
15	Most inferior point of septum at the plane ⑤

Table 2–3. Primers used for quantitative real–time PCR

gene (mouse)	forward (5' → 3')	reverse (3' → 5')
<i>Gapdh</i>	CATGTTCCAGTATGACTCCAC TC	GGCCTCACCCCATTTGATGT
<i>Type X collagen</i>	TTCTGCTGCTAATGTTCTTGACC	GGGATGAAGTATTGTGTCTTGG G
<i>Osteopontin</i>	ATCTCACCA TTC GGA TGA GTC T	TCAGTCCATAAGCCAAGCTATCA
<i>Mmp13</i>	CTTCTTCTTGTGAGCTGGACTC	CTGTGGAGGTCACTGTAGACT
<i>Ki–67</i>	CTG CCT GCG AAG AGA GCA TC	AGC TCC ACT TCG CCT TTT GG
<i>Fgf2</i>	GCGACCCACACGTCAAATA	TCCCTTGATAGACACAACCTCCTC
<i>Fgf18</i>	GGACATGTGCAGGCTGGGCTA	GTAGAATCCCGTCTCCTTGCCCT T
<i>Bmp2</i>	GGGACCCGCTGTCTTCTAGT	TCAACTCAAATTCGCTGAGGAC
<i>Bmp4</i>	TTCCTGGTAACCGAATGCTGA	CCTGAATCTCGGCGACTTTTT
<i>Ihh</i>	TGGA CTCATTGCCTCCAGA	CAAAGGCTCAGGAGGCTGGA
<i>Wnt3a</i>	CTCCTCTCGGATACCTCTTAGTG	GCATGATCTCCACGTAGTTCCTG
<i>Vegf</i>	GCCAGCACATAGAGACAATGAGC	ATCCGCATGATCTGCATGATGG
<i>Tgf–beta1</i>	CTCCCGTGGCTTCTAGTGC	GCCTTAGTTTGGACAGGATCTG
<i>Gremlin1</i>	ACAGCGAAGAACCTGAGGAC	CAGCTGTTGGCAGTAGGGTC

<i>Ecm-1</i>	ATAAAGACCCACCCCACTC	AGCAGCGGATGGTCATATTC
<i>Noggin</i>	TGTACGCGTGGAATGACCTA	GTGAGGTGCACAGACTTGGA

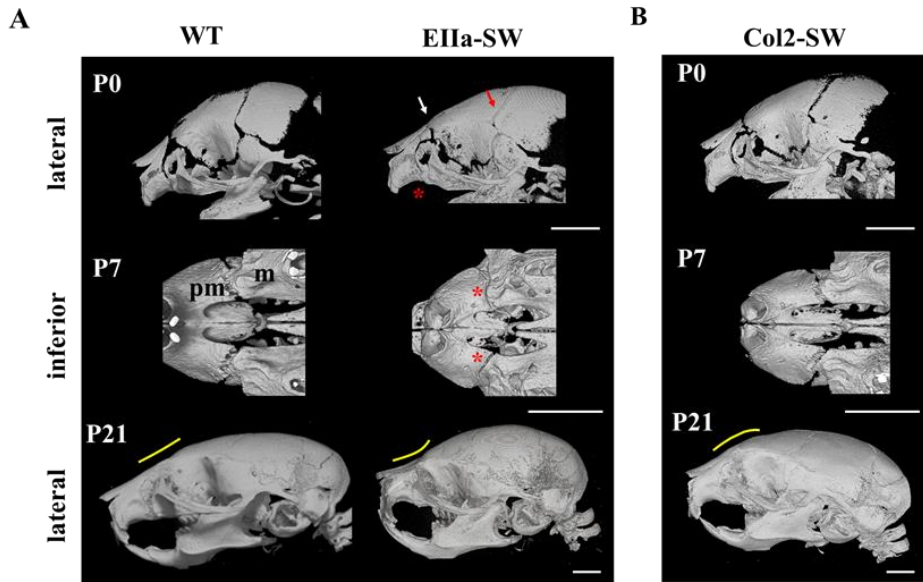


Figure 2–3. Cranial anomalies on *EIIa-SW* and *Col2-SW*. (A) Micro CT images of skull of Apert syndrome mouse model at postnatal day 0, 7, and 21 (P0, P7 and P21). White arrow and red arrow on *EIIa-SW* indicates the fusion on naso-frontal and coronal suture, respectively. Red asterisk indicates the fusion of premaxilla-maxillary suture at P0 and P7. pm, premaxilla; m, maxilla. Yellow line represents the curvature of nasion. Scale bar: 2 mm (B) Micro-CT images of *Col2-SW* at P0, P7 and P21. Yellow line indicates the curvature of nasion. Scale bar: 2 mm.

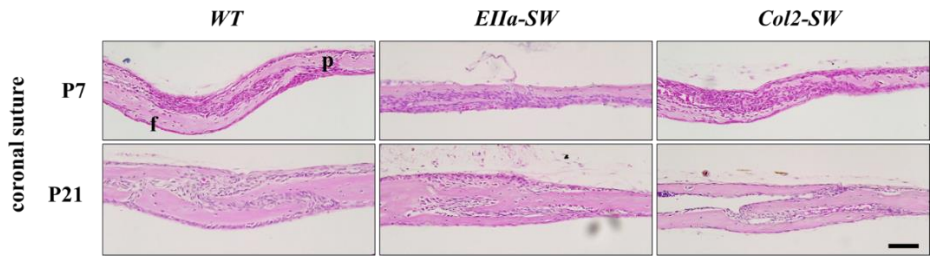


Figure 2–4. Histology of coronal suture of *Fgfr2*^{S252W/+} mutant mice. Hematoxylin and eosin staining of coronal suture at P7 and P21 stages. Frontal bone (f) and parietal bone (p) were fused on *EIIa-SW*, not on *Col2-SW*. Scale bar: 100 μ m

Table 2-4. Craniofacial suture fusion frequency at P0 and P7 stages

age	genotypes	craniofacial sutures		
		coronal	naso- frontal	premaxillo- maxilla
P0	<i>WT</i>	0/5	0/5	0/5
	<i>EIIa-SW</i>	5/5	3/5	1/5
	<i>Col2-SW</i>	0/5	0/5	0/5
P7	<i>WT</i>	0/5	0/5	0/5
	<i>EIIa-SW</i>	4/5	5/5	5/5
	<i>Col2-SW</i>	0/5	0/5	0/5

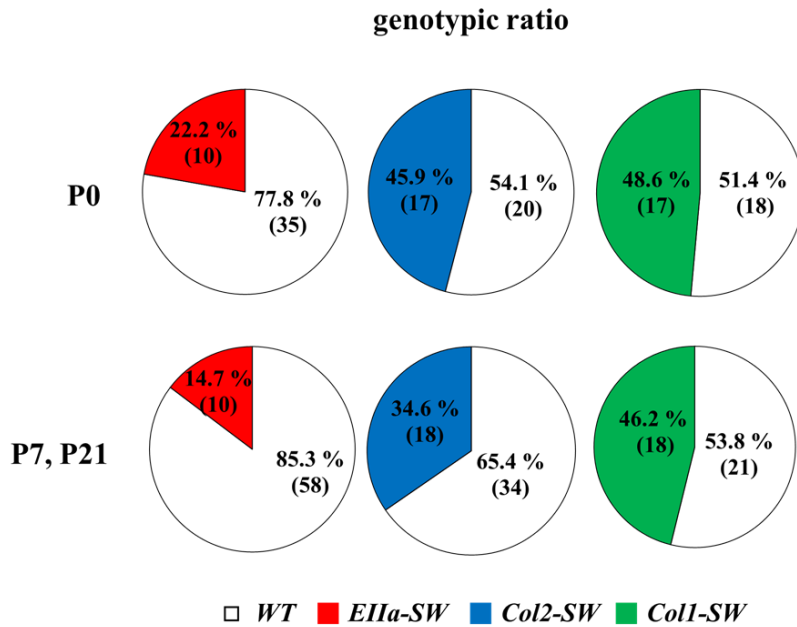


Figure 2–5. The ratio of each mouse genotype. The genotypes were checked at P0 (neonatal) or P7 and P21 (postnatal). The expected genotypic ratio of WT and *Fgfr2*^{S252W/+} is 1:1. *EIIa-SW* showed neonatal lethality, and only 14.7 % of mutant mice can survive after P7. *Col2-SW* showed normal birth rate, but postnatal lethality as they grow. *Col1-SW* did not show lethality.

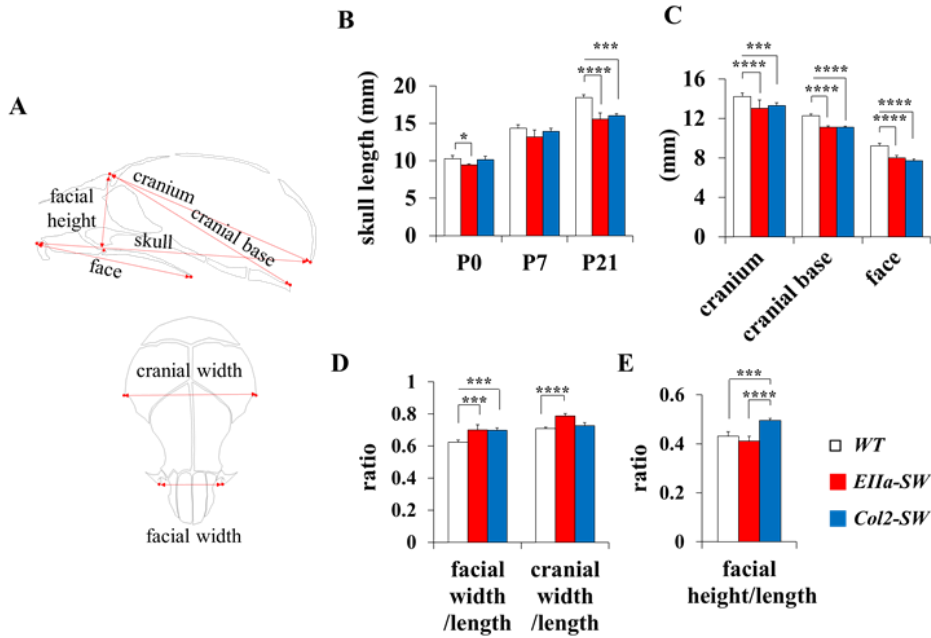


Figure 2–6. Linear measurements of craniofacial bones. (A) The depiction of linear measurements on the mid–sagittal and superior view. Details for landmarks are on Figure 2–1 and Table 2–1. (B) Total skull length of each group at P0, P7 and P21. (C) Linear measurements of the cranium, the cranial base and the face. (D) The relative facial and cranial width to the length. (E) The relative facial height to the length. Values are presented as mean \pm SD. * $p \leq 0.0332$, ** $p \leq 0.0021$, *** $p \leq 0.0002$, **** $p \leq 0.0001$ ($n=5$).

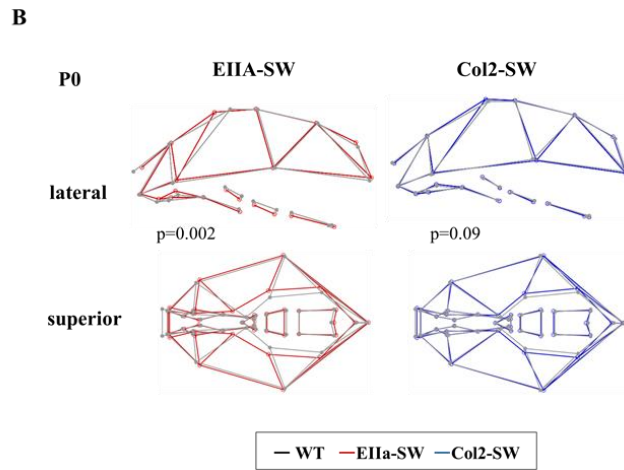
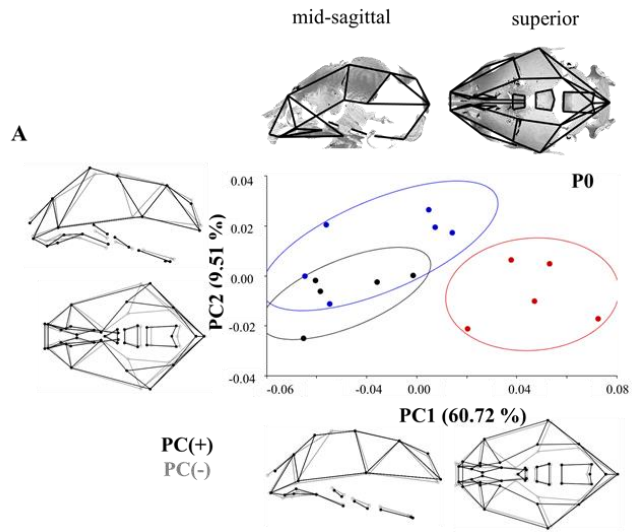


Figure 2–7. Morphometric analysis of skull at P0

(A) PCA analysis of the skull at P0. Upper lane indicates the landmarks on mid–sagittal and superior plane. The percentage of total variance for each PC was displayed on the axis of plot graph. Wireframe images indicate the shape variance along the PC axis. (B) Mean skull shape comparison between WT and mutant mice. P–values for permutation tests (1000 permutations) between two groups are showed below of the wireframe images ($n = 5$)

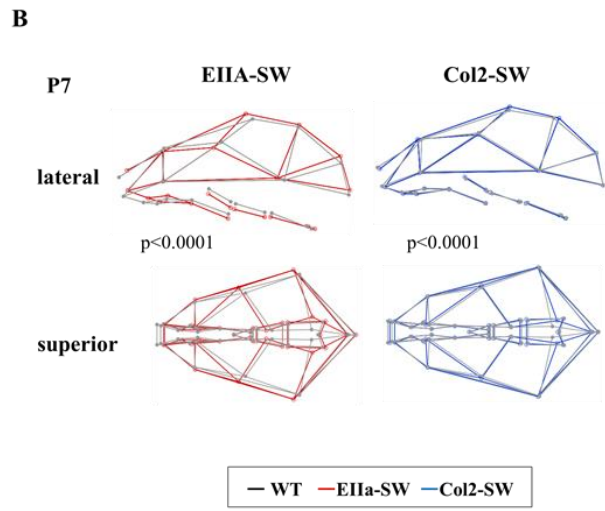
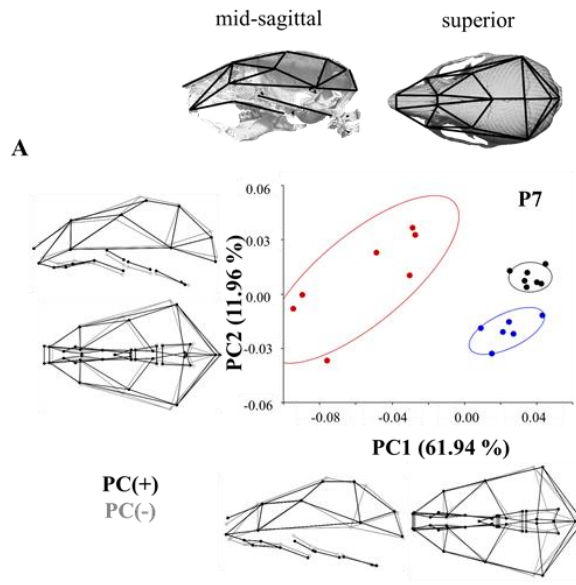


Figure 2–8. Morphometric analysis of skull at P7

(A) PCA analysis of the skull at P7. Upper lane indicates the landmarks on mid–sagittal and superior plane. The percentage of total variance for each PC was displayed on the axis of plot graph. Wireframe images indicate the shape variance along the PC axis. (B) Mean skull shape comparison between WT and mutant mice. P–values for permutation tests (1000 permutations) between two groups are showed below of the wireframe images ($n=5$)

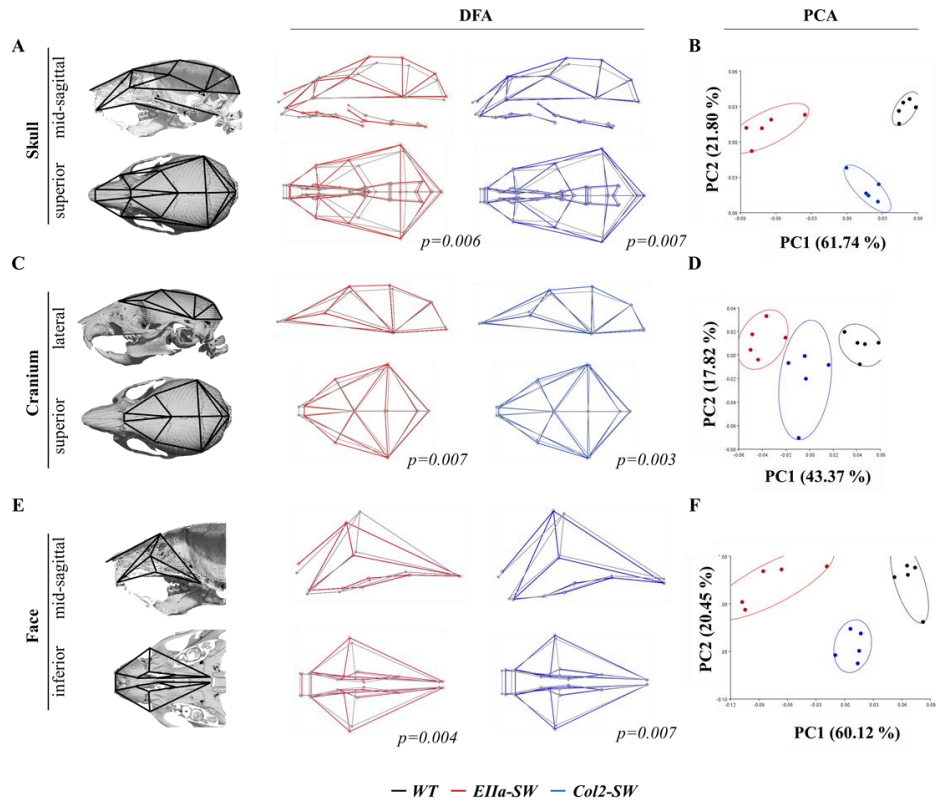


Figure 2–9. Morphometric analysis of whole skull, cranium and face.

Based on the craniofacial landmarks (Figure 2–1 and Table 2–1), 3D shape changes and patterns were analyzed at P21 stage. The mean shape of whole skull, the cranium and the facial bone is represented with wireframe images by discriminant function analyses (DFA) (**A**, **C** and **E**). P -values for permutation tests (1000 permutations) between two groups are showed below of the wireframe images. The shape variance of skull components was analyzed by PCA (**B**, **D** and **F**). ($n=5$)

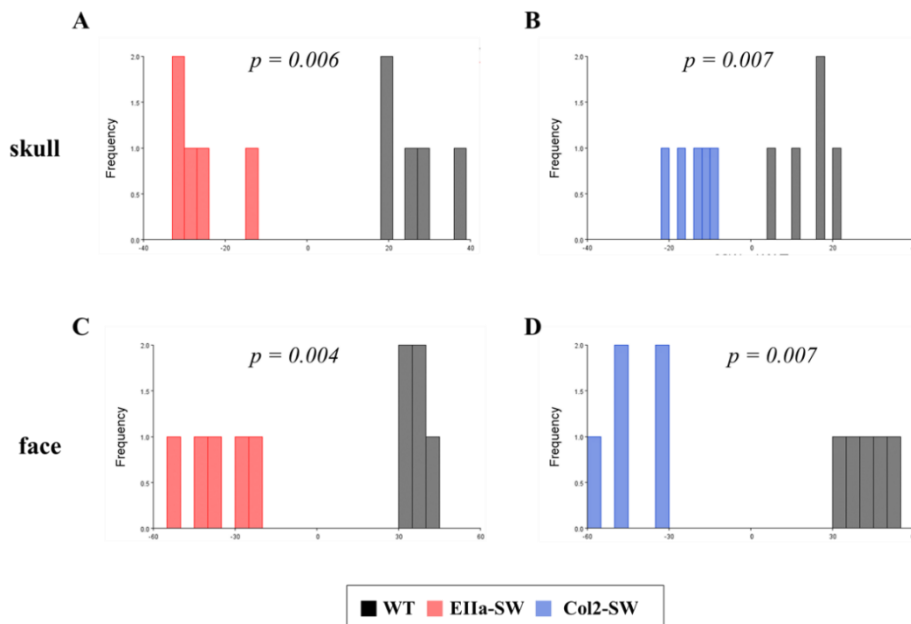


Figure 2–10. DFA for skull and facial shape variation (related to Figure 2–7A and 2–7E).

Cross-validation scores for comparison of (A) skull between WT and *EIIa-SW*, (B) skull between WT and *Col2-SW*, (C) face between WT and *EIIa-SW* and (D) face between WT and *Col2-SW*. ($n=5$)

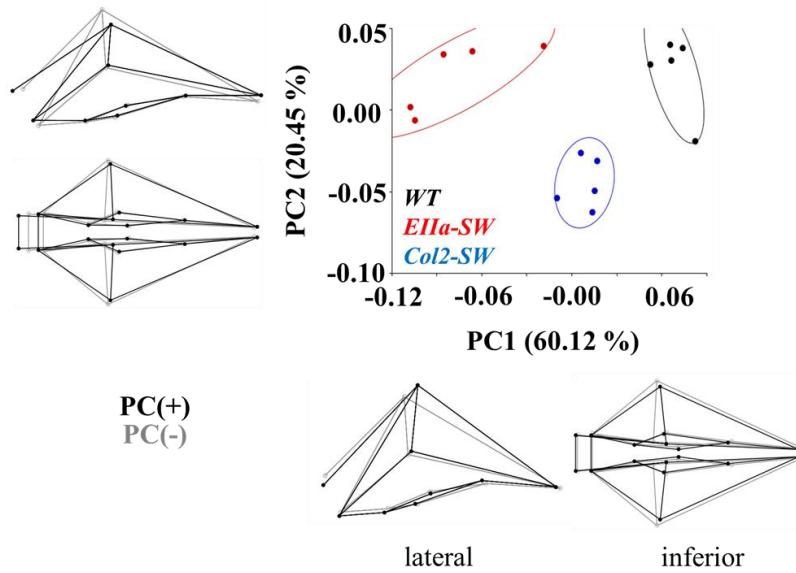


Figure 2–11. The facial shape variance of each group by PCA

The percentage of total variance for each principal component is displayed on the axis. The shape changes were represented with wireframe images by the axis along the negative PC (grey line) or positive PC axis (black line). ($n=5$)

Abnormal growth of facial bones adjacent to the nasal septal cartilage in *EIIa-SW* and *Col2-SW*

Since the unique facial phenotypes were found in *Col2-SW*, we focused on the intra-nasal and -facial region to find possible causal factors for the craniofacial anomalies. We found the abnormal fusion between the premaxilla and the vomer in *EIIa-SW* and *Col2-SW* at P7, which is normally patent even at P21 stage. (Figure 2-12). Abnormal vomer formation, which results the palate perforation was only presented on *EIIa-SW* and *Col1-SW* (Figure 2-12, 15 and Table 2-5). Histological observation at mid-sagittal plane of facial region also showed fused phenotype between the premaxilla and the vomer on *EIIa-SW* and *Col2-SW* groups (Figure 2-12C). No cartilaginous tissue was found between two bones. The snout of *Col2-SW* was deviated despite no premature closure of naso-frontal suture (Figure 2-13). Moreover, the formation of perpendicular plate of ethmoid bone was significantly reduced in both mutant groups (Figure 2-14). Interestingly, these effected facial bone components are adjacent to the septal cartilage at the center. Collectively, the facial anomalies in *Col2-SW* implicate the involvement of nasal septal cartilage.

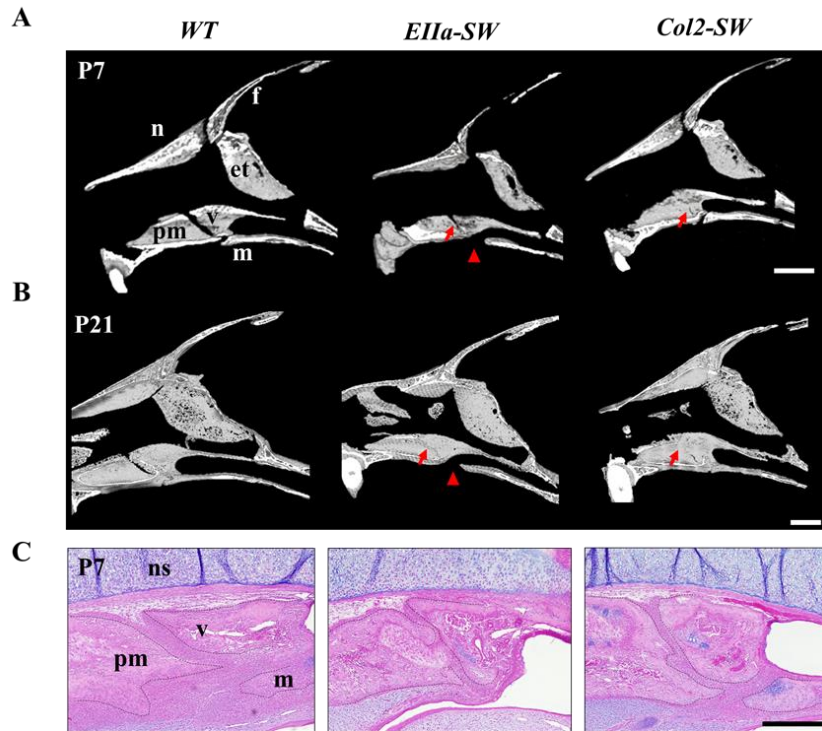


Figure 2–12. Abnormal obliteration of the suture between premaxilla and maxilla bone

(A and B) Micro CT images of mouse skull at mid–sagittal plane at P7 and P21 stages. Red arrows indicate closure between premaxilla and vomer. Red arrowheads indicate palate perforation. Scale bar: 1 mm (C) Hematoxylin, eosin and alcian blue stain of skull at mid–sagittal plane of P7 mice. Broken line indicates the edge of each bones. n, nasal bone; f, frontal bone; pm, premaxilla bone; v, vomer; et, ethmoid bone; ps, presphenoid bone; m, maxilla; ns, nasal septum. Scale bar: 1 mm

Table 2-5. Premaxilla-vomer closure and palate perforation frequency at P7 and P21 stages

	genotypes	premaxilla-vomer closure	palate perforation
P7	<i>WT</i>	0/5	0/5
	<i>EIIa-SW</i>	5/5	5/5
	<i>Col2-SW</i>	5/5	0/5
	<i>Col1-SW</i>	0/5	3/5
P21	<i>WT</i>	0/5	0/5
	<i>EIIa-SW</i>	5/5	5/5
	<i>Col2-SW</i>	5/5	0/5
	<i>Col1-SW</i>	1/5	3/5

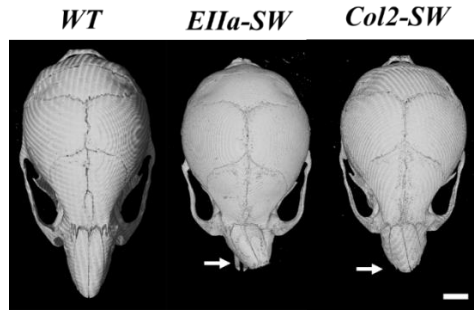


Figure 2–13. Deviated nose of the mutant mice at P21

The superior view of the skull. The white arrows on the mutant mice indicate deviation of nasal bone.

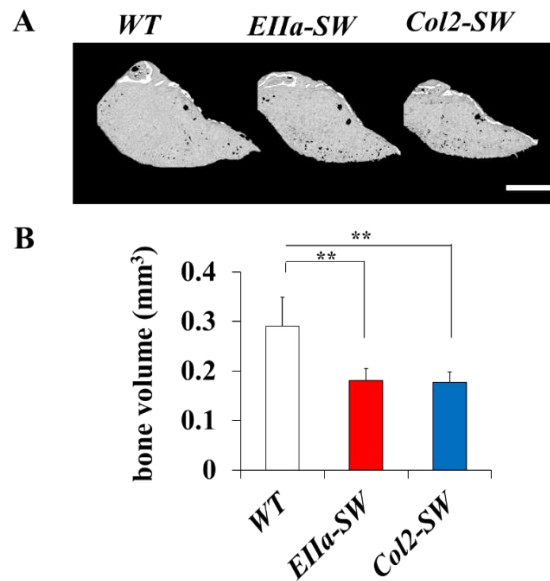


Figure 2–14. Reduced formation of ethmoid bone in the mutant mice

(A) Micro–CT images of perpendicular of ethmoid bone of P21 mice at lateral view and (B) the bone volume measurements. Scale

bar: 1mm. Values are presented as mean \pm SD. * $p \leq 0.0332$,

** $p \leq 0.0021$ ($n = 5$)

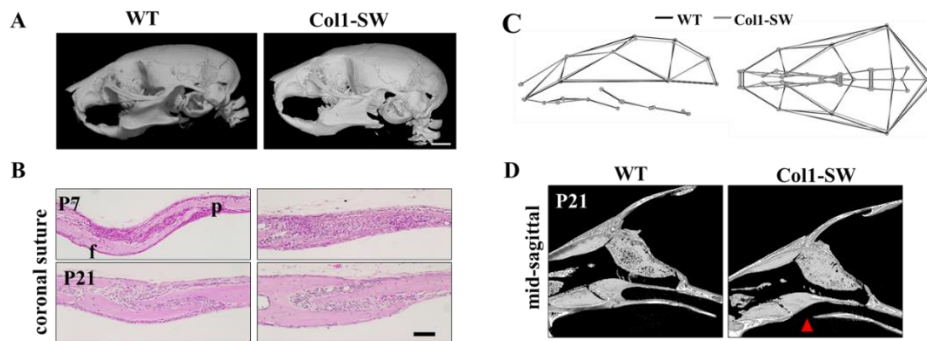


Figure 2–15. *Col1–SW* showed mild craniofacial phenotypes. **(A)** Lateral view of *Col1–SW* skull. Overall skull phenotype of *Col1–SW* is normal. Scale bar: 2 mm **(B)** Histology of coronal suture of WT and *Col1–SW*. *Col1–SW* showed normal suture development. Scale bar: 100 μ m **(C)** The mean skull shape of *Col1–SW* by DFA (black line for WT and grey line for *Col1–SW*). **(D)** Micro–CT image of facial region at mid–sagittal plane. *Col1–SW* showed impaired vomer and palatine development (red arrowhead).

Thickening of septal cartilage altered the structure of the vomer and

the premaxilla bone in *Fgfr2*^{S252W/+} mice

Anatomically, the inferior part of the septal cartilage is surrounded by Y-shaped vomer wings at coronal view (Figure 2-16A). We found the septal cartilage of *EIIa-SW* and *Col2-SW* was dramatically thickened and distorted. With this septal morphology changes, the surrounding vomer wings have been widened and distorted (Figure 2-16A~C). Moreover, the vomer wing length was reduced in *EIIa-SW*, but not in *Col2-SW* (Figure 2-14D). To check the possibility of the effect from altered chondrocyte characters to the abnormal bony fusion, the expression of chondrocyte-derived secretory proteins that might affect to osteoblasts differentiation was examined (Maes 2017; Sanchez et al. 2017). The expression of the factors in the septum chondrocytes influencing osteoblasts was not significantly changed. These histological observations suggest that the abnormal vomer shape and the fusion between the vomer and the premaxilla bone below in both mutant mice (Figure 2-17) might be due to the pressure caused by enlarged septal cartilage.

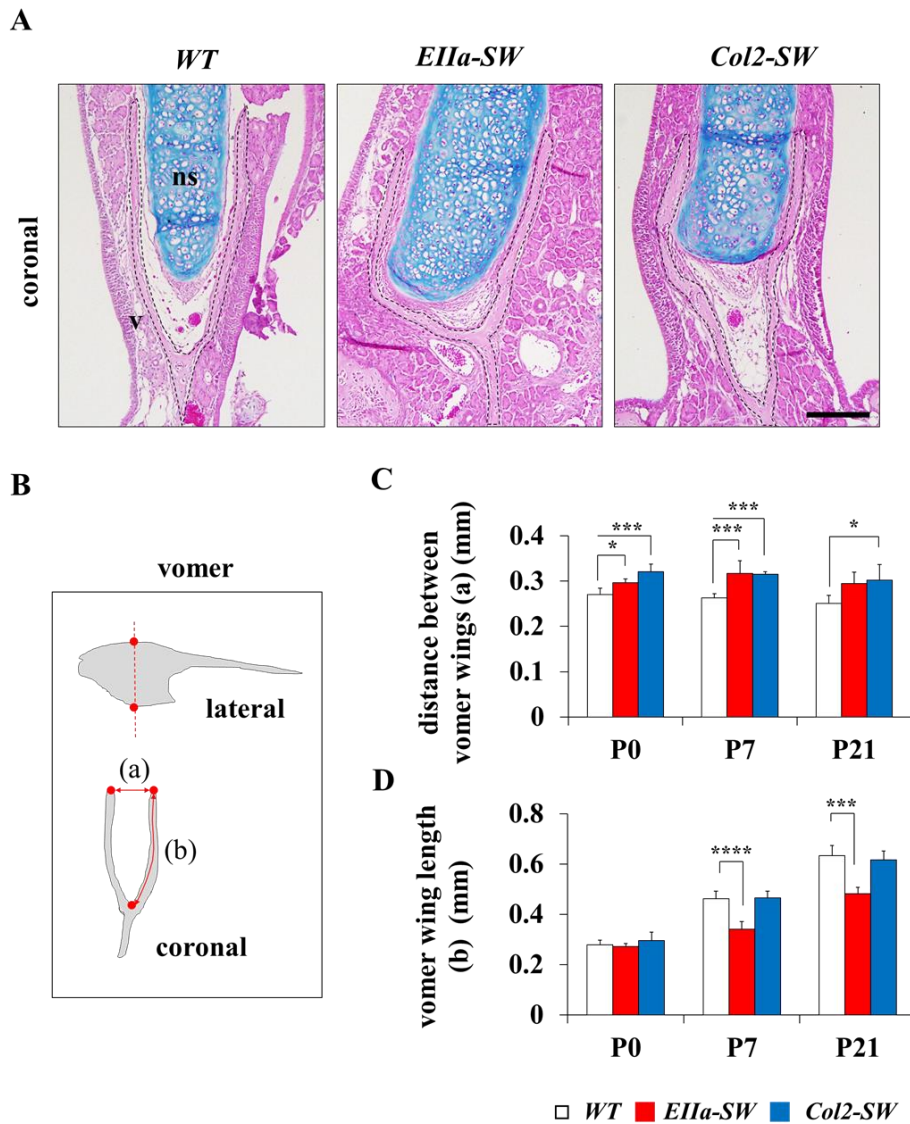


Figure 2–16. *Fgfr2*^{S252W} mutation affects to the vomer growth via changed nasal septum growth

(A) Hematoxylin, eosin and alcian blue stained septal cartilage (ns) and vomer (v) at P21 mice. Dotted line indicate vomer. Scale bar: 200 μ m (B) The schematic image of vomer for linear measurements.

The measurements were performed at coronal plane where the highest and the lowest point on the vomer is seen (red dotted line). Distance between two vomer wings (C) (distance (a) in Figure 2–16B) and the length of vomer wings (D) (length (b) in Figure 2–16B) were measured. The length of two wings were averaged. Values are presented as mean \pm SD. * $p \leq 0.0332$, ** $p \leq 0.0021$, *** $p \leq 0.0002$, **** $p \leq 0.0001$ ($n=5$).

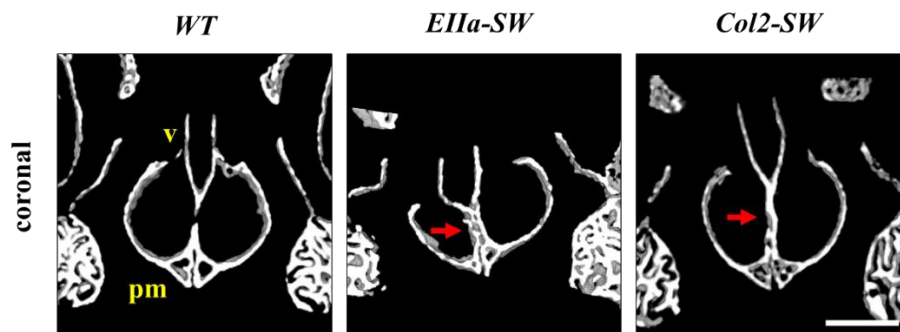


Figure 2–17. Altered septum and vomer growth may induce the fusion of vomer and premaxilla bone

Micro-CT images of the vomer and the premaxilla bone at coronal plane. Red arrows on the mutant mice indicate the fusion of the vomer and the premaxilla bone. Scale bar: 0.5 mm

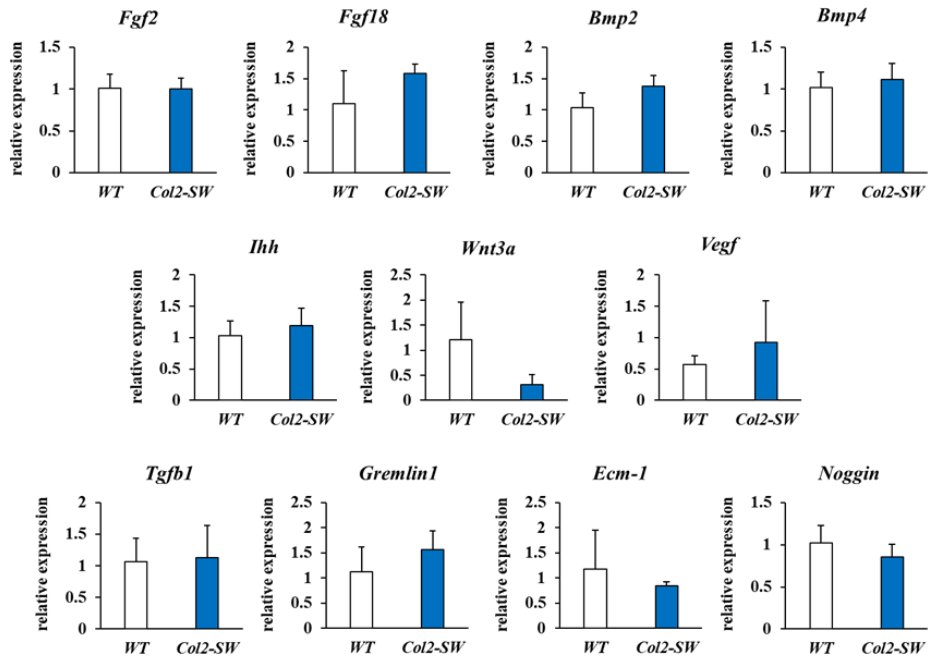


Figure 2–18. Chondrocyte–derived factors influencing bone formation were not affected by *Fgfr2*^{S252W} mutation

Relative gene expression of chondrocyte–derived secretory factors was examined from septal cartilage of P7 mice. The expression level was normalized to *Gapdh*. Values are presented as mean \pm SD. Student *t*-test ($n=4$)

Morphological changes of nasal septal cartilage and septal deviation in *Fgfr2*^{S252W/+} mice

The samples were stained with iodinated contrast agent, so that the contrast-enhanced cartilaginous tissues can be detected by Micro-CT scanning (Gignac et al. 2016). On the coronal plane at the middle of septal cartilage, *EIIa-SW* and *Col2-SW* showed thickened and deviated septal cartilage (Figure 2-18A and B, upper lane, Figure 2-19A and B). *EIIa-SW* showed severer deviation with lowered nasal bone. The major deviated point was between the nasal bone and septal cartilage. With septal deviation, the snout was also deviated (Figure 2-18A and B, lower lane). There was high correlation between the deviating degree of the septum and the nose in the mutant mice (Figure 2-19D). Interestingly, the deviation of the septum and the nose was mostly occurred to the opposite direction (Figure 2-19E). 3D-reconstructed images of septal cartilage showed shortening of antero-posterior length, and thickened and heightened morphological changes in both mutant groups (Figure 2-20A). The septum of *EIIa-SW* was distorted severer than *Col2-SW*, especially the upper region, which is adjacent to the nasal bone. The mean shape changes of the septal cartilage indicate the decrease in septal length and increase in septal height in both mutant mice

(Figure 2–20B). The septal thickness was also dramatically increased compare to WT. These results demonstrated the chondrocyte–specific *Fgfr2*^{S252W} mutation induced septal growth alteration and septal deviation, and it is sufficient for the facial deformity without premature closure of craniofacial sutures.

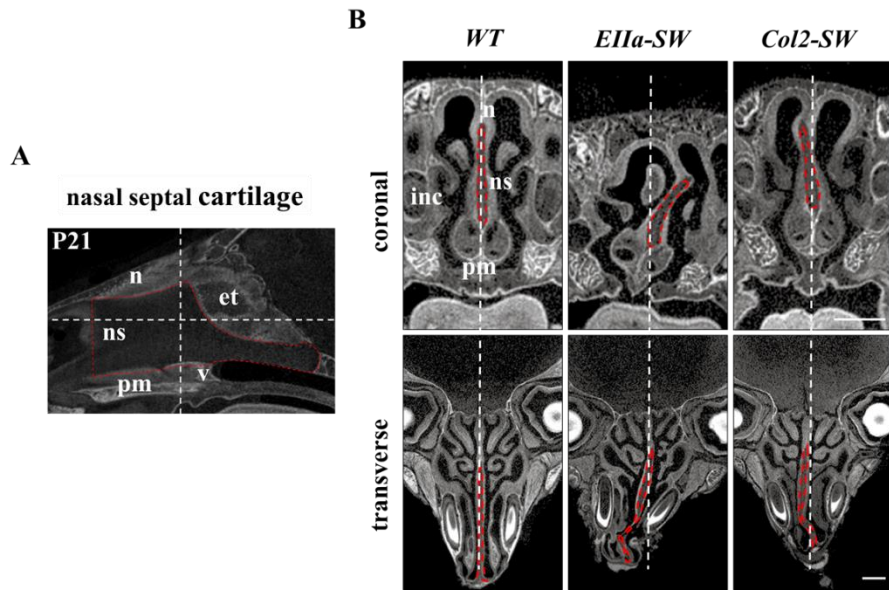


Figure 2–19. Deviation of the nasal septum and the snout in the mutant mice

(A) Mid–sagittal image of nasal cavity of P21 mice stained with Potassium triiodide, the contrast agent (Lugol’s solution) for 48h. Nasal septum was indicated with dotted red line. White line indicates the coronal and transverse plane for further analyses. n, nasal bone; ns, nasal septum; pm, premaxilla; v, vomer; et, perpendicular plate of ethmoid bone. (B) Coronal view (upper lane) and transverse view (lower lane) of nasal cavity. Septal cartilage was indicated with dotted red line. Scale bar: 0.5 mm.

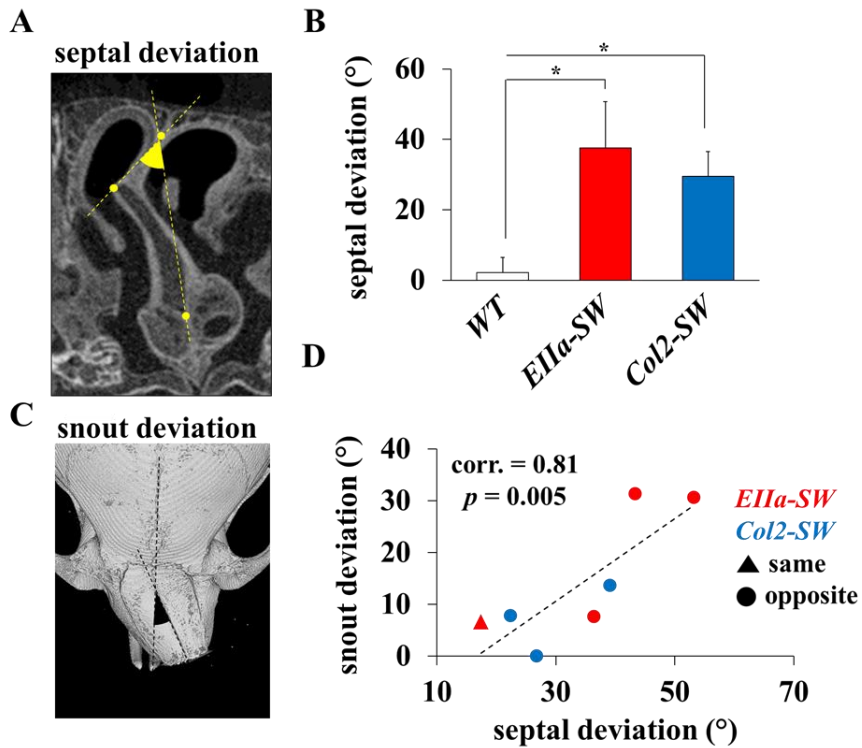


Figure 2–20. Correlation between the deviation of the nasal septum and the nose

(A and B) The measurement of septal deviation on the coronal view of nasal cavity. The septal deviation angle between the most deviated point of the septum and the midline (crossing two points on the nasal bone and the caudal most point of the septum) was measured. (C) The measurement of snout deviation. The angle between two black dotted lines, parallel to the inter-frontal suture and the nasal bone was measured. (D) Correlation between the

degree of deviation of the nose and the septum of mutant mice. Correlation efficiency and p -value are displayed in the graph. Triangle indicates the mutant mice, which show same deviating direction of the nasal septum and the snout. Round indicates opposite deviating direction of the septum and the snout. 6 of 7 mutant mice showed opposite deviating direction of the septum and the snout. Values are presented as mean \pm SD. * $p \leq 0.0332$. ($n \geq 3$)

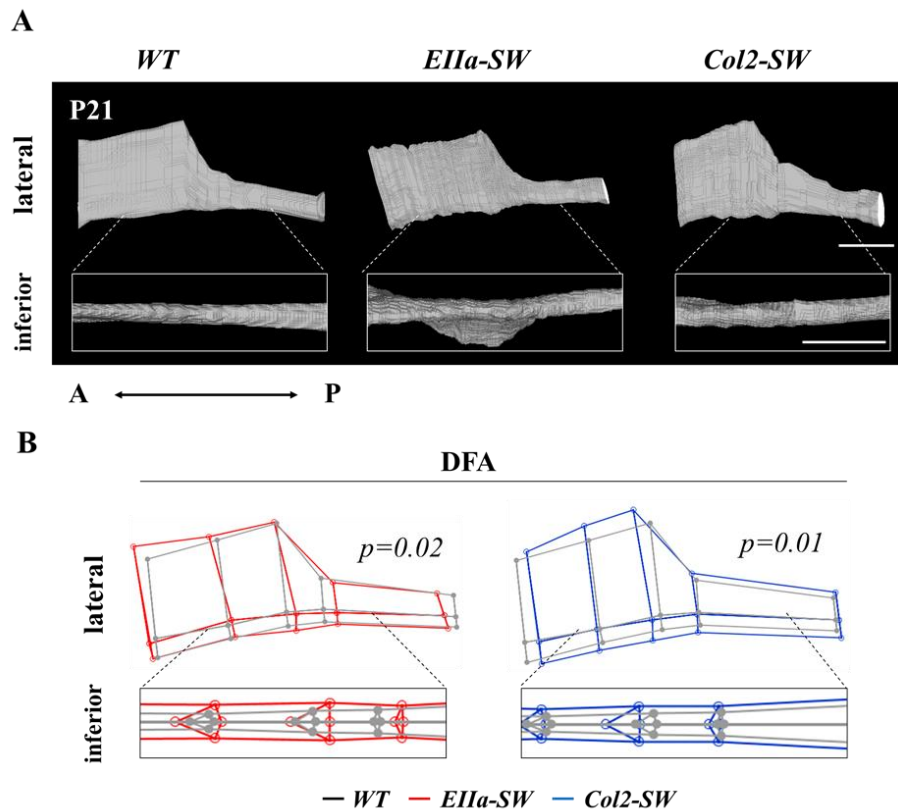


Figure 2–21. Thickening of the nasal septal cartilage

(A) Three-dimensional reconstructed image of nasal septal cartilage of P21 mouse at lateral and inferior views (magnified in the white box). Scale bar: 1 mm (B) Mean septal cartilage shape of *EIIa-SW* and *Col2-SW* were compared with that of WT by DFA with wireframe images. Inferior view was magnified in the box. *P*-values for 1,000 permutation tests between two groups are showed below the wireframe images.

Increased chondrocyte hypertrophy and cellular size induced thickening of the nasal septal cartilage

To examine the effect of *Fgfr2*^{S252W} on the septum chondrocyte, gene expression and histological assessments were performed on the septal cartilage of *Col2-SW*. SOX9, a marker of early stage of chondrocyte, was decreased at all the observed stages of *Col2-SW* (Figure 2-21). In contrast, RUNX2, a marker of hypertrophy of chondrocyte, was increased on the mutant septal cartilage at P21 (Figure 2-22). Expression of type X collagen was also increased on the septal cartilage matrix of *Col2-SW* indicating increased chondrocyte hypertrophy and changed septal matrix character (Figure 2-23A and B). Other hypertrophy markers, *Osteopontin* and *matrix metalloproteinase-13 (Mmp13)* were also increased in the mutant septum chondrocytes (Figure 2-23 C and D). As cellular hypertrophy accelerated, cellular size of septum chondrocytes was also significantly increased (Figure 2-24A). The cellular area occupying the septal cartilage matrix was increased by 5.1 % (Figure 2-24B). However, the number of chondrocytes was not significantly different (Figure 2-24C). Collectively, these results indicate that *Fgfr2*^{S252W} mutation on the nasal septum chondrocyte increases its hypertrophy, altered the nature of cartilage matrix and finally,

thickening of the septal cartilage.

FGFR-related craniosynostosis patients frequently showed tracheal cartilaginous sleeve that respiratory defect by solid and fused tracheal cartilage (Wenger et al. 2017). *EIIa-SW* and *Col2-SW* mice also showed increased thickness of tracheal cartilages (Figure 2-26). The cartilages of *EIIa-SW* mice were more clearly stained with alcian blue than those of WT. These data indicate that the respiratory problems might be caused by airway obstruction by thickening of nasal septum or tracheal cartilage, rather than rib cartilage defect.

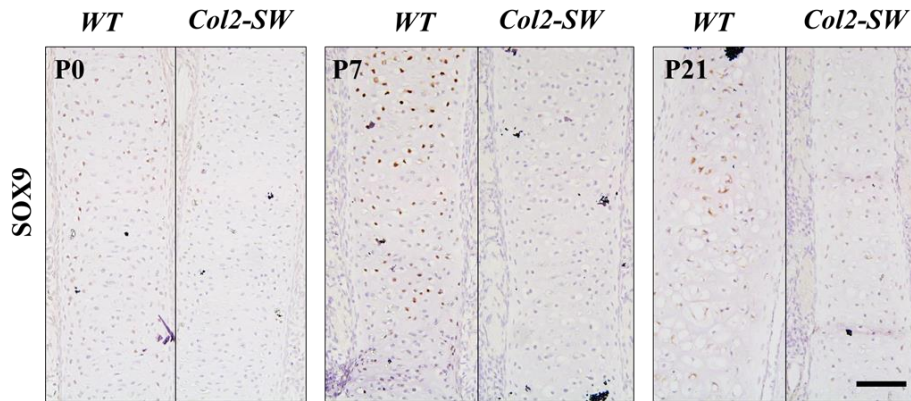


Figure 2–22. SOX9 expression was reduced by *Fgfr2*^{S252W} mutation on the septum chondrocytes

Immunohistochemistry for SOX9 on the septal cartilage of P0, P7 and P21 mice. Scale bar: 100 μ m

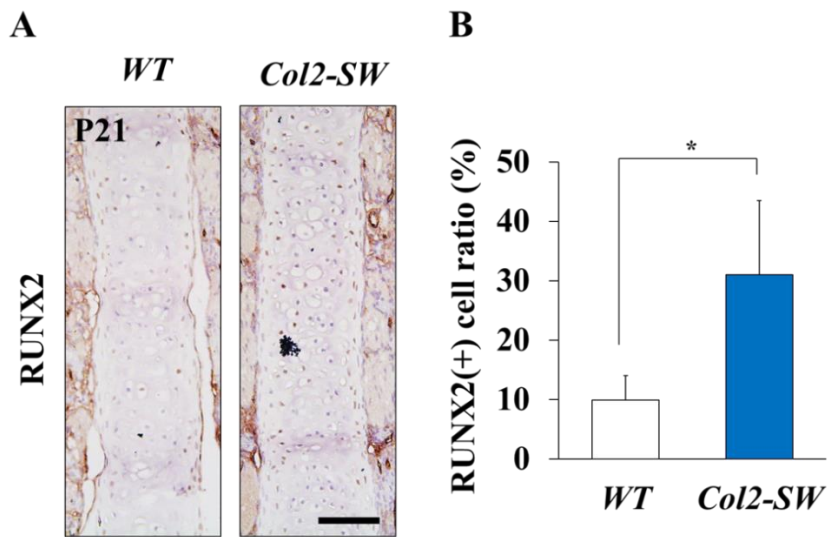


Figure 2–23. RUNX2 expression was increased by *Fgfr2*^{S252W} mutation on the septum chondrocytes

(A) Immunohistochemistry for RUNX2 on the septal cartilage of P21 mice. Scale bar: 100 μ m (B) RUNX2–positive cells were counted. Four slides were randomly selected per mouse, three WT and four *Col2–SW* mice were used for histological assessments. Values are presented as mean \pm SD. Student *t*-test, * $p \leq 0.05$.

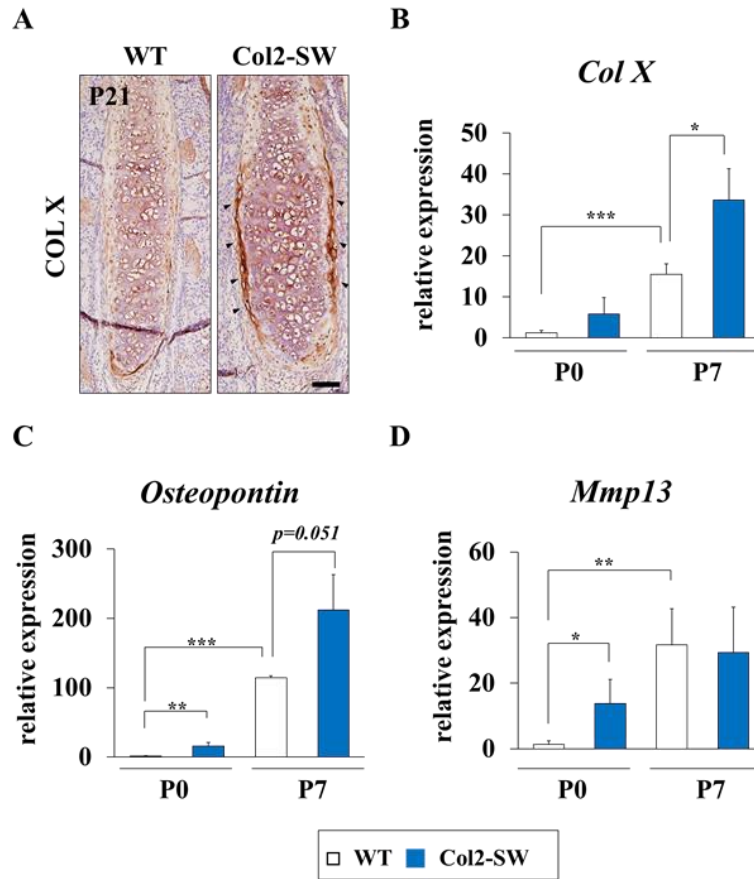


Figure 2–24. Chondrocyte hypertrophy markers were increased with *Fgfr2*^{S252W} mutation

(A) Immunohistochemistry for type X collagen (COL X) on the P21 septal cartilage. Black arrowheads indicate increased COL X expression at the edge of septal cartilage of *Col2-SW*. Gene expression of chondrocyte hypertrophic markers, (B) *ColX*, (C) *Osteopontin* and (D) *Mmp13* in the septal cartilage at P0 and P7 stages. The expression level was normalized to *Gapdh*. $n=4$ for P0

and $n=3$ for P7 mice for quantitative PCR. Values are presented as mean \pm SD. Student t -test, $*p\leq 0.05$, $**p\leq 0.01$, $***p\leq 0.001$.

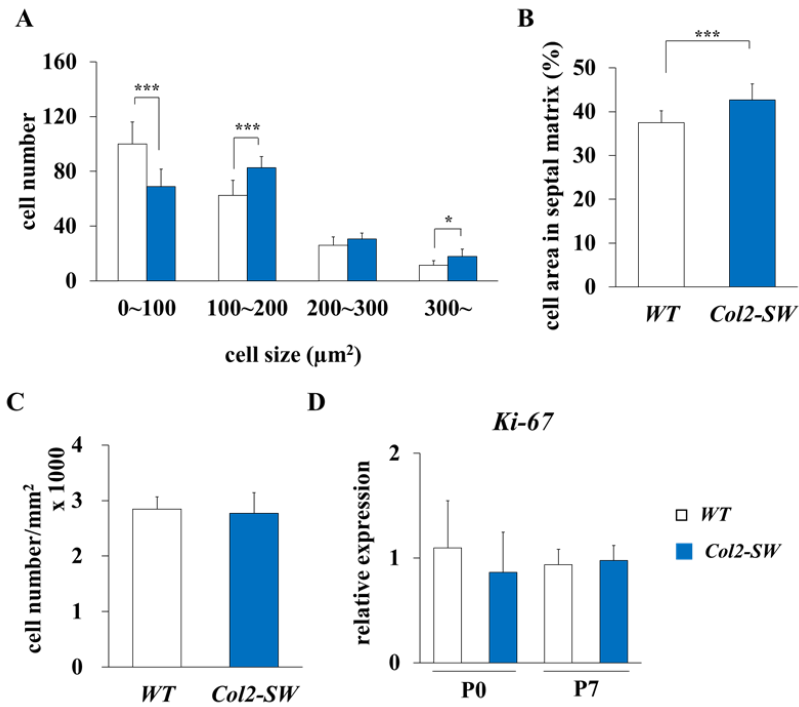


Figure 2–25. Increased septum chondrocyte size in *Col2-SW*

(A) Septum chondrocyte size distribution on the P21 septal cartilage. (B) Cellular area on the septal cartilage matrix. (C) The number of septum chondrocytes per mm^2 of septal matrix. Values are presented as mean \pm SD. Student t -test, $*p\leq 0.05$, $**p\leq 0.01$, $***p\leq 0.001$. Four slides were randomly selected per mouse, three WT and four *Col2-SW* mice were used for histological assessments.

Fgfr2^{S252W/+} mice showed delayed rib cartilage ossification and increased tracheal cartilage dense

Since *Fgfr2*^{S252W/+} mice showed high lethality due to respiratory problems, we additionally checked the possibility of abnormal rib development, which grows by endochondral ossification process (DeSesso and Scialli 2018). The number and the patterning of ribs were found normal (Figure 2–26A). However, the ossification of costal cartilage of ribs were reduced in both mutant mice (Figure 2–26B). Histological observation also presented the reduced mineralization and more compact cartilage formation (Figure 2–17A). Mutant costal cartilage expressed higher level of COL2A1 and COL X (Figure 2–17B), which indicate increased chondrocyte differentiation. However, mutant mice did not show notable defect in the rib development at P21 stage. These results might imply the temporarily delayed rib cartilage ossification by abnormally accelerated terminal chondrogenesis, however, it did may not induce significant breathing problems in *Fgfr2*^{S252W/+} mice.

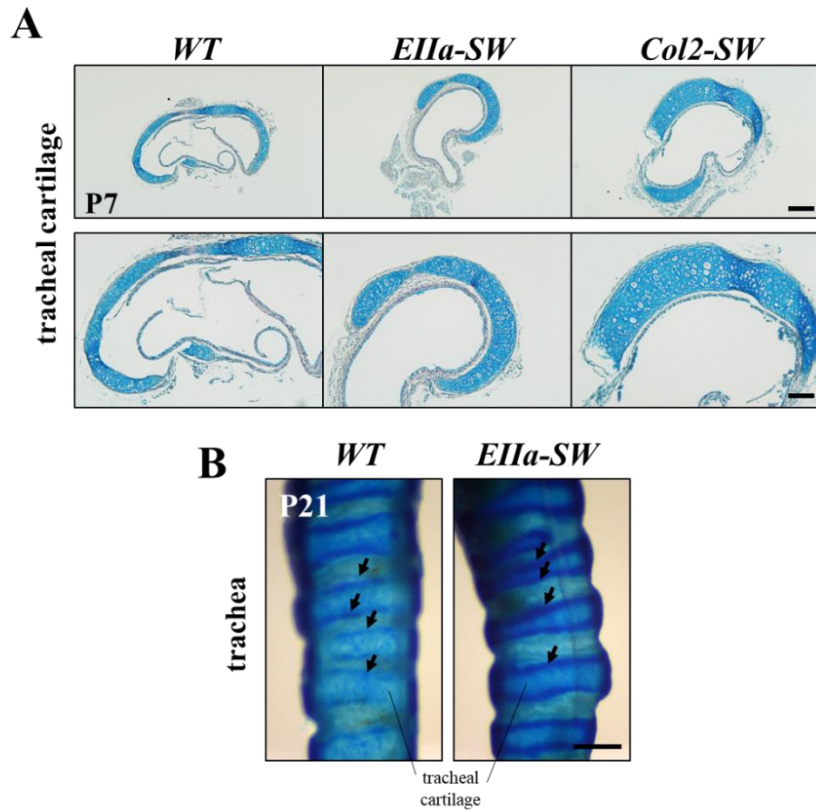


Figure 2–26. Thickening of tracheal cartilage in mutant mice

(A) Sectioned tracheal cartilage from P7 *WT* and mutant mice were stained with alcian blue. *EIIa-SW* and *Col2-SW* mice presented thicker tracheal cartilage compare to that of *WT*. Scale bar: 200 μm (upper) and 100 μm (lower) (B) Trachea from P21 was stained with alcian blue solution. Tracheal cartilage in *EIIa-SW* mice was more clearly stained with alcian blue (black arrows in magnified images in lower lane). Scale bar: 0.5 mm.

Discussion

In patients with Apert syndrome, midface hypoplasia and airway obstruction are the major problems that must be managed during childhood (Mathijssen 2015). However, the pathogenic mechanism and the intrinsic contributing factors of midface hypoplasia remain unclear. Breathing problems caused by a deviated nasal septum, choanal atresia, and narrowed tracheal cartilage sleeve (Xie et al. 2016) are related to abnormalities in the nasal septum or facial cartilaginous tissue growth. In this study, we demonstrated that abnormal septal cartilage development acts as a major contributor to midface hypoplasia in a mouse model.

Patients with Apert syndrome are treated with decompressive surgery to relieve raised pressure in the craniofacial region (Marucci et al. 2008). However, intracranial pressure was not the only cause of the midfacial anomalies, since the cranium grows rapidly during the first 5 years, whereas maxillary growth is still active at the ages of 12 to 14 (Singh 2015). Hypoplastic facial phenotypes of *Col2-SW* mice in the absence of premature craniofacial suture closure imply the importance of intrafacial features in Apert syndrome. The premature closure of the vomero-premaxilla suture found in *Col2-*

SW mice could directly cause anteroposterior facial shortening (Lowe et al. 2000; Ren et al. 2014). The distortion of the shape of the vomer also could result in respiratory failure (Lesciotto et al. 2018); however, the abnormal fusion was not expected because the premaxilla and the vomer does not grow by endochondral bone formation (Singh 2015). In the mutant mice, we also found elevated nasions, deviated nasal bones, and undergrowth of the perpendicular plate of the ethmoid bone, which grows with endochondral bone formation from septum chondrocytes (Wealthall and Herring 2006). These results strongly indicate the involvement of changes in septal cartilage growth in abnormal midfacial phenotypes. Increased chondrocyte hypertrophy, changed septal matrix structure, and enlarged septal cartilage would impinge upon the vomer and nasal bone, resulting in facial deformities (Al Dayeh et al. 2013; Setlur and Goyal 2011).

Early surgical treatment of the cranium of Apert syndrome should be conducted (~2 years of age) to relieve severe respiratory distress and intracranial hypertension (Fadda et al. 2015). Later during growth and even up to adulthood, serial anterior skull and maxilla advancement are considered as a second step. Similar to humans with Apert syndrome, *EIIa-SW* mice with craniosynostosis showed

severe craniofacial anomalies at birth (Kim et al. 2020a). By contrast, *Col2-SW* mice showed normal craniofacial phenotypes at birth and relatively progressive development of midface hypoplasia, especially with abnormally thickened septal cartilage. Therefore, surgical resection of thickened septum during the treatment of Apert syndrome may improve midface morphology and relieve the burden of multiple surgical steps.

The septal thickening and elevation might result in septal deviation at the junction of solid nasal bone above (Setlur and Goyal 2011). *EIIa-SW* mice showed more severe septal deviation than *Col2-SW* mice because of premature closure of the nasofrontal suture and depressed nasion. The deviation occurred mainly between the nasal bone and septal cartilage, and it reflected the hardened matrix structure of septal cartilage. The degree of septal deviation and nasal deviation were strongly correlated. Furthermore, horizontal sectional views showed that the nasal deviation occurred on the opposite side of the septal deviation in six of seven mutant mice. In the patients with septal deviation, an external anteroposterior C-shaped septal deviation is commonly on the opposite side of internal deviation (Cerkes 2011), which is believed to be the adaptation for securing the airway. These data imply that septal cartilage has an essential

role in determining the maxillary shape; furthermore, the surgical correction of nasal septum could lead to proper facial growth.

In previous studies, to relieve craniosynostosis and midface hypoplasia in Apert syndrome, we targeted PIN1, an enzyme in the FGF/FGFR signaling pathway with genetic or pharmacological inhibition (Kim et al. 2020a; Shin et al. 2018). Since the posttranslational modification of RUNX2 by PIN1 acts critical role in FGF/FGFR signaling (Kim et al. 2020b; Kim et al. 2003b), we attenuated hyper-stabilized RUNX2 and restored premature fusion of craniofacial sutures in *Fgfr2*^{S252W/+} mice by inhibiting PIN1. Although we did not examine the effect of attenuating PIN1 in *Col2-SW* mice in this study as the trial has been successfully conducted in *EIIa-SW*, we can propose a combination of the pharmacological PIN1 inhibition and the surgical septal correction may improve the treatment process.

Basically, FGF signaling accelerates hypertrophic differentiation and reduces its proliferation mainly through FGFR3 in the differentiation of chondrocyte (Ornitz and Legeai-Mallet 2017). Some investigators have studied the cartilage issues found with the *Fgfr2* mutation. In syndromic craniosynostosis, including Apert syndrome, solid

tracheal cartilage sleeve is commonly reported as a respiratory defect in humans and mouse models (Wang et al. 2005; Wenger et al. 2017). Recent study also demonstrated thickened nasal septum and narrowed nasal airway in the mouse model of Apert syndrome on neonate stage (Holmes et al. 2018). Similarly, our data demonstrated increased septum chondrocyte hypertrophy and thickening of the septum. Furthermore, 3-D septal shape analysis and histological assessments during growth highlighted the importance of septal growth in the facial development and airway formation.

We confirmed that septum chondrocytes basically undergo hypertrophy during development. Other studies also showed the capacity of nasal septum chondrocytes for hypertrophy and mineralization under certain conditions in both *in vitro* and *in vivo* models (Pavlov et al. 2003; Pippenger et al. 2015). *Fgfr2*^{S252W} mutations accelerate this process in the nasal septum, although we did not observe ectopic ossification until P21. We also found the septal thickening is caused mainly by enlarged chondrocyte size rather than by an increase in the number of chondrocytes. Our previous observation also showed no significant change in chondrocyte proliferation in cranial base synchondroses in the same mouse model (Kim et al. 2020a). By contrast, (Holmes et al. 2018)

reported a transient increase of chondrocyte proliferation at the embryonic stage, but they also confirmed the thickening of septal cartilage without proliferation change at later stages. These studies indicate that FGF signaling has a tissue- and stage-specific role in craniofacial cartilage development.

In this study, by using a mouse model of chondrocyte-specific *Fgfr2*^{S252W} expression, we demonstrated that abnormal growth of the nasal septal cartilage, caused by increased cellular hypertrophy, is a major cause of midface hypoplasia. Our results strongly suggest that the risk of respiratory failure and aesthetic problems can be reduced by surgical correction of nasal septal cartilage at an early age in patients with Apert syndrome.

V. Conclusion

In this study, we provided the insight of the pathological mechanisms of midface hypoplasia by conducting detailed three-dimensional morphological assessments. In Apert syndrome mouse model, facial suture closure, cranial base flexion and septal cartilage thickening act as a main contributing factor of midface hypoplasia. Understanding the growth patterns of facial bones, cranial base and nasal septum might complement the risky surgical treatment for the patients with Apert syndrome. Moreover, we suggested attenuation of PIN1 as a therapeutic strategy to rescue the midfacial phenotypes. Our multi-dimensional analysis on Apert syndrome mouse model could provide the insight for the advanced treatment strategy to reduce the burden of surgical process and to improve prognosis.

VI. References

- Ahmed J, Marucci D, Cochrane L, Heywood RL, Wyatt ME, Leighton SE. 2008. The role of the nasopharyngeal airway for obstructive sleep apnea in syndromic craniosynostosis. *J Craniofac Surg.* 19(3):659–663.
- Al Dayeh AA, Rafferty KL, Egbert M, Herring SW. 2013. Real-time monitoring of the growth of the nasal septal cartilage and the nasofrontal suture. *Am J Orthod Dentofacial Orthop.* 143(6):773–783.
- Basheer B, Hegde KS, Bhat SS, Umar D, Baroudi K. 2014. Influence of mouth breathing on the dentofacial growth of children: A cephalometric study. *J Int Oral Health.* 6(6):50–55.
- Boulet SL, Rasmussen SA, Honein MA. 2008. A population-based study of craniosynostosis in metropolitan atlanta, 1989–2003. *Am J Med Genet A.* 146A(8):984–991.
- Bradshaw RA, Dennis EA. 2010. *Handbook of cell signaling.* Vol. 2 vol. 2. Amsterdam: Academic Press.
- Britto JA, Chan JC, Evans RD, Hayward RD, Thorogood P, Jones BM. 1998. Fibroblast growth factor receptors are expressed in craniosynostotic sutures. *Plast Reconstr Surg.* 101(2):540–543.
- Cerkes N. 2011. The crooked nose: Principles of treatment. *Aesthet Surg J.* 31(2):241–257.
- Chen L, Li D, Li CL, Engel A, Deng CX. 2003. A ser250trp substitution in mouse fibroblast growth factor receptor 2 (fgfr2) results in craniosynostosis. *Bone.* 33(2):169–178.
- Connolly JP, Gruss J, Seto ML, Whelan MF, Ellenbogen R, Weiss A,

- Buchman SR, Cunningham ML. 2004. Progressive postnatal craniosynostosis and increased intracranial pressure. *Plast Reconstr Surg.* 113(5):1313–1323.
- Cunningham ML, Seto ML, Ratisoontorn C, Heike CL, Hing AV. 2007. Syndromic craniosynostosis: From history to hydrogen bonds. *Orthod Craniofac Res.* 10(2):67–81.
- Czeizel AE, Elek C, Susanszky E. 1993. Birth prevalence study of the apert syndrome. *Am J Med Genet.* 45(3):392–393.
- Delezoide AL, Benoist–Lasselin C, Legeai–Mallet L, Le Merrer M, Munnich A, Vekemans M, Bonaventure J. 1998. Spatio–temporal expression of fgfr 1, 2 and 3 genes during human embryo–fetal ossification. *Mech Dev.* 77(1):19–30.
- Deng CX, Wynshaw–Boris A, Shen MM, Daugherty C, Ornitz DM, Leder P. 1994. Murine fgfr–1 is required for early postimplantation growth and axial organization. *Genes Dev.* 8(24):3045–3057.
- DeSesso JM, Scialli AR. 2018. Bone development in laboratory mammals used in developmental toxicity studies. *Birth Defects Research.* 110(15):1157–1187.
- Dunyak BM, Gestwicki JE. 2016. Peptidyl–proline isomerases (ppiases): Targets for natural products and natural product–inspired compounds. *J Med Chem.* 59(21):9622–9644.
- Eswarakumar VP, Horowitz MC, Locklin R, Morriss–Kay GM, Lonai P. 2004. A gain–of–function mutation of fgfr2c demonstrates the roles of this receptor variant in osteogenesis. *Proc Natl Acad Sci U S A.* 101(34):12555–12560.
- Eswarakumar VP, Monsonogo–Ornan E, Pines M, Antonopoulou I, Morriss–Kay GM, Lonai P. 2002. The iiic alternative of fgfr2

is a positive regulator of bone formation. *Development*. 129(16):3783–3793.

Eswarakumar VP, Ozcan F, Lew ED, Bae JH, Tome F, Booth CJ, Adams DJ, Lax I, Schlessinger J. 2006. Attenuation of signaling pathways stimulated by pathologically activated fgf-receptor 2 mutants prevents craniosynostosis. *Proc Natl Acad Sci U S A*. 103(49):18603–18608.

Fadda MT, Ierardo G, Ladniak B, Di Giorgio G, Caporlingua A, Raponi I, Silvestri A, Group of Apert syndrome PUISUoRI. 2015. Treatment timing and multidisciplinary approach in apert syndrome. *Ann Stomatol (Roma)*. 6(2):58–63.

Forte AJ, Lu X, Hashim PW, Steinbacher DM, Alperovich M, Persing JA, Alonso N. 2019. Airway analysis in apert syndrome. *Plast Reconstr Surg*. 144(3):704–709.

Fujimori F, Takahashi K, Uchida C, Uchida T. 1999. Mice lacking pin1 develop normally, but are defective in entering cell cycle from g(0) arrest. *Biochem Biophys Res Commun*. 265(3):658–663.

Ge CX, Xiao GZ, Jiang D, Yang Q, Hatch NE, Roca H, Franceschi RT. 2009. Identification and functional characterization of erk/mapk phosphorylation sites in the runx2 transcription factor. *Journal of Biological Chemistry*. 284(47):32533–32543.

Gignac PM, Kley NJ, Clarke JA, Colbert MW, Morhardt AC, Cerio D, Cost IN, Cox PG, Daza JD, Early CM et al. 2016. Diffusible iodine-based contrast-enhanced computed tomography (dicect): An emerging tool for rapid, high-resolution, 3-d imaging of metazoan soft tissues. *J Anat*. 228(6):889–909.

Gothel SF, Marahiel MA. 1999. Peptidyl-prolyl cis-trans isomerases,

- a superfamily of ubiquitous folding catalysts. *Cellular and Molecular Life Sciences*. 55(3):423–436.
- Griffiths SK, Campbell JP. 2015. Placental structure, function and drug transfer. *Bja Educ*. 15(2):84–89.
- Grymer LF, Bosch C. 1997. The nasal septum and the development of the midface. A longitudinal study of a pair of monozygotic twins. *Rhinology*. 35(1):6–10.
- Hall BK, Precious DS. 2013. Cleft lip, nose, and palate: The nasal septum as the pacemaker for midfacial growth. *Oral Surg Oral Med Oral Pathol Oral Radiol*. 115(4):442–447.
- Harfe BD, Scherz PJ, Nissim S, Tian H, McMahon AP, Tabin CJ. 2004. Evidence for an expansion-based temporal shh gradient in specifying vertebrate digit identities. *Cell*. 118(4):517–528.
- Heggie AA, Kumar R, Shand JM. 2013. The role of distraction osteogenesis in the management of craniofacial syndromes. *Ann Maxillofac Surg*. 3(1):4–10.
- Hennig L, Christner C, Kipping M, Schelbert B, Rucknagel KP, Grabley S, Kullertz G, Fischer G. 1998. Selective inactivation of parvulin-like peptidyl-prolyl cis/trans isomerases by juglone. *Biochemistry*. 37(17):5953–5960.
- Holmes G, O'Rourke C, Motch Perrine SM, Lu N, van Bakel H, Richtsmeier JT, Jabs EW. 2018. Midface and upper airway dysgenesis in fgfr2-related craniosynostosis involves multiple tissue-specific and cell cycle effects. *Development*. 145(19).
- Howe AM, Hawkins JK, Webster WS. 2004. The growth of the nasal septum in the 6–9 week period of foetal development—warfarin embryopathy offers a new insight into prenatal facial

- development. *Aust Dent J.* 49(4):171–176.
- Iseki S, Wilkie AO, Heath JK, Ishimaru T, Eto K, Morriss–Kay GM. 1997. *Fgfr2* and osteopontin domains in the developing skull vault are mutually exclusive and can be altered by locally applied *fgf2*. *Development.* 124(17):3375–3384.
- Islam R, Yoon WJ, Ryoo HM. 2017. *Pin1*, the master orchestrator of bone cell differentiation. *Journal of Cellular Physiology.* 232(9):2339–2347.
- Itoh N, Ornitz DM. 2004. Evolution of the *fgf* and *fgfr* gene families. *Trends Genet.* 20(11):563–569.
- Jin YR, Han XH, Taketo MM, Yoon JK. 2012. *Wnt9b*–dependent *fgf* signaling is crucial for outgrowth of the nasal and maxillary processes during upper jaw and lip development. *Development.* 139(10):1821–1830.
- Johnson D, Wilkie AO. 2011. Craniosynostosis. *Eur J Hum Genet.* 19(4):369–376.
- Kasai K, Moro T, Kanazawa E, Iwasawa T. 1995. Relationship between cranial base and maxillofacial morphology. *Eur J Orthodont.* 17(5):403–410.
- Kim B, Shin H, Kim W, Kim H, Cho Y, Yoon H, Baek J, Woo K, Lee Y, Ryoo H. 2020a. *Pin1* attenuation improves midface hypoplasia in a mouse model of apert syndrome. *J Dent Res.* 99(2):223–232.
- Kim HJ, Kim JH, Bae SC, Choi JY, Kim HJ, Ryoo HM. 2003a. The protein kinase c pathway plays a central role in the fibroblast growth factor–stimulated expression and transactivation activity of *runx2*. *J Biol Chem.* 278(1):319–326.
- Kim HJ, Kim WJ, Ryoo HM. 2020b. Post–translational regulations of

- transcriptional activity of runx2. *Mol Cells*. 43(2):160–167.
- Kim HJ, Lee MH, Park HS, Park MH, Lee SW, Kim SY, Choi JY, Shin HI, Kim HJ, Ryoo HM. 2003b. Erk pathway and activator protein 1 play crucial roles in fgf2-stimulated premature cranial suture closure. *Dev Dyn*. 227(3):335–346.
- Klingenberg CP. 2011. MorphoJ: An integrated software package for geometric morphometrics. *Mol Ecol Resour*. 11(2):353–357.
- Klingenberg CP, McIntyre GS. 1998. Geometric morphometrics of developmental instability: Analyzing patterns of fluctuating asymmetry with procrustes methods. *Evolution*. 52(5):1363–1375.
- Kreiborg S, Marsh JL, Cohen MM, Jr., Liversage M, Pedersen H, Skovby F, Borgesen SE, Vannier MW. 1993. Comparative three-dimensional analysis of ct-scans of the calvaria and cranial base in apert and crouzon syndromes. *J Craniomaxillofac Surg*. 21(5):181–188.
- Lajeunie E, Cameron R, El Ghouzzi V, de Parseval N, Journeau P, Gonzales M, Delezoide AL, Bonaventure J, Le Merrer M, Renier D. 1999. Clinical variability in patients with apert's syndrome. *J Neurosurg*. 90(3):443–447.
- Lazarus JE, Hegde A, Andrade AC, Nilsson O, Baron J. 2007. Fibroblast growth factor expression in the postnatal growth plate. *Bone*. 40(3):577–586.
- Lee KKL, Stanier P, Pauws E. 2019. Mouse models of syndromic craniosynostosis. *Mol Syndromol*. 10(1–2):58–73.
- Lee TH, Tun-Kyi A, Shi R, Lim J, Soohoo C, Finn G, Balastik M, Pastorino L, Wulf G, Zhou XZ et al. 2009. Essential role of pin1 in the regulation of trf1 stability and telomere maintenance.

- Nature Cell Biology. 11(1):97–U212.
- Lesciotta KM, Heuze Y, Jabs EW, Bernstein JM, Richtsmeier JT. 2018. Choanal atresia and craniosynostosis: Development and disease. *Plast Reconstr Surg.* 141(1):156–168.
- Li SL, Quarto N, Longaker MT. 2010. Activation of fgf signaling mediates proliferative and osteogenic differences between neural crest derived frontal and mesoderm parietal derived bone. *Plos One.* 5(11):e14033.
- Lim KE, Park NR, Che X, Han MS, Jeong JH, Kim SY, Park CY, Akiyama H, Kim JE, Ryoo HM et al. 2016. Core binding factor beta of osteoblasts maintains cortical bone mass via stabilization of runx2 in mice. *J Bone Miner Res.* 31(1):245.
- Liou YC, Zhou XZ, Lu KP. 2011. Prolyl isomerase pin1 as a molecular switch to determine the fate of phosphoproteins. *Trends Biochem Sci.* 36(10):501–514.
- Lowe LH, Booth TN, Joglekar JM, Rollins NK. 2000. Midface anomalies in children. *Radiographics.* 20(4):907–922; quiz 1106–1107, 1112.
- Lu KP, Hanes SD, Hunter T. 1996. A human peptidyl–prolyl isomerase essential for regulation of mitosis. *Nature.* 380(6574):544–547.
- Lu KP, Zhou XZ. 2007. The prolyl isomerase pin1: A pivotal new twist in phosphorylation signalling and disease. *Nat Rev Mol Cell Biol.* 8(11):904–916.
- Maes C. 2017. Signaling pathways effecting crosstalk between cartilage and adjacent tissues seminars in cell and developmental biology: The biology and pathology of cartilage. *Seminars in Cell & Developmental Biology.* 62:16–33.

- Mai S, Wei K, Flenniken A, Adamson SL, Rossant J, Aubin JE, Gong SG. 2010. The missense mutation w290r in *fgfr2* causes developmental defects from aberrant *iiib* and *iiic* signaling. *Dev Dyn*. 239(6):1888–1900.
- Martelli H, Jr., Paranaíba LM, de Miranda RT, Orsi J, Jr., Coletta RD. 2008. Apert syndrome: Report of a case with emphasis on craniofacial and genetic features. *Pediatr Dent*. 30(6):464–468.
- Martinez–Abadias N, Holmes G, Pankratz T, Wang Y, Zhou X, Jabs EW, Richtsmeier JT. 2013. From shape to cells: Mouse models reveal mechanisms altering palate development in apert syndrome. *Dis Model Mech*. 6(3):768–779.
- Marucci DD, Dunaway DJ, Jones BM, Hayward RD. 2008. Raised intracranial pressure in apert syndrome. *Plast Reconstr Surg*. 122(4):1162–1168; discussion 1169–1170.
- Mathijssen IM. 2015. Guideline for care of patients with the diagnoses of craniosynostosis: Working group on craniosynostosis. *J Craniofac Surg*. 26(6):1735–1807.
- Melnik BC. 2009. Role of *fgfr2*–signaling in the pathogenesis of acne. *Dermatoendocrinol*. 1(3):141–156.
- Minina E, Kreschel C, Naski MC, Ornitz DM, Vortkamp A. 2002. Interaction of *fgf*, *lhh/pthlh*, and *bmp* signaling integrates chondrocyte proliferation and hypertrophic differentiation. *Developmental Cell*. 3(3):439–449.
- Miraoui H, Oudina K, Petite H, Tanimoto Y, Moriyama K, Marie PJ. 2009. Fibroblast growth factor receptor 2 promotes osteogenic differentiation in mesenchymal cells via *erk1/2* and protein kinase c signaling. *J Biol Chem*. 284(8):4897–4904.

- Moore JD, Potter A. 2013. Pin1 inhibitors: Pitfalls, progress and cellular pharmacology. *Bioorg Med Chem Lett.* 23(15):4283–4291.
- Morita J, Nakamura M, Kobayashi Y, Deng CX, Funato N, Moriyama K. 2014. Soluble form of fgfr2 with s252w partially prevents craniosynostosis of the apert mouse model. *Dev Dyn.* 243(4):560–567.
- Motch Perrine SM, Cole TM, 3rd, Martinez–Abadias N, Aldridge K, Jabs EW, Richtsmeier JT. 2014. Craniofacial divergence by distinct prenatal growth patterns in fgfr2 mutant mice. *BMC Dev Biol.* 14:8.
- Murakami S, Balmes G, McKinney S, Zhang ZP, Givol D, de Crombrughe B. 2004. Constitutive activation of mek1 in chondrocytes causes stat1–independent achondroplasia–like dwarfism and rescues the fgfr3–deficient mouse phenotype. *Gene Dev.* 18(3):290–305.
- Clinical trials.Gov. 2020. [accessed 2020]. <https://clinicaltrials.gov/>.
- Nout E, Bannink N, Koudstaal MJ, Veenland JF, Joosten KF, Poulton RM, van der Wal KG, Mathijssen IM, Wolvius EB. 2012. Upper airway changes in syndromic craniosynostosis patients following midface or monobloc advancement: Correlation between volume changes and respiratory outcome. *J Craniomaxillofac Surg.* 40(3):209–214.
- Oldridge M, Zackai EH, McDonald–McGinn DM, Iseki S, Morriss–Kay GM, Twigg SR, Johnson D, Wall SA, Jiang W, Theda C et al. 1999. De novo alu–element insertions in fgfr2 identify a distinct pathological basis for apert syndrome. *Am J Hum Genet.* 64(2):446–461.

- Ornitz DM, Itoh N. 2001. Fibroblast growth factors. *Genome Biol.* 2(3):REVIEWS3005.
- Ornitz DM, Legeai-Mallet L. 2017. Achondroplasia: Development, pathogenesis, and therapy. *Dev Dyn.* 246(4):291–309.
- Ornitz DM, Marie PJ. 2002. Fgf signaling pathways in endochondral and intramembranous bone development and human genetic disease. *Genes Dev.* 16(12):1446–1465.
- Ornitz DM, Marie PJ. 2015. Fibroblast growth factor signaling in skeletal development and disease. *Genes Dev.* 29(14):1463–1486.
- Orr-Urtreger A, Bedford MT, Burakova T, Arman E, Zimmer Y, Yayon A, Givol D, Lonai P. 1993. Developmental localization of the splicing alternatives of fibroblast growth factor receptor-2 (fgfr2). *Dev Biol.* 158(2):475–486.
- Ovchinnikov DA, Deng JM, Ogunrinu G, Behringer RR. 2000. Col2a1-directed expression of cre recombinase in differentiating chondrocytes in transgenic mice. *Genesis.* 26(2):145–146.
- Park OJ, Kim HJ, Woo KM, Baek JH, Ryoo HM. 2010. Fgf2-activated erk mitogen-activated protein kinase enhances runx2 acetylation and stabilization. *Journal of Biological Chemistry.* 285(6):3568–3574.
- Passos-Bueno MR, Richieri-Costa A, Sertie AL, Kneppers A. 1998. Presence of the apert canonical s252w fgfr2 mutation in a patient without severe syndactyly. *Journal of Medical Genetics.* 35(8):677–679.
- Pavlov MI, Sautier JM, Oboeuf M, Asselin A, Berdal A. 2003. Chondrogenic differentiation during midfacial development in the mouse: In vivo and in vitro studies. *Biol Cell.* 95(2):75–

- Pawson T, Scott JD. 2005. Protein phosphorylation in signaling—50 years and counting. *Trends Biochem Sci.* 30(6):286–290.
- Perantoni AO, Timofeeva O, Naillat F, Richman C, Pajni–Underwood S, Wilson C, Vainio S, Dove LF, Lewandoski M. 2005. Inactivation of *fgf8* in early mesoderm reveals an essential role in kidney development. *Development.* 132(17):3859–3871.
- Peters K, Ornitz D, Werner S, Williams L. 1993. Unique expression pattern of the *fgf* receptor 3 gene during mouse organogenesis. *Dev Biol.* 155(2):423–430.
- Peters KG, Werner S, Chen G, Williams LT. 1992. Two *fgf* receptor genes are differentially expressed in epithelial and mesenchymal tissues during limb formation and organogenesis in the mouse. *Development.* 114(1):233–243.
- Pippenger BE, Ventura M, Pelttari K, Feliciano S, Jaquiere C, Scherberich A, Walboomers XF, Barbero A, Martin I. 2015. Bone-forming capacity of adult human nasal chondrocytes. *J Cell Mol Med.* 19(6):1390–1399.
- Posnick JC. 2014. Orthognathic surgery. W.B. Saunders.
- Powers CJ, McLeskey SW, Wellstein A. 2000. Fibroblast growth factors, their receptors and signaling. *Endocr–Relat Cancer.* 7(3):165–197.
- Ren SX, Ma L, Sun ZP, Qian J. 2014. Relationship between palate–vomer development and maxillary growth in submucous cleft palate patients. *Cleft Palate–Cran J.* 51(3):314–319.
- Rohlf FJ, Corti M. 2000. Use of two–block partial least–squares to study covariation in shape. *Syst Biol.* 49(4):740–753.
- Sahni M, Ambrosetti DC, Mansukhani A, Gertner R, Levy D, Basilico

- C. 1999. Fgf signaling inhibits chondrocyte proliferation and regulates bone development through the stat-1 pathway. *Gene Dev.* 13(11):1361–1366.
- Sanchez C, Bay–Jensen AC, Pap T, Dvir–Ginzberg M, Quasnicka H, Barrett–Jolley R, Mobasher A, Henrotin Y. 2017. Chondrocyte secretome: A source of novel insights and exploratory biomarkers of osteoarthritis. *Osteoarthr Cartilage.* 25(8):1199–1209.
- Setlur J, Goyal P. 2011. Relationship between septal body size and septal deviation. *Am J Rhinol Allergy.* 25(6):397–400.
- Shimizu H, Yokoyama S, Asahara H. 2007. Growth and differentiation of the developing limb bud from the perspective of chondrogenesis. *Dev Growth Differ.* 49(6):449–454.
- Shin HR, Bae HS, Kim BS, Yoon HI, Cho YD, Kim WJ, Choi KY, Lee YS, Woo KM, Baek JH et al. 2018. Pin1 is a new therapeutic target of craniosynostosis. *Hum Mol Genet.* 27(22):3827–3839.
- Shukla V, Coumoul X, Wang RH, Kim HS, Deng CX. 2007. Rna interference and inhibition of mek–erk signaling prevent abnormal skeletal phenotypes in a mouse model of craniosynostosis. *Nature Genet.* 39(9):1145–1150.
- Singh G. 2015. Textbook of orthodontics.
- Su N, Jin M, Chen L. 2014. Role of fgf/fgfr signaling in skeletal development and homeostasis: Learning from mouse models. *Bone Res.* 2:14003.
- Szebenyi G, Savage MP, Olwin BB, Fallon JF. 1995. Changes in the expression of fibroblast growth factor receptors mark distinct stages of chondrogenesis in vitro and during chick limb

- skeletal patterning. *Dev Dyn.* 204(4):446–456.
- Wang Y, Sun M, Uhlhorn VL, Zhou X, Peter I, Martinez–Abadias N, Hill CA, Percival CJ, Richtsmeier JT, Huso DL et al. 2010. Activation of p38 mapk pathway in the skull abnormalities of apert syndrome *fgfr2(+p253r)* mice. *BMC Dev Biol.* 10:22.
- Wang Y, Xiao R, Yang F, Karim BO, Iacovelli AJ, Cai J, Lerner CP, Richtsmeier JT, Leszl JM, Hill CA et al. 2005. Abnormalities in cartilage and bone development in the apert syndrome *fgfr2(+s252w)* mouse. *Development.* 132(15):3537–3548.
- Wealthall RJ, Herring SW. 2006. Endochondral ossification of the mouse nasal septum. *Anat Rec A Discov Mol Cell Evol Biol.* 288(11):1163–1172.
- Wei X, Thomas N, Hatch NE, Hu M, Liu F. 2017. Postnatal craniofacial skeletal development of female *c57bl/6ncrl* mice. *Front Physiol.* 8:697.
- Wenger TL, Dahl J, Bhoj EJ, Rosen A, McDonald–McGinn D, Zackai E, Jacobs I, Heike CL, Hing A, Santani A et al. 2017. Tracheal cartilaginous sleeves in children with syndromic craniosynostosis. *Genet Med.* 19(1):62–68.
- Wilkie AO. 2005. Bad bones, absent smell, selfish testes: The pleiotropic consequences of human *fgf* receptor mutations. *Cytokine Growth Factor Rev.* 16(2):187–203.
- Wink JD, Bastidas N, Bartlett SP. 2013. Analysis of the long–term growth of the mandible in apert syndrome. *J Craniofac Surg.* 24(4):1408–1410.
- Xie C, De S, Selby A. 2016. Management of the airway in apert syndrome. *J Craniofac Surg.* 27(1):137–141.
- Xu Y, Malladi P, Zhou D, Longaker MT. 2007. Molecular and cellular

- characterization of mouse calvarial osteoblasts derived from neural crest and paraxial mesoderm. *Plast Reconstr Surg.* 120(7):1783–1795.
- Yin L, Du X, Li C, Xu X, Chen Z, Su N, Zhao L, Qi H, Li F, Xue J et al. 2008. A pro253arg mutation in fibroblast growth factor receptor 2 (fgfr2) causes skeleton malformation mimicking human apert syndrome by affecting both chondrogenesis and osteogenesis. *Bone.* 42(4):631–643.
- Yoon WJ, Cho YD, Kim WJ, Bae HS, Islam R, Woo KM, Baek JH, Bae SC, Ryoo HM. 2014. Prolyl isomerase pin1-mediated conformational change and subnuclear focal accumulation of runx2 are crucial for fibroblast growth factor 2 (fgf2)-induced osteoblast differentiation. *J Biol Chem.* 289(13):8828–8838.
- Yoon WJ, Islam R, Cho YD, Woo KM, Baek JH, Uchida T, Komori T, van Wijnen A, Stein JL, Lian JB et al. 2013. Pin1-mediated runx2 modification is critical for skeletal development. *J Cell Physiol.* 228(12):2377–2385.
- Yoshida T, Vivatbutsiri P, Morriss-Kay G, Saga Y, Iseki S. 2008. Cell lineage in mammalian craniofacial mesenchyme. *Mech Dev.* 125(9–10):797–808.
- Yu K, Herr AB, Waksman G, Ornitz DM. 2000. Loss of fibroblast growth factor receptor 2 ligand-binding specificity in apert syndrome. *Proc Natl Acad Sci U S A.* 97(26):14536–14541.
- Yu K, Xu J, Liu Z, Sosic D, Shao J, Olson EN, Towler DA, Ornitz DM. 2003. Conditional inactivation of fgf receptor 2 reveals an essential role for fgf signaling in the regulation of osteoblast function and bone growth. *Development.* 130(13):3063–3074.

Zaidi SK, Javed A, Choi JY, van Wijnen AJ, Stein JL, Lian JB, Stein GS. 2001. A specific targeting signal directs runx2/cbfa1 to subnuclear domains and contributes to transactivation of the osteocalcin gene. *Journal of Cell Science*. 114(17):3093–3102.

Zaidi SK, Javed A, Pratap J, Schroeder TM, Westendorf JJ, Lian JB, Van Wijnen AJ, Stein GS, Stein JL. 2006. Alterations in intranuclear localization of runx2 affect biological activity. *Journal of Cellular Physiology*. 209(3):935–942.

VII. 국문 초록

에이퍼트 증후군 모델 마우스 얼굴 기형의 3차원 형태 분석을 통한 발병 기전 규명 및 치료법 확립

김 봉 수

서울대학교 대학원

치의과학과 분자유전학 전공

(지도교수 류 현 모)

주로 FGFR2 돌연변이에 의한 FGF/FGFR 신호 증가로 인해 발생하는 에이퍼트 증후군 (Apert syndrome)은 대표적으로 두개골 조기 유합증 (craniosynostosis)과 중안모 저성장 (midface hypoplasia), 그로 인한 호흡 곤란 등의 증상을 나타낸다. 하지만 현재로서는 중안모 저성장의 정확한 발병 기전을 알지 못하며, 어린 시기부터 여러 차례에 걸친 수술 이외에는 치료 방법이 없는 실정이다. 본 연구에서는 에이퍼트 증후군의 마우스 모델 (*Fgfr2^{S252W/+}*)을 사용하여, 3차원 형태 분석과 조직학적 분석을 통해 중안모 저성장을 일으키는 주요 원인을 파악하고자 한다. 또한 증상의 예방과 치료를 위한 약물 타겟 및 적절한 수술 방법을 제시하고자 한다.

Part 1에서는, Micro-CT로 촬영한 에이퍼트 마우스 두개안면부의

3차원적 형태 분석을 통해, 안면부를 구성하는 여러 봉합 (suture)의 조기 유합으로 인한 안면부의 길이 감소 및 형태 이상이 가장 두드러지게 나타나는 것을 확인하였다. 이러한 형태 변화는 두개저 (cranial base)의 휘어짐 현상과 밀접하게 연관되어 있으며, 이는 에이퍼트 증후군에서 나타나는 호흡 문제를 직접적으로 야기할 수 있는 요인으로 생각된다. 또한, FGF/FGFR 신호 전달 효소인 PIN1 (Peptidyl-prolyl *cis-trans* isomerase NIMA-interacting 1)을 유전적 또는 약물학적으로 억제하여 에이퍼트 증후군 마우스 모델에서 나타나는 증안모 증상들이 호전되는 결과를 확인하였다.

Part 2에서는, 연골 특이적으로 FGFR2 돌연변이를 발현하는 마우스 모델을 사용하여 안면부를 구성하는 연골 조직의 성장 변화 및 증안모 발달에 미치는 영향을 살펴보고자 하였다. 해당 마우스에서는 관상 봉합 (coronal suture) 및 안면부를 구성하는 봉합의 조기 유합이 나타나지 않았지만, 여전히 증안모 성장 저하 증상이 나타났고, 특히, 비근점 (nasion)이 위로 솟아 오르는 현상, 앞위턱뼈 (premaxilla)와 보습뼈 (vomer) 사이의 유합, 별집뼈 (ethmoid bone)의 형성 감소, 코뼈 휘어짐 증상이 두드러지게 나타났다. 해부학적으로 이들 골 조직은 비중격 연골 (nasal septal cartilage)을 중심으로 연결되어 있는데, 비중격 연골의 3차원 형태학적 분석을 통해 연골의 두께가 두꺼워지고 형태가 변형되어 비중격 만곡 (septal deviation)이 나타나는 것을 확인하였다. 이러한 비중격 연골의 두께 및 높이 증가는 연골을

구성하는 연골 세포의 비대 (hypertrophy) 증가로 인한 것으로 나타났다. 결과적으로, FGFR2 돌연변이에 의한 비중격 연골의 두께 증가 및 형태 변화는 안면부의 성장 저하를 일으키는 중심적인 역할을 하는 것으로 보인다.

본 연구에서는 다각적이고 자세한 3차원 형태 분석을 통해 에이퍼트 증후군의 마우스 모델에서 나타나는 중안모 저성장의 발병 기전을 분석하였다. 중안모 저성장의 주요 원인으로써, 안면을 구성하는 여러 봉합의 조기 유합과 두개저의 형태 변화, 그리고 비중격 연골 형태 변화를 제시하였고, 에이퍼트 증후군의 중안모 성장 저하 수술 과정에서의 적절한 수술 방법 전략을 제시할 수 있었다. 더불어, PIN1 억제로 인한 안면부 봉합의 조기 유합 증상 완화 효과를 보여줌으로써 에이퍼트 증후군의 약물 치료 타겟을 제시하였다. 따라서, 에이퍼트 증후군에서 나타나는 증상들을 다방면으로 분석한 본 연구의 결과가 에이퍼트 증후군의 증상 예방 및 완화, 중안모 성장 저하의 적절한 치료 방법과 시기를 결정하는데 응용 될 수 있을 것으로 기대한다.

주요어: 에이퍼트 증후군, 중안모저성장, PIN1 비중격 연골, 3차원 구조 분석, 연골세포 비대

학 번 : 2014-22043